Peeling behavior of thin viscoelastic tapes

Politecnico di Bari

Department of Mechanics, Mathematics and Management

Mechanical and Management Engineering
Ph.D. Program

SSD: ING-IND/13 - Applied Mechanics

Final dissertation

Peeling behavior of thin viscoelastic tapes

Marco Ceglie

Supervisors:

Prof. Giuseppe Carbone

Prof. Nicola Menga

Coordinator of the PhD Program:
Prof. Giuseppe P. Demelio

Course XXXVI, 01/11/2020 - 01/11/2023

Politecnico di Bari

LIBERATORIA PER L'ARCHIVIAZIONE DELLA TESI DI DOTTORATO

Al Magnifico Rettore
del Politecnico di Bari

Il/la sottoscritto/a Marco Ceglie nato/a a Altamura il 19/01/1995

residente a Altamura in via Catania 24 e-mail marco.ceglie@poliba.it

iscritto al 3° anno di Corso di Dottorato di Ricerca in Ingegneria Meccanica e Gestionale ciclo 36°

ed essendo stato ammesso a sostenere l'esame finale con la prevista discussione della tesi dal titolo:

Peeling Bheavior of Thin Viscoelastic Tapes

DICHIARA

1) di essere consapevole che, ai sensi del D.P.R. n. 445 del 28.12.2000, le dichiarazioni mendaci, la falsità negli atti e l'uso di atti falsi sono puniti ai sensi del codice penale e delle Leggi speciali in materia, e che nel caso ricorressero dette ipotesi, decade fin dall'inizio e senza necessità di nessuna formalità dai benefici conseguenti al provvedimento emanato sulla base di tali dichiarazioni;
2) di essere iscritto al Corso di Dottorato di ricerca Ingegneria Meccanica e Gestionale ciclo 36°, corso attivato ai sensi del "*Regolamento dei Corsi di Dottorato di ricerca del Politecnico di Bari"*, emanato con D.R. n.286 del 01.07.2013;
3) di essere pienamente a conoscenza delle disposizioni contenute nel predetto Regolamento in merito alla procedura di deposito, pubblicazione e autoarchiviazione della tesi di dottorato nell'Archivio Istituzionale ad accesso aperto alla letteratura scientifica;
4) di essere consapevole che attraverso l'autoarchiviazione delle tesi nell'Archivio Istituzionale ad accesso aperto alla letteratura scientifica del Politecnico di Bari (IRIS-POLIBA), l'Ateneo archivierà e renderà consultabile in rete (nel rispetto della Policy di Ateneo di cui al D.R. 642 del 13.11.2015) il testo completo della tesi di dottorato, fatta salva la possibilità di sottoscrizione di apposite licenze per le relative condizioni di utilizzo (di cui al sito http://www.creativecommons.it/Licenze), e fatte salve, altresì, le eventuali esigenze di "embargo", legate a strette considerazioni sulla tutelabilità e sfruttamento industriale/commerciale dei contenuti della tesi, da rappresentarsi mediante compilazione e sottoscrizione del modulo in calce (Richiesta di embargo);
5) che la tesi da depositare in IRIS-POLIBA, in formato digitale (PDF/A) sarà del tutto identica a quelle **consegnate**/inviate/da inviarsi ai componenti della commissione per l'esame finale e a qualsiasi altra copia depositata presso gli Uffici del Politecnico di Bari in forma cartacea o digitale, ovvero a quella da discutere in sede di esame finale, a quella da depositare, a cura dell'Ateneo, presso le Biblioteche Nazionali Centrali di Roma e Firenze e presso tutti gli Uffici competenti per legge al momento del deposito stesso, e che di conseguenza va esclusa qualsiasi responsabilità del Politecnico di Bari per quanto riguarda eventuali errori, imprecisioni o omissioni nei contenuti della tesi;
6) che il contenuto e l'organizzazione della tesi è opera originale realizzata dal sottoscritto e non compromette in alcun modo i diritti di terzi, ivi compresi quelli relativi alla sicurezza dei dati personali; che pertanto il Politecnico di Bari ed i suoi funzionari sono in ogni caso esenti da responsabilità di qualsivoglia natura: civile, amministrativa e penale e saranno dal sottoscritto tenuti indenni da qualsiasi richiesta o rivendicazione da parte di terzi;
7) che il contenuto della tesi non infrange in alcun modo il diritto d'Autore né gli obblighi connessi alla salvaguardia di diritti morali od economici di altri autori o di altri aventi diritto, sia per testi, immagini, foto, tabelle, o altre parti di cui la tesi è composta.

Luogo e data Bari, 15/12/2023 Firma 

Il/La sottoscritto, con l'autoarchiviazione della propria tesi di dottorato nell'Archivio Istituzionale ad accesso aperto del Politecnico di Bari (POLIBA-IRIS), pur mantenendo su di essa tutti i diritti d'autore, morali ed economici, ai sensi della normativa vigente (Legge 633/1941 e ss.mm.ii.),

CONCEDE

- al Politecnico di Bari il permesso di trasferire l'opera su qualsiasi supporto e di convertirla in qualsiasi formato al fine di una corretta conservazione nel tempo. Il Politecnico di Bari garantisce che non verrà effettuata alcuna modifica al contenuto e alla struttura dell'opera.
- al Politecnico di Bari la possibilità di riprodurre l'opera in più di una copia per fini di sicurezza, back-up e conservazione.

Luogo e data Bari, 15/12/2023 Firma 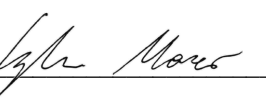

Politecnico di Bari

Department of Mechanics, Mathematics and Management

Mechanical and Management Engineering
Ph.D. Program

SSD: ING-IND/13 - Applied Mechanics

Final dissertation

Peeling behavior of thin viscoelastic tapes

Marco Ceglie

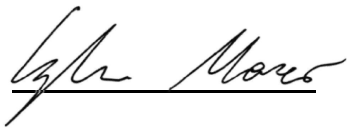

Referees:

Prof.ssa Elena PIERRO

Prof. Michele SCARAGGI

Supervisors:

Prof. Giuseppe Carbone

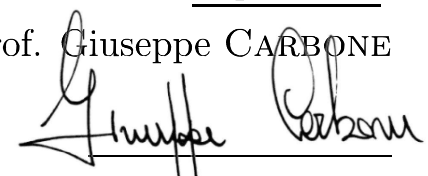

Prof. Nicola Menga

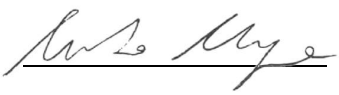

Coordinator of the PhD Program:
Prof. Giuseppe P. Demelio

Course XXXVI, 01/11/2020 - 01/11/2023

Abstract

Viscoelasticity, friction and geometry: which is their role in governing the behavior of adhesive systems? Despite the long standing effort on these issues, capturing and modeling dissipative phenomena and non-linearities inherent in real processes is a tough challenge, leaving several questions and problems unresolved. This thesis explores some of these particular aspects in soft contact mechanics with a primary emphasis on peeling processes. In the first part, an overview of the peeling mechanism is provided where the most important results and models are discussed. Main concepts of linear viscoelasticity are also given to define the mathematical framework for analyzing viscoelastic peeling. We address the single peeling of thin viscoelastic tapes in the case of stuck and frictional sliding interfaces. While a Kendall-like behavior is predicted in the absence of slippage, when considering frictional dissipation in the model sensible differences emerge. Higher peeling forces are observed at low peeling angles and the system toughness becomes velocity-dependent in agreement with experimental observation and phenomenological models. We also investigate the V-peeling configuration addressing the nonsteady propagation which occurs as the effect of time-dependent material behavior and system geometry variation. Non monotonic evolution of peeling quantities results from the continuous creep of tape during the detachment process which can also arrest for particular combinations of initial parameters and loading conditions. Interestingly, for impact loading conditions an enhancement of peel resistance is predicted suggesting that viscoelasticity could be crucial for the superior adhesive performance of natural peeling systems. In the last part, we discuss an experimental study on sliding contact between a spherical glass robe and a PDMS substrate carried via an *ad hoc* device which allows for the measure of surface in-plane displacements. We consistently observe a contact area reduction and a shape asymmetry as a possible effect of geometrical and material non-linearities arising in the tensile/compressive zone at the trailing and leading edge, respectively, where high levels of strain are achieved and normal-tangential uncoupling predicted from linear-elasticity is broken. Mechanical confinement also leads to a modification of coupling behavior with respect to infinite contact conditions, suggesting that geometrical aspects are pivotal to better understanding frictional adhesive contact.

Keywords: peeling, adhesion, viscoelasticity, friction, sliding contact, soft contact, elastomer.

Contents

List of Figures

Introduction

Contact mechanics represents a fundamental branch of both physics and engineering that delves into the study of interactions between solid surfaces upon contact. Its significance extends across various domains, including materials science, mechanical engineering, biology and biomimetics. Contact mechanics proves invaluable due to its capacity to unveil the intricate behaviors of materials across macroscopic, micro, and nanoscale dimensions, thereby shedding light on numerous facets of our daily lives from multiple perspectives. For instance, the peculiar behavior of certain biological tissues has inspired numerous studies aimed at interpreting and reproducing the adhesive [1, 2], self-cleaning [3], self-healing [4], drag reduction [5], idrorepellant [6] and hydrophilic [7] properties exhibited by plants and animals because of the potential practical applications in several technological sectors, such as soft-robotics [8, 9], coating [10], manufacturing [11], construction [12] and medical industries [13]. Regarding this, the possibility of managing the adhesive strength between mating surfaces is of primary concern for both biological processes and engineering applications, for vital functions and locomotive purposes in the former case, for developing reliable, controllable and efficient systems in the latter. In facing these necessities, peeling represents one of the most observed and exploited mechanisms of detachment, as it meets the requirements of high adaptability, controllability and reliability.

Although adhesives have been used since ancient times, just in the second half of the 20th century the research on this field experienced significant growth, coinciding with the widespread adoption of synthetic polymers and their significant technological impact [14]. In this context, the first description of the peeling dates back to 1944 with Rivlin's study where a measure of the adhesion strength between surfaces was proposed by means of a simple peeling test [15]. Since then, the effectiveness of the peeling test as a valuable method for the characterization of materials properties, adhesive interfaces and delamination resistance of layered materials has been witnessed by numerous standards based on different peeling setup [16]. Concurrently, even physical models have been proposed to interpret the behavior of peeling system and to interpret experimental evidences. Among them, Kendall's model [17] stands out as one of the most important contribution in the field as, for the first time, the peeling process was described by energy arguments under a fracture mechanics perspective. This groundbreaking approach paved the way for an extensive research in this area aimed at enhancing peeling models in effectively reflecting the real behavior of adhesive systems. Many aspects have been addressed by integrating into the formulation a series of parameters such as ge-

ometry [18–20], properties of the backing and substrate [21–25], peel-rate [26–28], and interfacial mechanisms such as stick-slip [29–31] and slippage [32–34]. In particular, much attention has been devoted to energy dissipation mechanisms due to their potential to aid in understanding the rate-dependent behavior of peeling systems and the origin of the high adhesive strength observed during debonding processes [35]. Major sources of energy losses could arise both at the level of material bulk where viscoelastic and plastic material responses could be triggered during the debonding process, and at the interface where the rupture of interfacial bonds and relative sliding tape-substrate could undergo non-conservative and frictional dissipation. Although materials common in peeling systems usually exhibit a certain degree of viscoelastic behavior, still viscoelasticity is poorly considered in peeling model, especially in combination with other dissipative mechanisms and more complicated peeling geometries. How does viscoelastic behavior impact the peeling process? Is there a correlation between viscoelastic losses and non-steady propagation behavior? When developing peeling models, is it necessary to take slippage into account and how are viscous and frictional dissipation related?

This thesis will try to answer these questions by investigating the peeling mechanism of thin viscoelastic tapes from rigid substrates, seeking to understand the contribution of local interface interactions and the system's geometric arrangement in governing the peeling behavior. In particular, in Chapter 1, an overview of the peeling mechanism is presented: the first studies, the fracture mechanics energy approach and the major results of the actual research are exposed. Chapter 2 introduces the viscoelasticity and the basic constitutive models for linear viscoelastic material. In Chapter 3, a model for the single peeling of thin viscoelastic tapes is presented; an energy-based formulation is used to account for the interfacial slippage aiming at understanding the combined influence of frictional and viscoelastic dissipation. Chapter 4 addresses the V-peeling of thin viscoelastic tapes; the governing equations are firstly derived by an energy-based approach, then integrated through an *ad hoc* numerical procedure able to predict the time evolution of the peeling process. In conclusion, Chapter 5 is dedicated to presenting some results of sliding experiments between a smooth glass spherical probe and PDMS substrate aiming at investigating frictional behavior in soft contact.

Chapter 1

Peeling: an overview

The peeling mechanism is a fascinating and intricate phenomenon that occurs in a wide range of natural and man-made contexts. It can be defined as the mechanism of detachment of thin bodies occurring via propagation of a peeling front. Pulling off Scotch® tape from a surface, removing protective films or a band-aid from the skin, or opening a package are some of everyday life situations where we encounter peeling. However, peeling process is also pivotal for vital functions of many animals and in governing the adhesion of biological systems. Most important example is represented by the superior adhesive performance and the ability to switch between firm attachment and effortless detachment of insects, reptiles and amphibia [2,36,37] based on the possibility of exploiting peeling actions at the level of toes which allows for a very efficient control of adhesive forces on every surface in dry, wet, smooth and rough conditions [38]. This behavior has inspired engineers in developing so called climbing robots [39] which emulate attachment/detachment mechanism of geckos both macroscopically, by simulating digital hyperextension [40], and microscopically, with the presence of micro-structured surfaces [41] also employed in reversible adhesive tapes used for medical scope [38,42]. Beside the so called *bioinspired* applications, peeling is also important in technological contexts, from painting and coating sectors, to transfer printing [43,44], or robotics in developing soft grippers [45], and its relevance is also witnessed by peeling tests used for material characterization and adhesive force measure [16,46,47]. For these reasons, investigating and characterizing the peeling mechanism is not only of significant scientific interest but also holds practical implications in various fields, from biology and materials science to industrial processes and everyday life problems (Fig. 1.1).

In this chapter, an overview of the peeling mechanism is presented. In the first part, we present the theoretical-experimental background and the fracture mechanics framework used for addressing the peeling problems. In the second part most relevant studies and findings that have contributed to a better understanding of the topic will be covered.

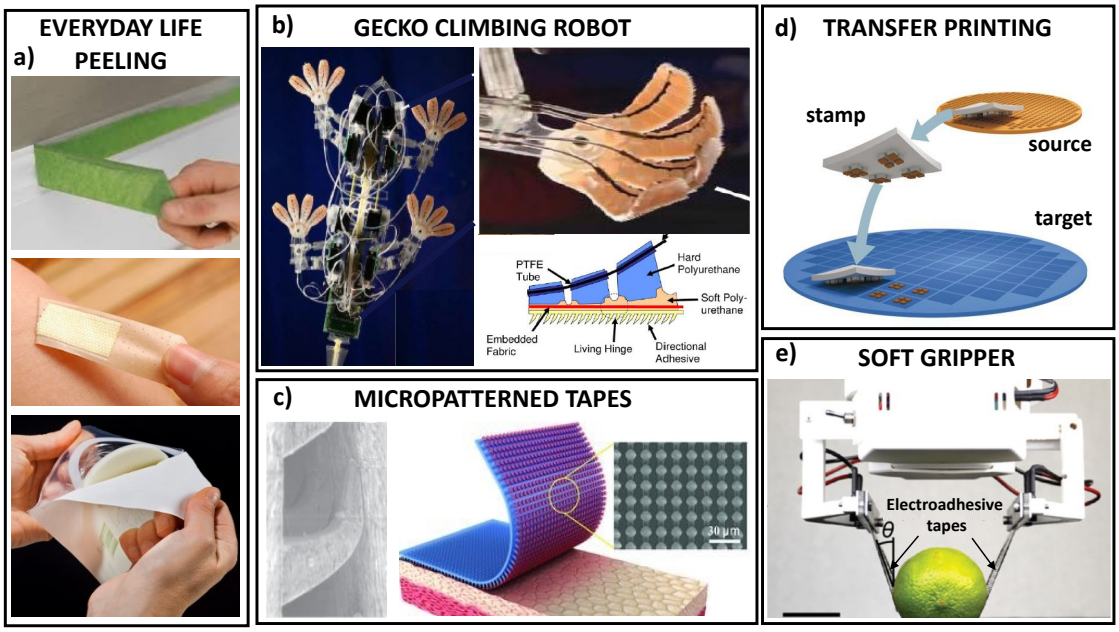

Figure 1.1: (a) Example of everyday life peeling. From Google Images. (b) Stickybot inspired by Gecko adhesion mechanism. Toes allow for digit hyperestension and have a directional adhesive stalks on the surface for achieving high adhesion. Adapted from [39]. (c) Examples of micropatterned adhesive tapes. Adapted from [41, 42]. (d) Transfer printing process where delamination force are controlled to transfer objects from a source to a target surface. Credits *photonics.com*. (e) Soft gripper based on electroadhesive tapes. Releasing is facilitated by peeling action. From [45].

1.1 Peeling as a fracture problem

Driven by practical motivations of interest of aeronautic and marine industries, at the beginning of the XX century, a significant effort was dedicated to the characterization of material behavior, with a particular focus on the initiation and propagation of cracks and fractures. Trying to reconcile experimental observations and theoretical predictions of the critical stress needed to fracture metal and glass, Griffith sensed that microdefects in the material could cause a concentration of stresses such as to reach locally values which trigger rupture. The needs of a mathematical framework able to explain these phenomena, inspired Griffith in developing a thermodynamic approach to address fracture problem.

Griffith theory [48], presented in 1920, is based on the concept of energy release rate G, roughly speaking, the energy available to propagate a crack. If this energy is higher or equal a critical value G_c, associated with the energy needed for the creation of new free surfaces, fracture propagates. Thus, the so called Griffith criterion for the crack propagation requires

$$G \geq G_c \tag{1.1}$$

In other words, according with the principle of minimum energy, a fracture propagation is possible as far as the crack growth reduces the system's energy by a

quantity sufficient to overcome the fracture energy.

Griffith applied his intuition firstly on material assumed perfect elastic. In this case, the equilibrium fracture condition can be expressed as

$$G = -\left(\frac{\partial U_P}{\partial a} + \frac{\partial U_{el}}{\partial a}\right) = G_c \tag{1.2}$$

where the two terms represent the variation of potential energy of the applied external forces U_P, and elastic energy U_{el}, respectively, for an infinitesimal increment of the crack size a. Although experiments carried out on glass specimens perfectly fit theoretical predictions, for structural materials exhibiting a ductile behavior, the actual level of energy needed to cause fracture was orders of magnitude underestimated. For this reason Griffith's work was largely ignored by the engineering community until the early 1950s [49], when Irwin work extended original formulation for non brittle material by accounting for plastic deformation close crack zone [50]. This intuition opened the way for an extensive application of the Griffith energy approach where different sources of energy dissipation are considered attempting to better describe real fracture phenomena.

1.1.1 Fracture mechanics perspective of adhesion and debonding processes

From this perspective, a debonding process between two contact bodies can be seen as the propagation of a crack within the contact interface and can be studied in the context of fracture mechanics. In this case, the separation criterion requires that G equals or overcomes the work of adhesion Γ.

Dupré work of adhesion

The thermodynamic (or Dupré) work of adhesion is a fundamental quantity in contact and fracture mechanics and represents the reversible work required to separate unit area of two phases in contact. It is given by

$$\gamma = \gamma_1 + \gamma_2 - \gamma_{12} \tag{1.3}$$

where γ_1 and γ_2 are the surface energies of the two materials, and γ_{12} is the interfacial energy. γ is an intrinsic property of materials and the specific interfacial interaction they establishes when in contact. Depending on the essence of the interacting surfaces, the adhesive forces can be classified into four main types [51]: a) surface and field forces: are attractive or repulsive forces generated from distant dependent interactions. They include short-range van der Walls forces, electrostatic and magnetic forces. b) Material bridges arise from bond established at atomic and molecular level. This is the case, for instance of, diffusion process observable in polymers as chains' entanglements process, or strong chemical (ionic, covalent, metallic) bonds. Moreover, in wet conditions, capillary interaction could arise between two solids when a liquid forms capillary bridges between two surfaces. c)

Mechanical interlocking established between surfaces thanks to pure shape effects (e.g. hook-and-loop). d) Suction forces generated via pressure difference between the internal and surrounding ambient. (See Fig. 1.2)

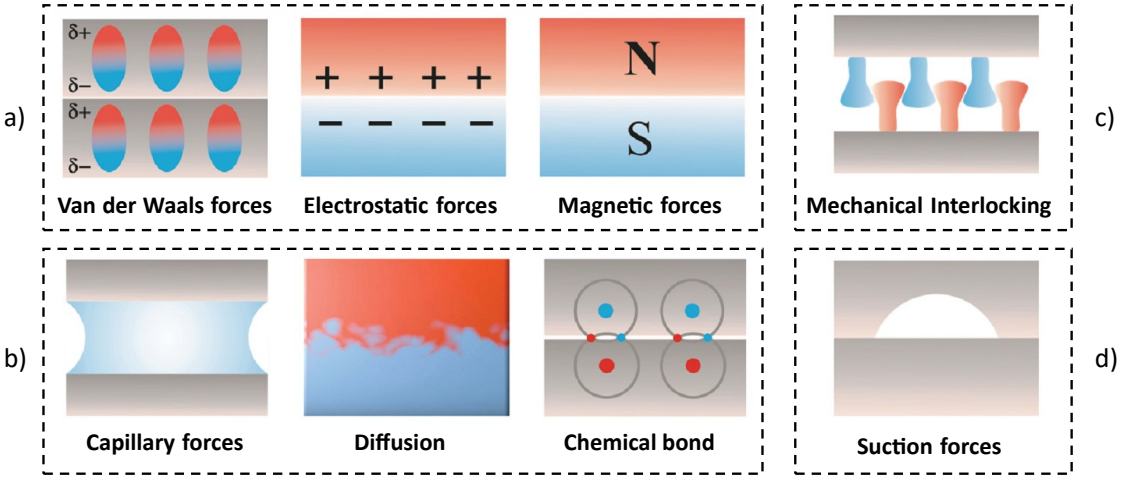

Figure 1.2: Representation of different adhesive interaction: a) surface and field forces, b) material bridges, c) mechanical interlocking, d) suction forces. Adapted from [51].

Effective fracture work

It is important to remark that Dupré energy corresponds to the work of adhesion for an ideal reversible process and is the minimum work needed to separate two surfaces. However, in real processes, the effective work needed for trigger debonding Γ can largely exceed the Dupré work of adhesion γ, and therefore it results to be not a merely intrinsic interface/material property. In fact, the surfaces separation process involves non-consevative phenomena responsible for an increases of the real energy required for the debonding. These effects include both mechanism occurring at the interface as friction, rupture of chemical bonds, polymer's chains pull-out, as well as in the material bulk as plasticity and viscoelasticity processes [52]. Since formally including such effects in adhesion models could be very challenging, empirical relations has been proposed to account for a comprehensive dissipative effect contribution. According with the Gent and Shultz expression [53], the effective fracture work is commonly expressed as sum of two terms

$$\Gamma = \Gamma_0[1 + \Phi(\dot{a}, T, etc.)] \tag{1.4}$$

where Φ is the dissipative function and Γ_0 is a constant term. Note that Φ mainly depends on the rate of detachment $\dot{a}$ and the temperature T, reflecting the dominant influence of the viscoelastic and plastic effect on the overall energy loss. Even if Γ_0 may also depend on the particular debonding process [16], for many practical application it is usually associated with the intrinsic adhesion energy γ exhibited in quasi-static debonding conditions, thus $\Gamma(\dot{a} \to 0) = \Gamma_0 = \gamma$.

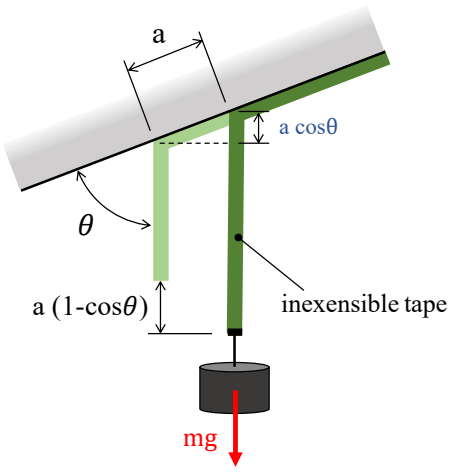

Figure 1.3: Scheme of Rivlin's peeling test.

1.1.2 Energy model for peeling

Rivlin's estimation of the adhesion energy

A first description of the peeling process within the context of fracture mechanics was presented by Rivlin in 40' [15]. He proposed a simple expression for quantifying the adhesion strength between two bodies based on inextensible tapes peel test, Fig. 1.3; in his model the force exercised by a dead weight of mass m is related to the adhesion energy Γ trough

$$\frac{mg}{w} = \frac{\Gamma}{1 - \cos\theta} \tag{1.5}$$

where θ is the peeling angle and w the tape width. This formula expresses an equilibrium between the work of the peeling force mg (g is the gravitational acceleration) and the energy needed for detaching a tape strip of length a.

The Kendall's model for elastic tape

However, the most successful peeling model is probably the one proposed by Kendall in 1971 which extended the Rivlin's formulation by accounting for the tape deformability [17]. In his seminal work, the peeling of an elastic tape from a rigid substrate is described through the balance of three energy contributions. See Fig. 1.4 reporting the peeling scheme of an elastic tape with Young modulus E and cross section $A_t = wd$ under the action of the external force P. In steady-state condition, the work done by the external force P for debonding a strip of length a can be written as

$$U_P = Pa(1 - \cos\theta + \varepsilon) = Pa(1 - \cos\theta + \frac{P}{EA_t}) \tag{1.6}$$

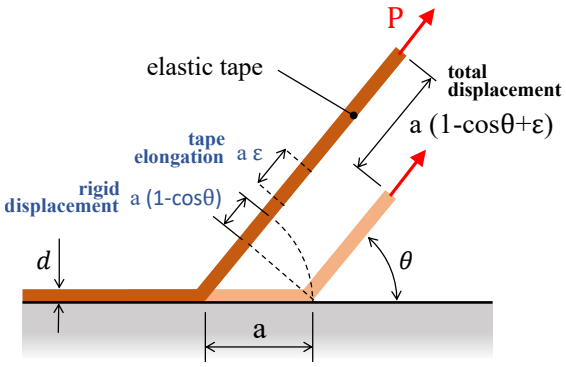

Figure 1.4: Scheme of single peeling of an elastic tape from a rigid substrate.

where θ is the peeling angle and $\varepsilon = P/EA_t$ is the tape deformation. The elastic energy stored in the debonded strip a is easily obtain as

$$U_{el} = \frac{P\varepsilon}{2}a = \frac{P^2}{2EA_t}a \tag{1.7}$$

Finally, the surface contribution given by the adhesion work Γ results

$$U_S = -\Gamma w a \tag{1.8}$$

The Griffith criterion for the debonding requires that the total energy release rate is zero at the equilibrium, in this case $dU_T/da = d(U_P + U_{el} + U_S)/da = 0$. The famous Kendall's equation for peeling is therefore given by

$$\frac{P^2}{2EA_t} + P(1 - \cos\theta) = \Gamma w \tag{1.9}$$

In Fig. 1.5 typical peeling behavior predicted by Kendall model. In many cases the tape stiffness largely exceed the tension $E \gg P/A_t$ so that the first term becomes negligible and the Rivlin solution for inextensible tapes is recovered Eq. (1.5). This is also usually observable for high value of peeling angle where low level of deformation are expected as the peeling force is low as well. However, for soft tapes or for low peeling angles, the first two term in Eq. (1.9) are comparable as the effect of higher deformations. In this latter case, in the limit of $\theta \to 0$ the maximum value of the peeling force is predicted from

$$\frac{P}{w} = \sqrt{2Ed\Gamma} \tag{1.10}$$

1.2 Important results of peeling study

As the potential energy U_P, the elastic energy U_{el} and the surface energy U_S are the conservative contributions which are usually present in peeling processes, Kendall formulation has represented the foundational framework for the development of more sophisticated models that incorporate additional effects and dissipative phenomena. In the following, we will present significant studies and findings in the field of peeling, deepening some aspects and side-phenomena providing valuable insights to better understand real debonding process.

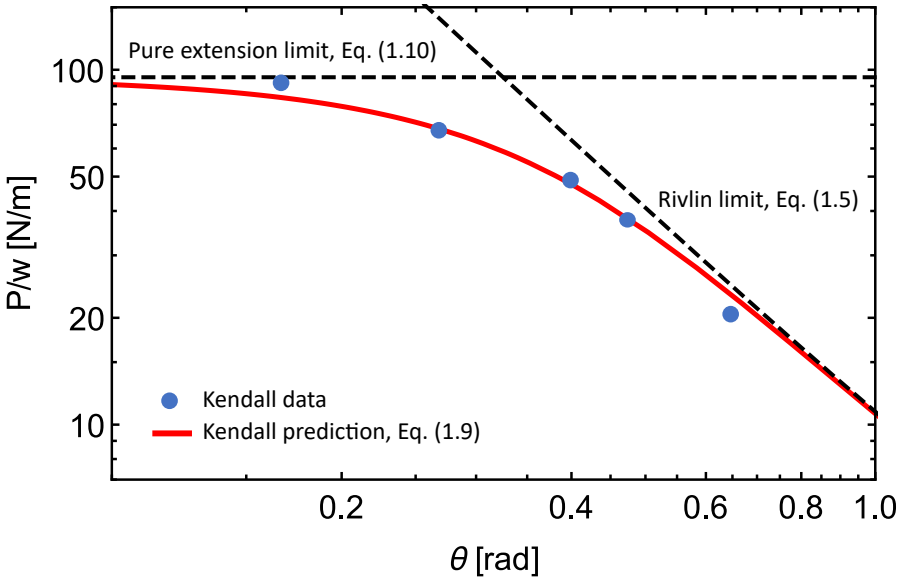

Figure 1.5: The peeling force P/w versus the peeling angle θ: Kendall's data points (blue dots) and prediction (red curve). Black dashed curves refer to limit solutions. Adapted from [54].

1.2.1 The effect of bending stiffness

In addition to the Kendall energy approach, beam model has also represented a noteworthy theoretical framework for analyzing peeling phenomena. Here, thin films are treated as slender beams, and the principles of pure bending beam theory are employed to investigate the interfacial bonding and debonding mechanisms. In this context, the first significant contributions to this approach was made by Spies in his pioneering work [55], where an explicit solutions for peel force and distribution of internal stress within the tape are calculated for 90° peeling of pure elastic tapes and adhesive. Later, Kaelble presented a more comprehensive model that addresses scenarios in which either the tape, the substrate, or both are flexible and extends analysis for arbitrary peeling angles, offering a broader perspective on the peeling process [56, 57]. Accounting for rheological behavior of the adhesive layer, he identified two systems of forces involved in the peeling mechanism: cleavage and shear forces, noting that only the former are responsible for the debonding. In the region of the peeling front, the rotation of the "stiff" peel arm generates a lever-like mechanism and an associated tensional-compressional stress distribution on the substrate (Fig 1.6). The resulting moment responsible for the detachment is linked to the peeling force P, the peeling angle θ and the tape bending stiffness EI (being E the elastic modulus and I the second moment of area of the tape section) by

$$P = \frac{\sum_i (f_i x_i)^2}{EI(1-\cos\theta)} \tag{1.11}$$

where f_i is the generic local normal force (compressive $f_i > 0$ or tensil $f_i < 0$) with x_i arm of such force.

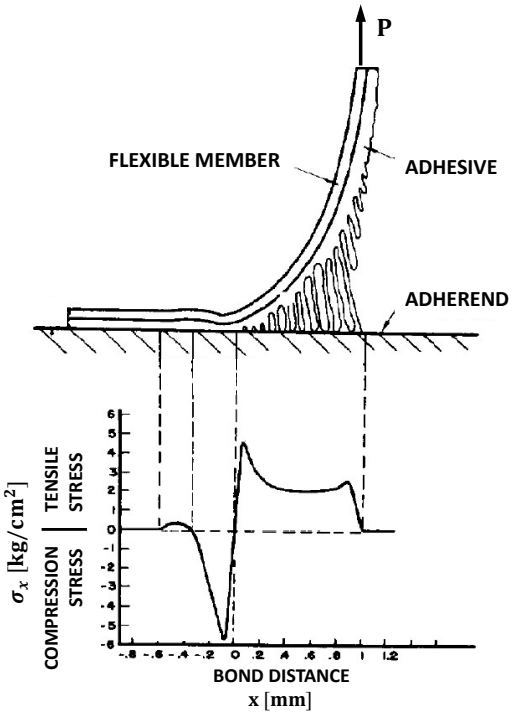

Figure 1.6: Schematic representation of the peel profiles and experimental distribution of normal stress on substrate surface. Adapted from [57].

Although rheological approaches offer an alternative method for studying the peeling problem in terms of force and stress distributions, has been demonstrated that conventional energy models are equally effective in predicting the dependence of peel force on peel angle, even for large bending situations [21]. However, as most of these works focuses on steady-state peeling process, for elastic films, the elastic energy contribution associated with the tape bend is usually neglected as it is constant $dU_b/da = 0$ [17]. Nonetheless, when the transient process is considered, the peeling mechanics is significantly affected by tape's bending stiffness. Indeed either experimental [58], theoretical [59,60] and numerical [61] investigations have observed a non-stationary value of the peeling force during the early stages as the effect of the increasing bending energy stored in the tape until the tangential angle of the film approaches the peeling angle, where the peeling force is well predicted by the Kendall's model, insensitive to the bending stiffness. As transient value of the peeling force can exceed the steady-state value, steady-state model could result ineffective in predicting the effective force for achieving a complete tape delamination (see Fig. 1.7).

The high curvature the tape experience very close to the peeling front, especially at high value of peeling angle, could induce high stress level which can trigger plastic deformations. In this scenario, plastic dissipation could occur in two different tape region during the peeling process [16,62]. The tape can plastically deform firstly in the region close to the peeling front where the moment and curvature are high (A-B region in Fig. 1.8). Then, because of the prior plastic deformation,

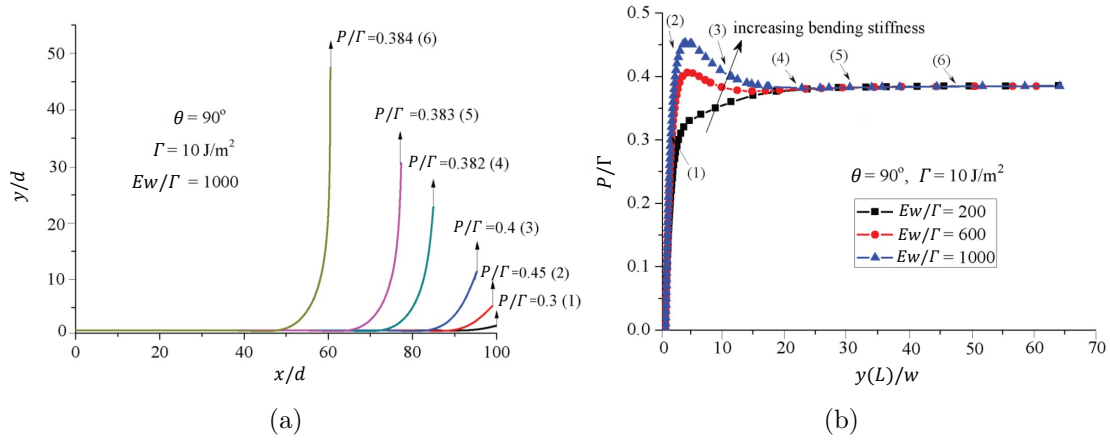

Figure 1.7: Profiles of the deformed film (a) and the peeling force (b) during different peeling moments. Adapted from [59].

the bent tape could undergo a reverse plastic bending which induce a reduction of the tape curvature (E-F region). As a result, a residual curvature lasts after the complete detachment process.

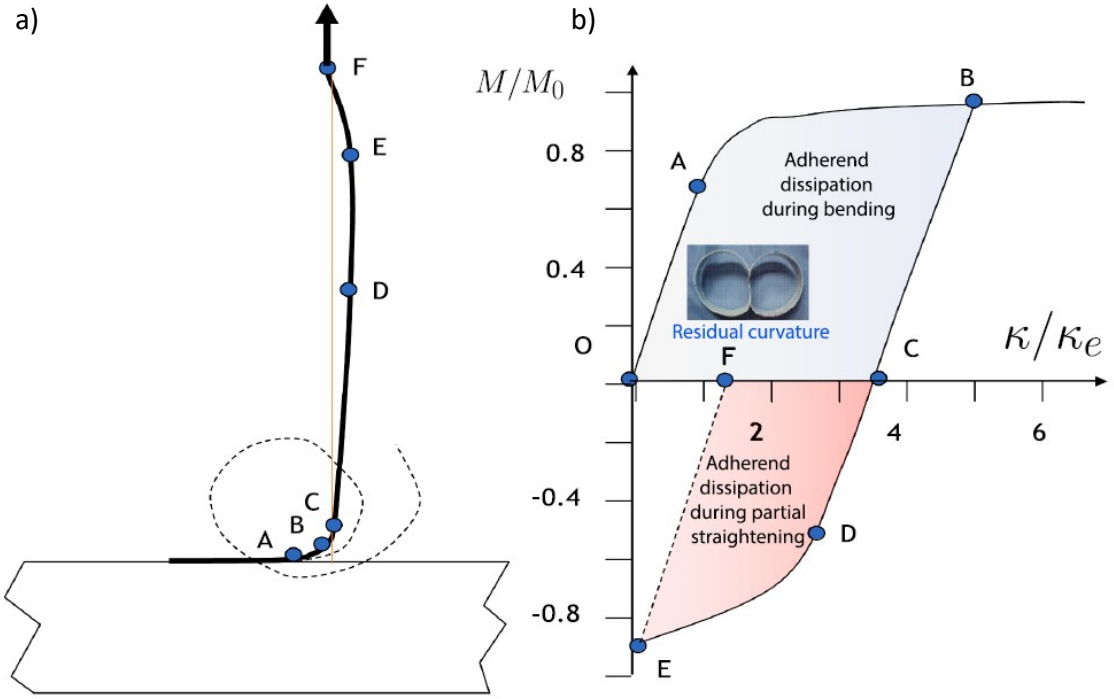

Figure 1.8: (a)Regions of deformation of the peel arm. Dashed line suggests the final shape of peel. (b) Normalized bending moment versus arm curvature during the debonding process (M_0 and κ_0 refer to bending moment and elastic curvature limit, respectively). From [16]

However, for viscoelastic tapes, the contribution of the bending stiffness is an

important factor even in steady-state condition as it could lead to the emergence of a rate-dependent behavior, triggered by dissipative effects close to the peeling front. We will better discuss this aspect in the next section.

1.2.2 Viscoelasticity in peeling systems

Viscoelasticity is a prevalent source of energy dissipation in the peeling process, occurring at the tape, foundation, and adhesive layer levels. The rate-dependent performance of the peeling system is primarily influenced by the intrinsic viscous behavior of the material, a problem extensively explored in numerous studies. Most of them rely on empirical relations which implicitly consider an overall dissipative contribution accounted in a peel-rate dependent dissipation function (See Eq. 1.4) [26, 27, 44, 63]. In these models, the peeling the peeling force is usually described by a power law expression of the kind

$$\frac{P}{w} = C_0 \left(1 + k v^n\right) \tag{1.12}$$

where where C_0 and k are parameters related to the peeling angle, the thickness of the viscoelastic thin-film and the contact adhesion energy, whereas n is a constant related to the intrinsic property of the thin film [64].

In other works, the effect of tape viscoelasticity has been investigated with rigorous analytical approaches by evaluating the viscoelastic energy loss due tensile and/or bending stress contribution within the whole detached tape assumed as a slender linear-viscoelastic beam [65]. An extensive and complete formulation is provided by Chen [25]; in steady-state condition he recovered the bending moment M and tensile T fields as a function of the peel rate and the mechanical properties of the viscoelastic tape obtaining a close form solution for the energy release rate

$$G = \frac{P}{w}(1 - \cos\theta) + \frac{1}{w}\int_0^\infty \kappa \frac{dM}{ds} ds + \frac{1}{w}\int_0^\infty \varepsilon_m \frac{dT}{ds} ds \tag{1.13}$$

where, κ and ε_m are the tape curvature and the membrane strain, respectively. He also observed that the tensile contribution is predominant over the bending contribution which also vanishes for high value of the peeling force, the peel rate and for thin tapes (Fig. 1.9b). However, for both empirical and analytical models the peeling force is an increasing function of the peel rate (Fig. 1.9c) which also affects the shape of the bend tape close to the peeling front becoming sharper for a faster detachment (Fig. 1.9d).

Aiming at controlling peeling force and detachment velocity, many studies have been dedicated at investigating the peeling behavior from compliant and stretchable substrate [21, 22, 66, 67]. In this matter, the problem of the peeling from viscoelastic substrate has been addressed because the direct implications in medical applications such as band-aid and transdermal drug delivery systems used on human tissues [68–70] (Fig. 1.10a).
Afferrante and Carbone have analytically investigated the peeling of elastic tapes from a viscoelastic foundation by accounted for the contribution of the internal

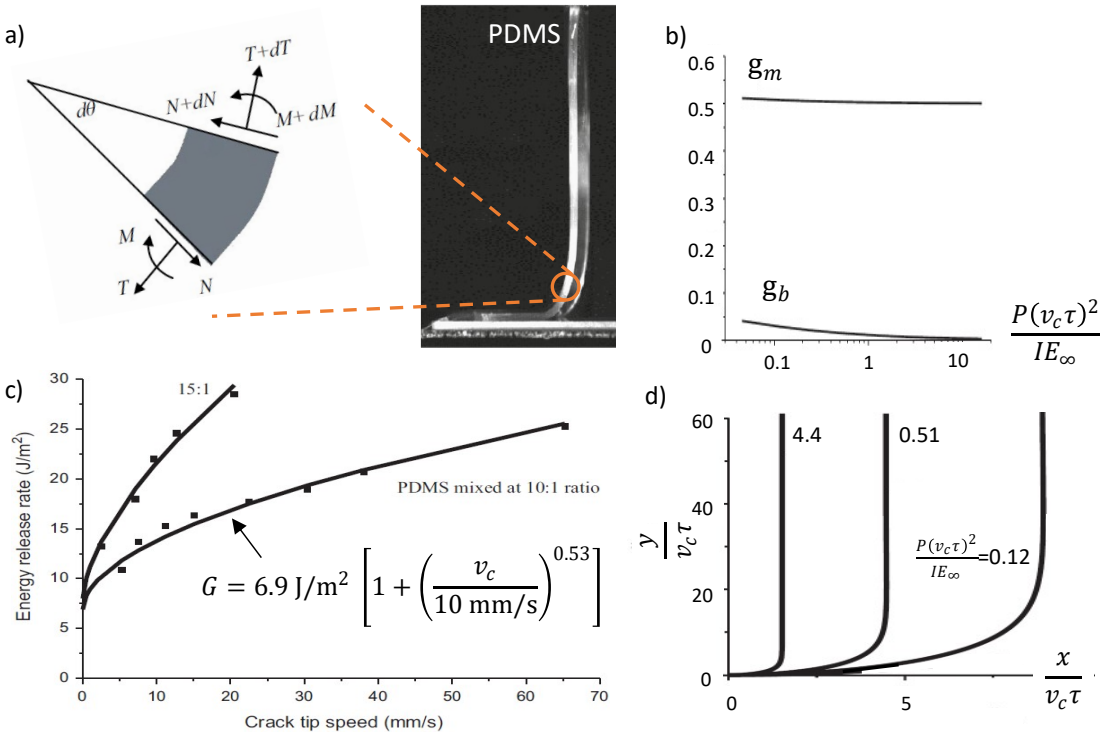

Figure 1.9: Peeling behavior of a PDMS viscoelastic tapes. (a) Schematic of forces within a tape's strip. (b) Typical trend of bending g_b and membrane g_m energy contribution versus the normalized peel force (being v_c the peel rate, τ the viscoelastic creep time, E_∞ the viscoelastic high frequency modulus, I the second area moment of the cross section). (c) Energy release rate versus the peel-rate, experimental data and power law fitting. (d) Tape profile for several normalized peel forces for vertical peeling. Adapted from [25]

energy in the viscoelastic material by means of a Green function methodology [23]. They found that, contrary to the commonly observed one-to-one correspondence between the peeling force and the detaching speed, in this case the systems allows for multiple solutions. In particular it results that for relatively stiff elastic tapes and small peeling angles, equilibrium is always possible for arbitrarily large values of the external load. In this case, the detachment velocity can be conveniently modulated in order to control the peeling process. By contrast, for high peeling angles or relatively compliant tapes, stable detachment occurs as long as the applied force is smaller than a certain limiting value P_{lim} whereas, for higher values, equilibrium is no longer possible and unstable detachment occurs (Fig. 1.10b,d). Later, Zhu and coworkers [71] extended this formulation including an rate-dependent adhesion energy, showing that the controllable detaching speed range is substantially enlarged and can be effectively tuned through modulating the substrate viscoelasticity as well as the peeling angle (Fig. 1.10c).

Moreover, when dealing with viscoleastic material the temperature is a crucial parameter as it significantly affects the rehological response. Local increasing of

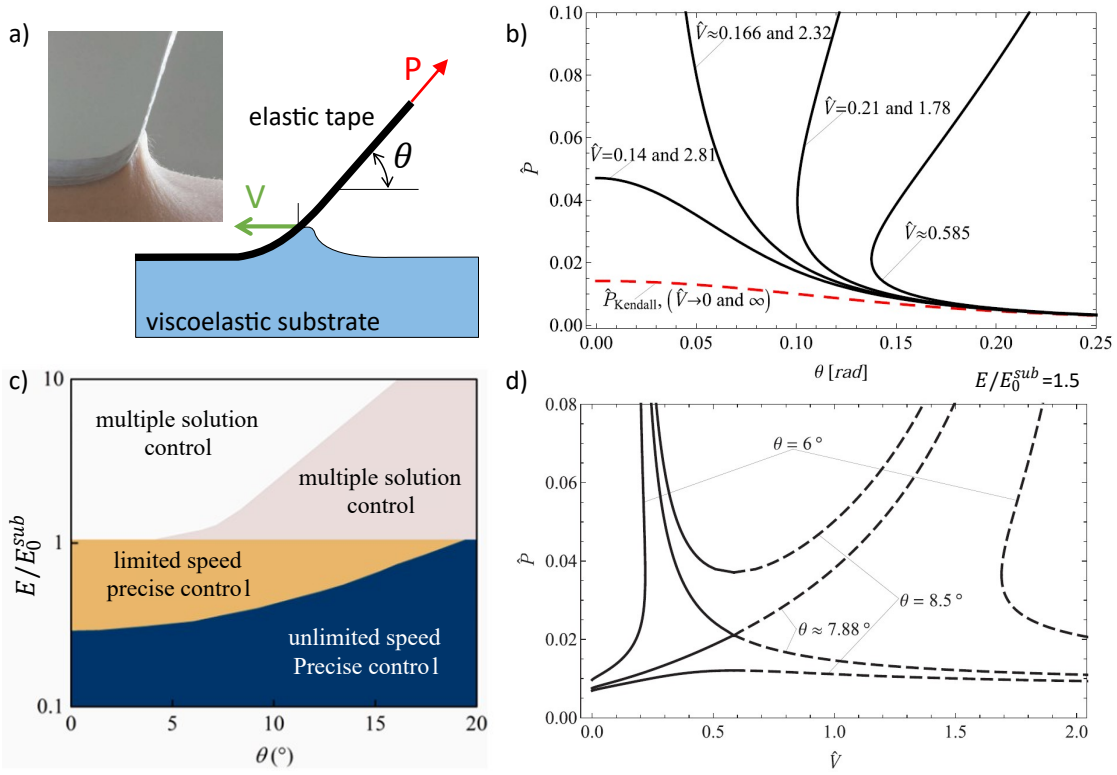

Figure 1.10: Peeling of an elastic tape from a viscoelastic substrate (a). The dimensionless peeling force $\hat{P} = P/Ewd$ is given as a function of the peeling angle θ (b) and the dimensionless detachment front velocities $\hat{V} = V\tau/d$ (d) (being E the tape's elastic modulus, w and d tape width and thickness, respectively, τ the substrate viscoelastic creep time). From [23]. (c) Phase diagram of control mode of peeling with considering the speed dependence of the work of adhesion. From [71]

the temperature may rise as effect of bulk and interfacial dissipation resulting in peculiar toughening effects and dynamic instabilities. These phenomena have been addressed by Carbone and Persson in two works on the crack motion in viscoelastic solids [72, 73]. They found that, during fracture propagation, the effective toughness exhibits a non-monotonic trend in relation to the crack velocity, characterized by the appearance of both local maxima and local minima which depend on the value of the thermal diffusivity (Fig. 1.11).
This outcome could be directly implicated in stick-slip behavior common in peeling systems [29–31]. Indeed, during crack propagation the available energy at the crack tip could result higher of the effective fracture energy. This extra energy is expressed as kinetic energy leading to an initial abrupt acceleration of crack. However, as velocity unstably increases the energy required for stable crack propagation overcome the available energy, resulting in the crack arrest. This cycle of events is then repeated.

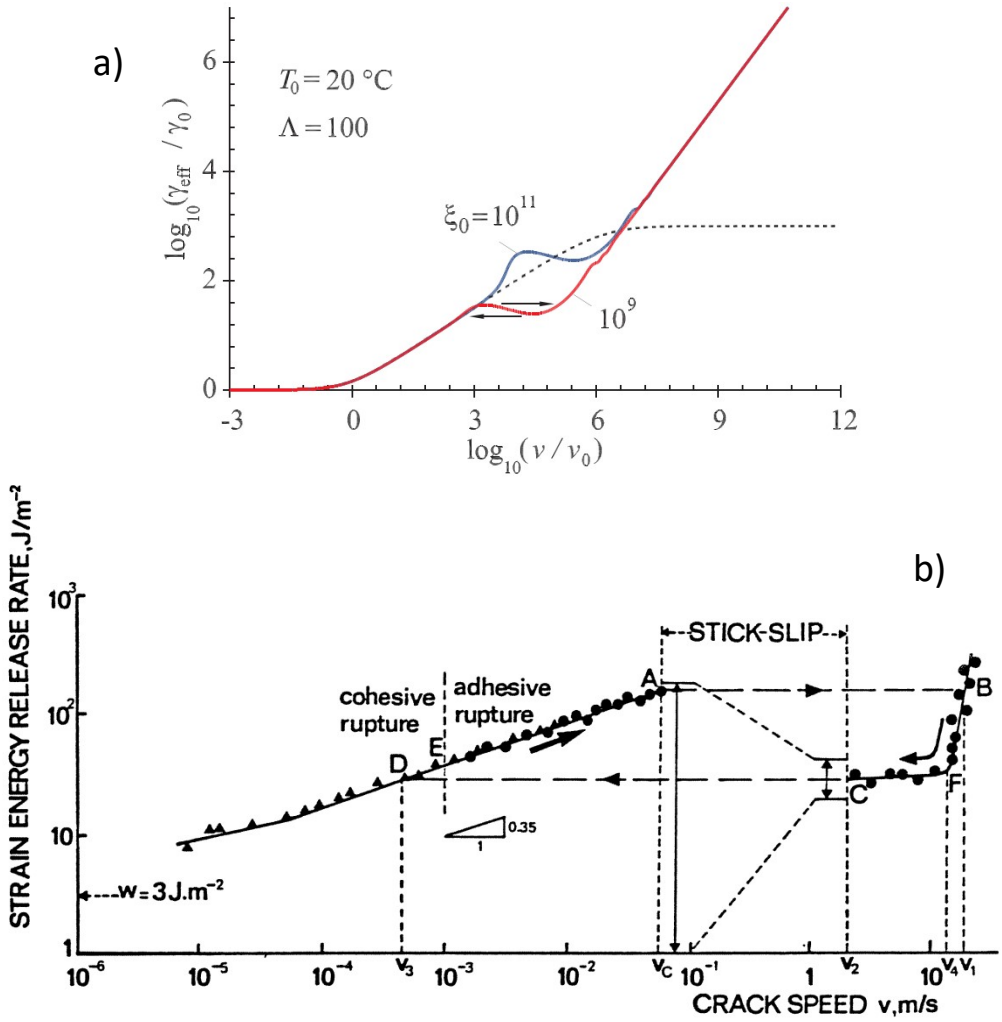

Figure 1.11: (a) The effective energy γ_{eff} to propagate the crack as a function of the crack velocity v for two different values of the dimensionless diffusivity ζ_0. The dashed line is obtained by neglecting the flash temperature effect.The non-monotonic behavior of the γ_{eff} may result in crack motion instability. From [72]. (b) Experimental energy release rate G function of the peeling rate. From [29]. Similar behavior is observed with respect of Carbone et Persson prediction.

1.2.3 Peeling geometries

Beside the intrinsic physical-chemical characteristics of surface interactions, it is widely acknowledged the fundamental role of geometry and topology in governing the behavior of peeling systems. This is particularly evident if we examine the remarkable adhesive mechanisms found in spiders, insects, and reptiles, directly involved in their exceptional locomotion performance. The appendages of these organisms exhibit a common pattern of fibrillar structures or hairs organized into multiple hierarchical levels (as depicted in Fig. 1.12). This arrangement enables them to achieve robust adhesion by conforming to diverse surface types, thereby

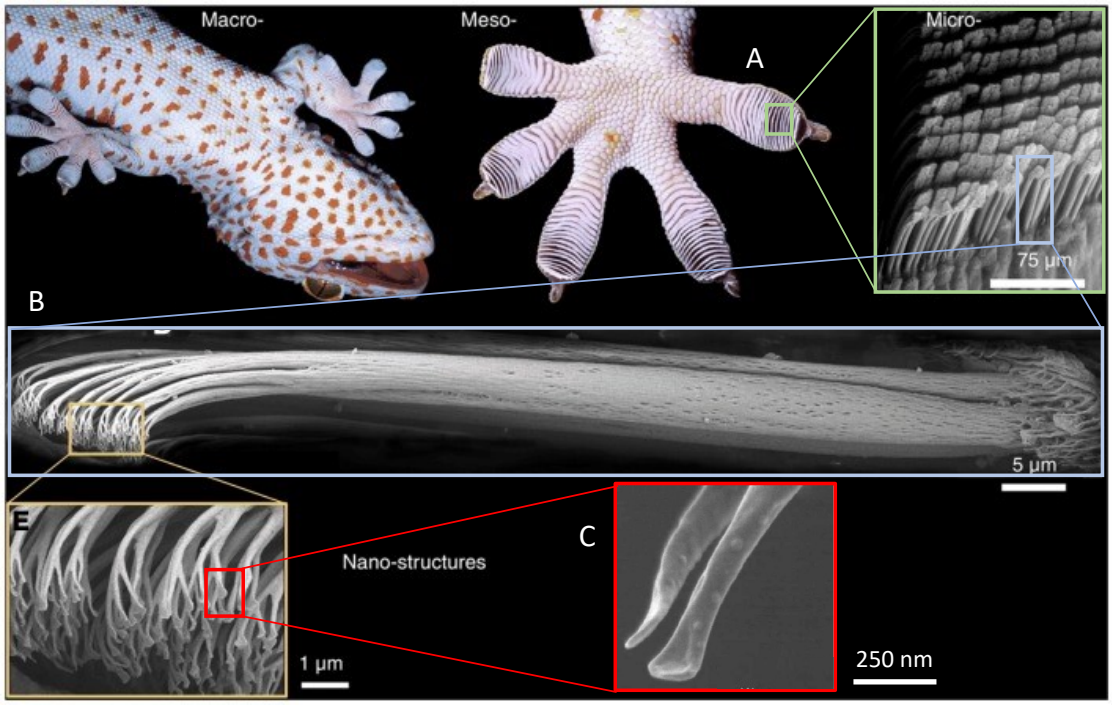

Figure 1.12: The hierarchical structure of gecko's pad. The toe pads consist of a series of lamellae (A) each of them covered with uniform arrays of thin, microscopic, hair-like structure called setae (B), which branch at the extremity in multiple nanoscopic spatulae terminations (C). Adapted from [36].

maximizing the contact area and facilitating the formation of chemical-physical bonds. While the highest-level hierarchical structures responsible for contact may significantly differ among species and vary considerably in size [2], the mechanism through which these adhesive structures adhere and detach remains consistent to a peeling mechanism. It has been proposed that the rapid detachment of their hierarchically structured extremities relies on the exploitation of simultaneous peeling processes, spanning from the macro-scale of the legs down to the nano-scale of the spatula pads [74]. Indeed, the peeling theory has been applied to interpret the adhesive forces exhibited by various animals across a broad spectrum of species and dimensions. This interpretation reveals a linear correlation between the weight of the organism and the total length of the peeling line (i.e., the sum of the widths of all individual spatula involved in the contact)(Fig. 1.13), accordingly with Rivlin's model Eq. (1.5) [2].

However, relying on single peeling models it could be not sufficient to completely capture the global attachment/detachment behavior of these animals. Developing the theory of multiple peeling [18], Pugno suggested that also the particular geometrical arrangement may play a key role. In this scenario, multiple peeling fronts coexist and the peeling angle is no longer an predetermined parameter but adapts accordingly with system characteristic. It is observed that an optimal peeling angle, at which adhesion is maximized, exists, and this configuration can be

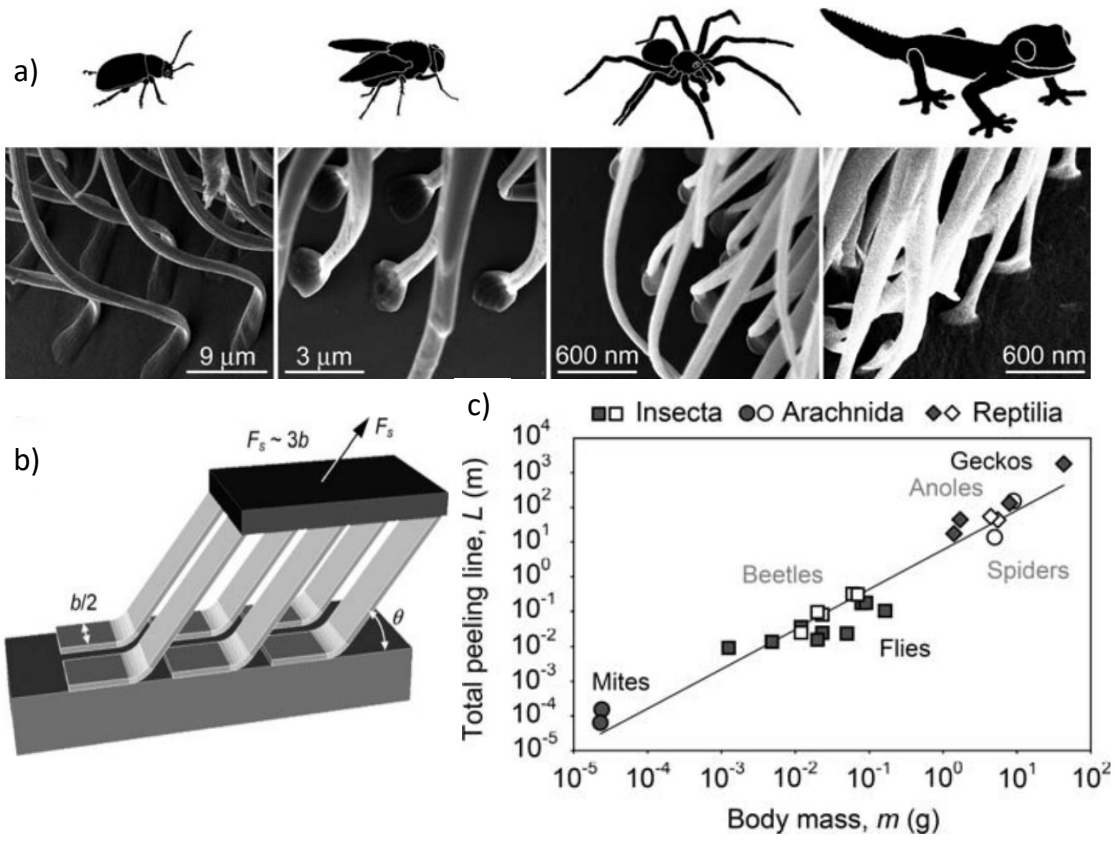

Figure 1.13: (a) Spatula structure of different animals. (b) Peeling scheme for multiple spatula adhesion. (c) Total peeling line versus the body mass of different animals; Rivlin's model fit well experimental data. Adapted form [2].

attained simply by increasing the tensile force [18].
Later, Lepore et Al. [75] showed that the angles assumed by Tokay geckos at the two characteristic sizes of feet and toe align excellently with Pugno's prediction of the maximal adhesion angle (Fig. 1.13a,b). Similarly, such "self-optimizing" configurations have also been observed in spiders' webs [76] and byssus thread networks of mussels [77], where the interplay between the peculiar system's geometrical arrangement and non-linear elastic response of the material has resulted in being a key factor for their superior adhesive performance which permits them to withstand the heavy action of wind and waves (Fig. 1.13e,f,g).
In a successive work Pugno and coworkers extended the multiple peeling theory to a hierarchical configurations [20]. Through FEM simulation they observed that increasing hierarchy increases the number of delamination points in the tape resulting in a distribution and reduction of the stresses at the interface. This helps in avoiding stress concentrations and an early onset of tape delamination. On the other hand, tape deformation and internal stresses are generally greater, and the displacement at full delamination is slightly smaller for hierarchical configurations with respect to the non-hierarchical tape (Fig. 1.13c,d).

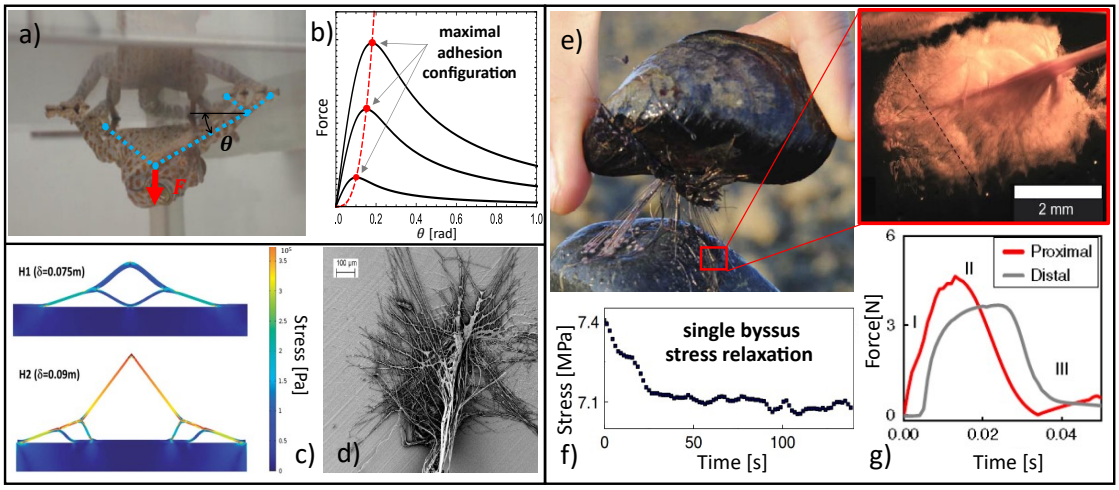

Figure 1.14: (a) V-peeling configurations in geckos at level of legs and digits. (b) Maximum adhesion configuration are observed. Adapted from [75]. (d) Hierarchical peeling geometries in spider web anchor [22] and (c) FEM simulation of stress distribution for two hierarchical levels [20]. (e) Mussels attached to a rock through byssus. (f) Viscoelastic behavior of a single byssus and (g) force vs. time within byssus threads under impact loading. Adapted from [77].

A strengthening effect has been also observed by Menga et. Al in investigating the V-peeling behavior of a thin elastic tape from an elastic substrate with finite [22] and non-finite thickness [66] (Fig. 1.15a). They found that an increase in the system delamination resistance could rise as a consequence of elastic interactions between adjacent peeling fronts. In particular an increasing of both the elasticity ratio between the Young's moduli of tape and substrate and the spatial periodicity produces strong enhancement of the defect tolerance of the system. Conversely, the peeling load can be minimized by tuning the substrate thickness and system periodicity suggesting that this configuration can represents an innovative optimization strategy to tailor the peel adhesion of several systems. Incidentally, we observe that such strengthening effect has been also reported for single peeling from elastic foundation where the influence of the peel arm bending is explicitly considered in the problem formulation [21].

However, the main important feature of multiple peeling propagation is its intrinsic unsteadiness involving continuous variation of system geometry and peeling force. Nonetheless, even in this case, a steady-state condition is usually achieved after sufficient time with a settling of a peeling force and peeling angle on an asymptotic value. In particular Afferrante et Al. [19] showed that the V-peeling propagation of an elastic tape is characterized by a monotonic increase of the pull-off force up to a critical value, above which an unstable delamination of occurs. Interestingly, in the same study, they reported the results for the circular peeling of a flat elastic membrane, where the mechanism of detachment differs significantly. In this case, the peeling line increases linearly with the radius of the detached area, resulting in a quasi-proportional increasing in the supported load

and a stable propagation behavior (Fig. 1.15b).

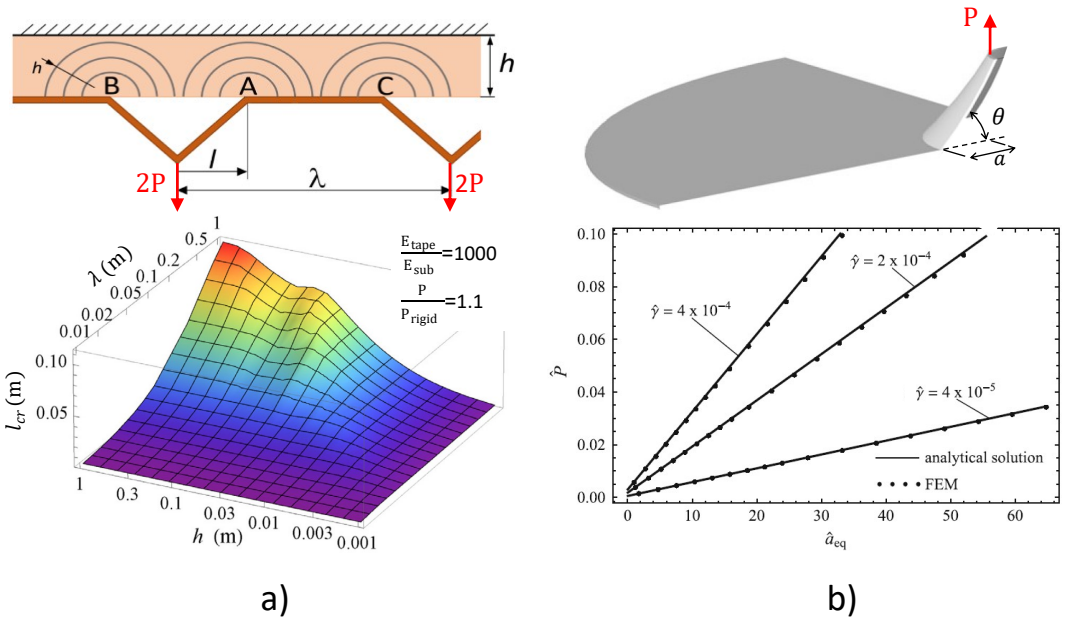

Figure 1.15: (a)The periodic V-peeling of an elastic tape from an elastic substrate with adjacent peeling fronts interacting. The effect of the peeling spatial periodicity λ and substrate thickness h on the critical detached length l_{cr}, at fixed load. From [66]. (b) Peeling of an axisymmetric membrane. The dimensionless peeling force $\hat{P}$ as a function of the dimensionless detached length $\hat{a}_{eq}$ for different values of the dimensionless work of adhesion $\hat{\gamma}$: analytical solution (solid lines) and FEM results (dots). From [19].

Moreover, it is worth to report that tests based on V-peeling and, in general, shallow peel angle configurations (e.g. ASTM Loop Tack test) are in some cases preferred over standard 90°-180° peel tests [46, 47] as they allow for a simplified set-up and reduce the possible effect of tape bending [16].

1.2.4 Slippage and friction effects

In peeling processes, evidences of slippage between film and substrate near the edge of the contact interface have been consistently observed in numerous experimental investigations [32, 34, 52, 78–82], suggesting that possible interfacial dissipative phenomena could be tightly involved in governing the adhesion strength exhibited in debonding processes largely exceeding predictions based on the sole reversible adhesion energy.

Mixed-mode fracture analysis

This problem has been approached in the context of a mixed-mode fracture framework where the contribute of interfacial frictional dissipation induced by slippage is not explicitly modeled but it is accounted in an mixed-mode interface toughness.

Here, the crack is subjected on a combination of two in-plane load states: tensile stress normal to the plane of the crack (Mode I), shear stress acting parallel to the plane of the crack and perpendicular to the crack front (Mode II). The phase angle is used to express which fracture mechanism in predominant in governing the crack propagation and is defined as

$$\psi = \tan^{-1}(K_{II}/K_I) \tag{1.14}$$

with K_I and K_{II} being the stress intensity factor for Mode I and Mode II, respectively. The mixed-mode approach was firstly proposed for modeling the crack propagation in layered structured by Suo and Hutchinson [83], and then formulated for peeling system by Thouless and Jensen [84]. In the case of peeling of thin elastic film from a infinite rigid substrate K_I and K_{II} are given by Collino et Al. [34]

$$\begin{cases} K_I = -\dfrac{P}{\sqrt{2d}}\cos\omega + \dfrac{\sqrt{6}M_0}{d^{3/2}}\sin\omega \\ K_{II} = -\dfrac{P}{\sqrt{2d}}\sin\omega - \dfrac{\sqrt{6}M_0}{d^{3/2}}\cos\omega \end{cases} \tag{1.15}$$

where P is peel force, d is the tape thickness, M_0 is the moment resultant acting at the crack tip and ω is a so-called phase factor depending on the elastic mismatch between solids (for a the peeling system considered $\omega = \pi/4$). Evaluating the moment M_0 in moderate rotation plate theory, the energy release rate results

$$G = \frac{P^2}{2Edw^2} + \frac{P}{2w}\theta^2 \tanh^2\left[\sqrt{\frac{12PL^2}{Ewd^3}}\right] \tag{1.16}$$

with w being the tape width, E the elastic modulus and L the length of the detached portion. Interesting, for very thin tapes, the bending contribution on the stress intensity factors is negligible and the phase angle resemble the definition given by Begley [85] specifically for peeling system $\psi = \tan^{-1}(P_x/P_y) = \pi/2 - \theta$, where $P_x = P\cos\theta$ and $P_x = P\sin\theta$ are the peel force component tangential and orthogonal to the substrate, respectively. Experimental results have shown that as the peeling angle decreases, an asymptotic increasing of the interface toughness emerges underling the dominant shear mode influence on the crack propagation (very low phase angle) associating with high frictional losses. However, for low θ (high ψ), K_I becomes negative resulting in a closed region immediately adjacent to the crack tip (see Fig. 1.16). Although, the authors present the possibility to extend the range of permissible phase angles to include region with negative K_I, they also emphasize the potential risk of surpassing the constraints of fracture mechanics. Indeed, it has been noted that, if for relatively stiff materials, frictional sliding occurs over very small distances compared with the feature dimensions of the system, when dealing with the peeling of soft tapes, sliding is no longer confined in a narrow zone close to the propagation front and could extend over larger length scales. In this case, the original assumptions underlying the standard fracture theory are violated, the toughness becomes specimen-dependent and the

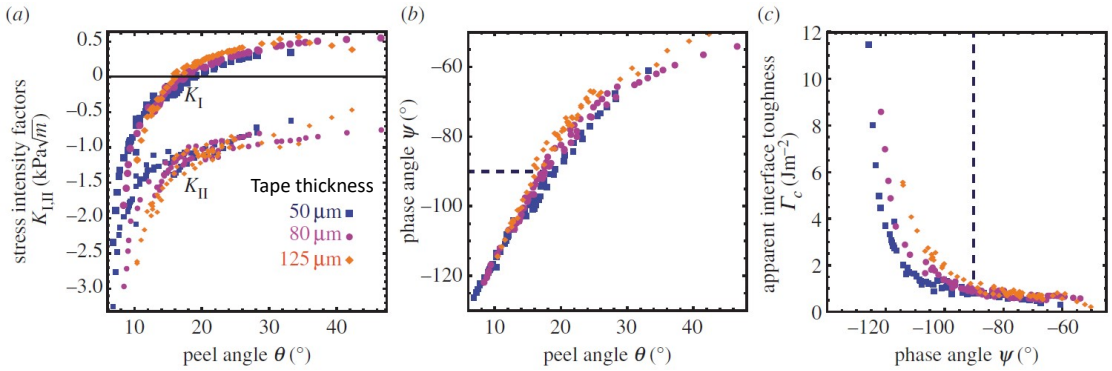

Figure 1.16: Mixed-mode fracture analysis of peeling. (a) Mode-I and mode-II stress intensity factors, (b) Phase angle and (c) apparent interface toughness as a function of phase angle evaluated from experimental peel force for three tapes with different thickness. From [34].

fracture process zone is influenced by behaviours outside the regions of K_I and K_{II} dominance. For this reason a certain skepticism about the validity of a mixed-mode approach lasts [16, 34, 85, 86].

Energy model for frictional peeling

Concurrently, energy based approaches have emerged effective in modeling slippage in peeling system. In this sense, the Kendall's formulation is extended by accounting for frictional losses generated in the contact region close to peeling front where a certain amount of slippage between tape and substrate arises. For soft materials, experimental analyses have demonstrated that the local interfacial shear stress f is independent on the contact pressure [87–89] and exhibits little to no dependence on the sliding velocity [90]. According with this evidences, uniform shear stress models have been proposed for single peeling [86, 91], wherein a linear displacement field within the sliding zone arises from the force equilibrium equation of plate elements $d\sigma/dx = -f/d$ between tensil σ and shear f stress. Such analysis results in a Kendall like expression in the form

$$\frac{P^2}{2Edw}(1-\cos^2\theta)+\frac{P}{d}(1-\cos\theta)=\Gamma w \tag{1.17}$$

where the additional term $P^2 cos^2\theta/2Edw$ emerges from frictional energy dissipation

$$U_F=-w\int_{-a}^{0}u(x)f\,dx \tag{1.18}$$

where $u(x)$ is the tape displacement field in the slippage zone of extension a.

Large deformations and V-peeling configuration have been later studied by Begley et Al. [34, 85] whose findings have been used for the interpretation of peeling experiments on a thin PDMS tape adhering to a glass substrate through van

der Waals interactions [34]. Across all these studies, it has been consistently observed that high peeling forces are reported for low peeling angles, far beyond the Kendall frictionless prediction (see Fig. 1.17a), reflecting the non-negligible role of frictional sliding in governing delamination strength of peeling systems. Moreover, through digital image correlation (DIC) the displacement field in the contact zone was measured, suggesting that sliding is likely confined to a region within two film thicknesses of the peel front, and that a strain exponential decay is well consistent with theoretical predictions derived from large deformation arguments (Fig. 1.17b). Similarly, a power low decay for displacements in sliding region

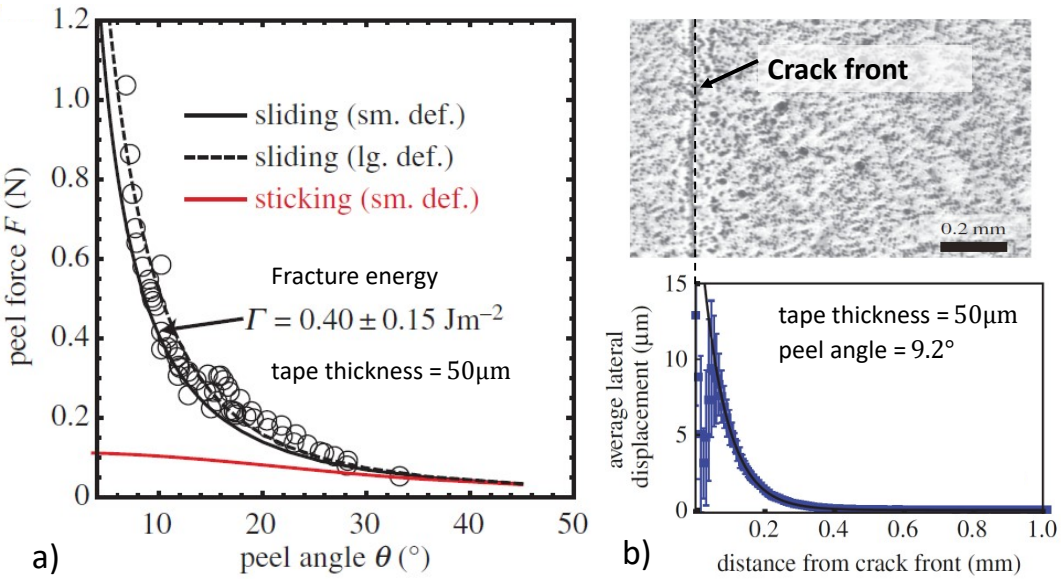

Figure 1.17: Peeling with frictional sliding interface. (a) Peel force as function of peeling angle: experimental data are compared with stuck and sliding models for small and large deformation. (b) Displacements in the adhered region of the film near the crack front measured via DIC and decay function fitting of the data. Adapted from [34].

has been predicted using a velocity-dependent shear stress model by Newby and Chaudhury [79] which well fitted measurements conducted using tapes marked with fluorescent particles. This same power law has been also observed in the relationship between peeling force and peel rate. Such a result suggests that interfacial frictional dissipation could be directly involved in the peel rate toughening effect commonly observed in peeling systems.

Chapter 2

Concepts of linear viscoelasticity

Viscoelastic materials exhibit an intermediate behavior between elastic solids and viscous fluids. Elastic materials can store mechanical energy when subjected to stress/strain actions. Their response does not depend on the dynamic of the excitation and, in the limit of linear elasticity, their behavior is just governed by the Young's modulus E which relates stress and strain through the well known Hooke's law $\sigma = E\varepsilon$. On the contrary, viscous fluids have the capacity for dissipating energy under non-hydro-static stress states, but not to store it. For many viscous fluids, the constitutive relation is described by Newton's law of viscosity $\sigma = \mu\dot{\varepsilon}$ (with μ being the viscosity coefficient). The combination of these two characteristics gives to viscoelastic materials a particular time-dependent behavior which is highly affected by the magnitude and the rate of the excitation they are subjected to.

Understanding and modeling viscoelasticity is of primary interest in several contexts ranging from biology, medicine to engineering. For instance, structural materials such as concrete, wood, stone, glass and metals naturally have a viscoelastic behavior which has to be accounted for during the design stage in order to prevent failure or collapse of structures as a result of excess deformation. This is crucial for the design, for instance, of seawall or asphalt subjected to static and dynamic loads respectively [92,93]. The marked viscoelastic response of metals at high temperatures must be considered in several applications including heat exchangers, furnace linings, boiler baffles, bolts at high temperatures, power plants, exhaust systems [94]. An example is represented by the turbine blades in jet engines subject to large tensile stress of centrifugal origin, and high temperature. The pursuit of ever higher performance achievable by forcing operation to higher temperatures has driven the development of specific cooling technologies and creep-resistant alloys [95].

The pursuit of ever higher performance, achieved by operating at increasingly higher temperatures, has driven the development of specific cooling technologies and creep-resistant alloys

Moreover, the capacity to recover strain exhibited from human tissues has been studied with the aim of developing specific treatment as in the case of abnormal head-shape correction in infants [96,97], for diagnostic purposes [98–100], or for the design of prostheses which can accurately reproduce the behavior of the original

biological structures they are replacing [101–103].

Moreover, studying viscoelastic mechanisms is important not just for understanding existing materials, but is also fundamental to guide the synthesis of new materials tailored on specific needs. In this aspect, polymers are probably the class of materials that stands out the most. Their chemical and mechanical behavior can be tuned by adjusting the chemical composition, molecular weight, and processing conditions [104, 105] to meet diverse industrial and scientific requirements. Look, for instance, at dumping materials used to design shock-absorbing elements (e.g. in helmets or vehicles' structure), reducing noise and vibration [106–108]. Moreover, rubbery materials are commonly used for seals and gaskets to prevent leakage of fluids. Thanks to their deformability and viscoelasticity can adapt to changing of gap between components securing sealing and reducing stress or frictional losses in case of sliding joints [109–111]. Tapes, and in particular adhesive tapes, represent a noteworthy application of tailored viscoelastic properties both at the level of the tape material and adhesive itself. These tapes are designed with specific characteristics which enable a solid adhesion while maintaining flexibility and durability. Understanding their viscoelastic behavior is essential for optimizing performance in packaging, construction, or even medical applications like wound dressings.

In this chapter we will present the most important notions and mathematical models for linear viscoelasticity that will be used for the formulation of the viscoelastic tapes peeling behavior.

2.1 Creep and Stress-relaxation

The main features of a viscoelastic response can be draw through a simple step excitation analysis. Consider a viscoelastic material subjected to a step stress $\sigma(t)$ applied at time $t = 0$ with magnitude σ_0; this can be mathematically expressed as

$$\sigma(t) = \mathcal{H}(t)\sigma_0 \tag{2.1}$$

where $\mathcal{H}(t)$ is the Heaviside step function defined as

$$\mathcal{H}(t) = \begin{cases} 0 & \text{if } x < 0 \\ 1 & \text{if } x \geq 0 \end{cases} \tag{2.2}$$

In a viscoelastic material the strain is observed increasing with time. This effect is called *Creep*, namely the deformation of a material undergone constant load. Thus the relation between load and deformation can be expressed through creep compliance (or creep function) $\mathcal{J}(t)$ as

$$\varepsilon(t) = \mathcal{J}(t)\sigma_0 \tag{2.3}$$

This behavior is graphically depicted in Fig.

Consider now to apply a step strain ε of magnitude ε_0 was time history is described by

$$\varepsilon(t) = \mathcal{H}(t)\varepsilon_0 \tag{2.4}$$

In a viscoelastic material a *stress relaxation*, thus a gradual decrease of stress when the material is held at constant strain, is observed. This is shown in Fig. 1.7b Now, a Hooke-like equation describes the stress-strain relation

$$\sigma(t) = \mathcal{R}(t)\varepsilon_0 \tag{2.5}$$

with $\mathcal{R}(t)$ being the relaxation modulus (or relaxation function), which can be interpreted as a time-dependent elastic modulus.

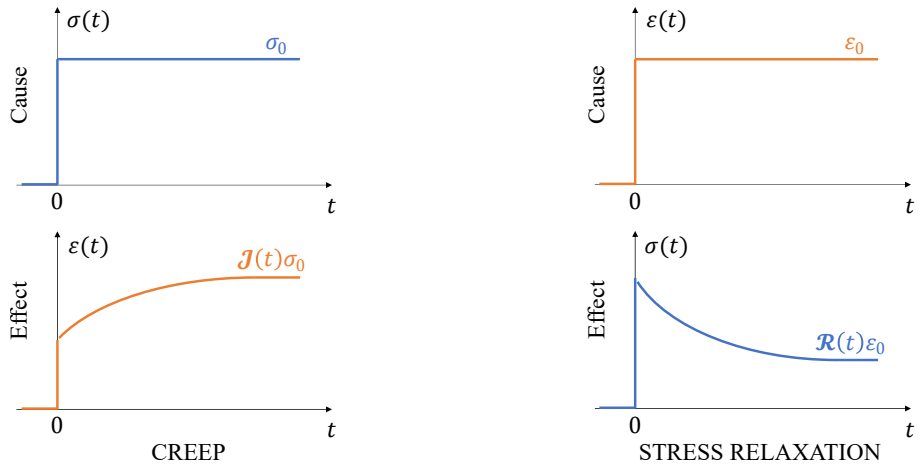

Figure 2.1: Typical viscoelastic response to step excitation. (a) Creep and (b) stress relaxation.

In a linear viscoelastic material both creep compliance $\mathcal{J}$ and relaxation function $\mathcal{R}$ are assumed independent of stress and strain level respectively and are function of time alone.

2.2 Boltzmann superposition principle

Step excitation experiments are also used to model and characterize the a linear viscoelastic material. The response to any stress or strain history can be extended from a simple step response by means of the Boltzmann superposition principle, which states that the effect of a compound cause is the sum of the effects of the individual causes. Consider a response $y(t)$ to a generic input $x(t)$ described by a linear operator $\mathcal{L}$ as

$$y(t) = \mathcal{L}\{x(t)\} \tag{2.6}$$

which satisfy the following assumptions:

- **Linearity**: the output generated from a linear combination of inputs can be expressed as a linear combination of the outputs of single inputs

$$ax_1(t) + bx_2(t) = a\mathcal{L}\{x_1(t)\} + b\mathcal{L}\{x_2(t)\} = ay_1(t) + by_2(t) \tag{2.7}$$

- **Time invariance**: the output signal does not depend on the absolute time. In other words, if for some input signal $x(t)$ the output signal is $y_1(t) = \mathcal{L}\{x(t)\}$, then a time-shift of the input signal creates a time-shift on the output signal, i.e.

$$y_2(t) = \mathcal{L}\{x(t - t_0)\} = y_1(t - t0) \tag{2.8}$$

- **Casuality**: the output of the system does not depend on future inputs, but only on past input. It is the cause-effect principle which governs real physical phenomena.

We consider now a linear viscolastic material where all these assumptions are assumed fullfilled. The response to a generic deformation $\varepsilon(t)$ is a stress $\sigma(t)$ given by

$$\sigma(t) = \mathcal{L}\{\varepsilon(t)\} \tag{2.9}$$

Suppose the deformation being a linear combination of step signal of magnitude ε_k occurring at time t_k, thus

$$\varepsilon(t) = \sum_k \varepsilon_k \mathcal{H}(t - t_k) \tag{2.10}$$

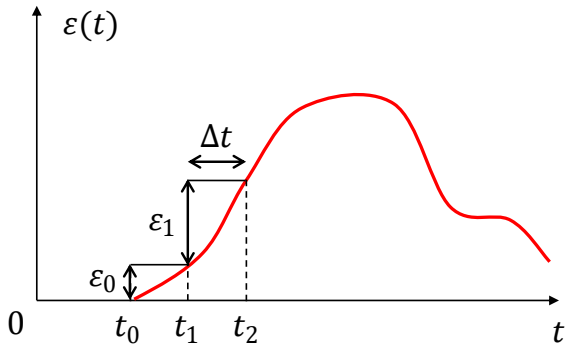

Figure 2.2: Decomposition of a continuous strain signal into step functions.

See now Fig. 2.2. An arbitrary signal can be decomposed into step functions occurring with uniform time-steps Δt. With reference to a step strain, in the limit of $\Delta t \to 0$, a continuous signal is obtained as

$$\varepsilon(t) = \sum_k \dot{\varepsilon}(t_k)\mathcal{H}(t - t_k)\Delta t \tag{2.11}$$

For the linearity and time invariance principles we can write the stress response $\sigma(t)$ as

$$\sigma(t) = \mathcal{L}\left\{\sum_k \dot{\varepsilon}(t_k)\mathcal{H}(t - t_k)\Delta t\right\} = \sum_k \dot{\varepsilon}(t_k)\mathcal{L}\{\mathcal{H}(t - t_k)\}\,\Delta t \tag{2.12}$$

From Eq. (2.5), the viscoelastic response to a unitary step-strain is expressed by the relaxation modulus; the last equation becomes

$$\sigma(t) = \sum_k \dot{\varepsilon}(t_k)\mathcal{R}(t - t_k)\Delta t \tag{2.13}$$

Finally, since $\Delta t \to 0$, passing to integrals we obtain

$$\sigma(t) = \int_{-\infty}^{t} \mathcal{R}(t - \tau)\dot{\varepsilon}(\tau)d\tau \tag{2.14}$$

Following the same arguments, the strain response to a generic stress input is given by

$$\varepsilon(t) = \int_{-\infty}^{t} \mathcal{J}(t - \tau)\dot{\sigma}(\tau)d\tau \tag{2.15}$$

Eqs. (2.14,2.15) let us to obtain the viscoleastic response to an arbitrary input history as a function of a convolution where the kernel is represented by the step-input response. Note that the Bolzamann superposition is not just valid for input expressed as a combination of step-signals, but is valid for every input ascribable to a sum of elementary functions (ramp, sine, cosine, etc.). For each elementary functions will correspond a different kernel $\mathcal{L}(t)$.

2.3 Rheological models

To comprehend and characterize the complex viscoelastic behavior, a common approach relies on the use of rheological models. These models serve as tools for quantifying the response of viscoelastic materials to external forces, temperature variations, and time-dependent deformations. In particular, the use of discrete mechanical element like Hookean springs (elastic element), and Newtonian dashpots (pure viscous element), combined in series or parallel has resulted powerful for this purpose.

2.3.1 Voigt model

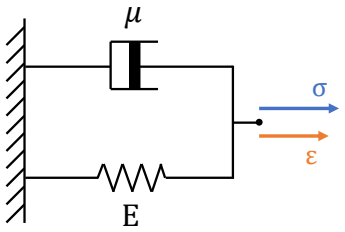

Figure 2.3: Scheme of the Voigt model

The Voigt model represented in Fig. (2.3) consists of spring and dashpot in parallel so that they both experience the same strain ε and the total stress σ is the sum of the stress in each element.

$$\begin{cases} \sigma = \sigma_{el} + \sigma_{vis} \\ \sigma_{el} = E\varepsilon \\ \sigma_{vis} = \mu\dot{\varepsilon} \end{cases} \tag{2.16}$$

Assuming the strain being an unit step-function $\varepsilon(t) = \mathcal{H}(t)$, the response of the system represent the relaxation function, so that

$$\mathcal{R}(t) = E\mathcal{H}(t) + \mu\delta(t) \tag{2.17}$$

where we have used $\dot{\mathcal{H}}(t) = \delta(t)$.

Consider now a unit step change of stress $\sigma(t) = \mathcal{H}(t)$ is applied, so that the strain response of the system represents the creep function. From Eq. (2.16) we have

$$\mu\dot{\mathcal{J}}(t) + E\mathcal{J}(t) = \mathcal{H}(t) \tag{2.18}$$

Since this is a first-order complete linear differential equation, the general solution $\mathcal{J}$ is obtained by adding the general solution of the associated homogeneous equation $\mathcal{J}_o$ to the particular solution $\mathcal{J}_p$

$$\mathcal{J}(t) = \mathcal{J}_o(t) + \mathcal{J}_p(t) \tag{2.19}$$

Without entering in details, the homogeneous equation has the note solution

$$\mathcal{J}_o(t) = Ae^{-\frac{t}{\tau}} \tag{2.20}$$

where we have defined the creep time $\tau = \mu/E$, and A is a constant we will find by imposing initial conditions. The particular solution can be found by observing that, after sufficiently time ($t \to \infty$) the stress application the system achieve an equilibrium condition ($\dot{\mathcal{J}} = 0$) where the contribution of the dashpot is null and only the elastic element reacts to the applied stress; from Eq. (2.18) we have

$$\mathcal{J}_p(t) = \frac{1}{E} \tag{2.21}$$

We fulfill the Cauchy problem noticing that, just after the stress application $\mathcal{J}(0^+) = 0$, as the dashpot avoids instantaneous deformations. Solving Eq. (2.20), we obtain the value of the constant $A = -1/E$.

Without formalism, for $t \geq 0$, the relaxation and creep functions of the Voigt model are, respectively

$$\begin{cases} \mathcal{R}(t) = E + \mu\delta(t) \\ \mathcal{J}(t) = \dfrac{1}{E}\left[1 - e^{-\frac{t}{\tau}}\right] \end{cases} \tag{2.22}$$

In Fig. 3.4a are shown creep and relaxation function for the Voigt model. It is important to notice that, the creep time $\tau = \mu/E$ is the characteristic time of

the system, so that the viscoelastic behavior of the system appears just on time scales in the order of $t \approx \tau$. For $t \ll \tau$, the Voigt model response is almost rigid as $\mathcal{J} = 0$. Moreover, at time $t = 0$, the relaxation function diverges as the dashpot requires infinite stress to be stretched instantaneously. For this reasons, this model is unable to properly represent the elastic behavior of a viscoelastic material at short time. Whereas, for longer time scales the creep behavior arises, and the response became purely elastic for $t \gg \tau$.

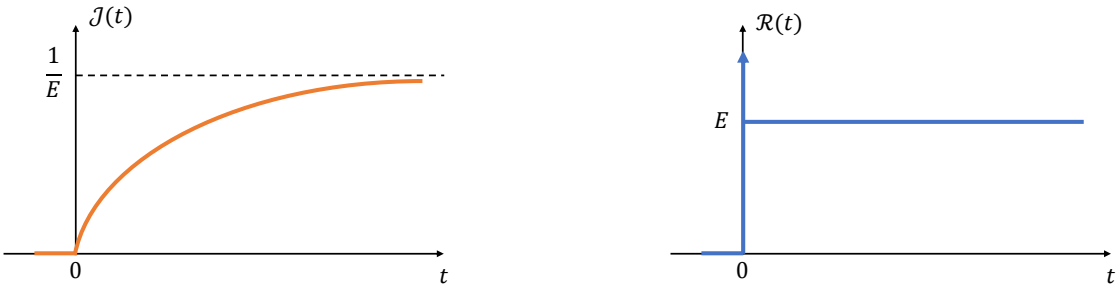

Figure 2.4: Creep function $\mathcal{J}(t)$ (a) and stress relaxation function $\mathcal{R}(t)$ (b) for the Voigt model.

2.3.2 Maxwell model

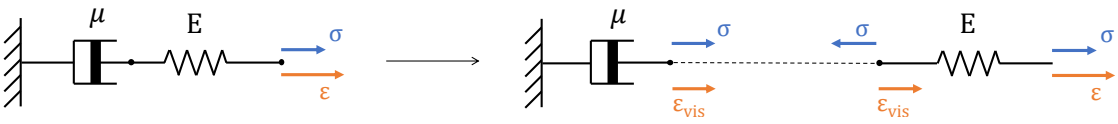

Figure 2.5: Scheme of the Maxwell model

The Maxwell model consists of a spring and a dashpot in series (see. Fig. 2.5). Here, each element is subjected to the same force, thus

$$\begin{cases} \sigma = \sigma_{el} = \sigma_{vis} \\ \sigma_{el} = E\varepsilon_{el} \\ \sigma_{vis} = \mu\dot{\varepsilon}_{vis} \end{cases} \tag{2.23}$$

where $\varepsilon_{el} = \varepsilon - \varepsilon_{vis}$ and ε_{vis} are the deformations of the elastic and dashpot elements, respectively. Derivating with respect of time σ_{el}, and substituting $\dot{\varepsilon}_{vis}$ given from σ_{vis} we obtain

$$\begin{cases} \dot{\sigma} = E(\dot{\varepsilon} - \dot{\varepsilon}_{vis}) \\ \dot{\varepsilon}_{vis} = \dfrac{\sigma}{\mu} \end{cases} \rightarrow \quad \dot{\sigma} + \frac{E}{\mu}\sigma = E\dot{\varepsilon} \tag{2.24}$$

Consider firstly a unit step of deformation as input $\varepsilon(t) = \mathcal{H}(t)$ so that the stress response represents the relaxation function of the model. We have

$$\dot{\mathcal{R}}(t) + \frac{E}{\mu}\mathcal{R}(t) = E\dot{\mathcal{H}}(t) = E\delta(t) \tag{2.25}$$

With similar arguments to those provided above, we have

$$\mathcal{R}_o(t) = Ae^{-\frac{t}{\tau}} \tag{2.26}$$

with $\tau = \mu/E$ being the relaxation time. Whereas for the particular solution $\mathcal{R}_p(t)$ observe that, after sufficient time ($t \to \infty$), all the imposed deformation has been recovered by the dashpot and the system is completely relaxed so that

$$\mathcal{R}_p(t) = 0 \tag{2.27}$$

Considering that at time $t = 0^+$, since the dashpot acts as a rigid body to impulsive deformation, the strain is entirely absorbed by the elastic element so that $\mathcal{R}(0^+) = E$; it results $A = E$. The relaxation function for a Maxwell model is given by

$$\mathcal{R}(t) = Ee^{-\frac{t}{\tau}} \tag{2.28}$$

Consider now the system is excited by a unit step stress $\sigma(t) = \mathcal{H}(t)$. The strain response represent the creep function of the model; Eq. (2.25) becames

$$\dot{\mathcal{J}}(t) = \frac{1}{E}\dot{\mathcal{H}}(t) + \frac{1}{\mu}\mathcal{H}(t) \tag{2.29}$$

which integrated gives

$$\mathcal{J}(t) = \mathcal{H}(t)\frac{1}{E}\left[1 + \frac{t}{\tau}\right] + A \tag{2.30}$$

Since $\mathcal{J}(0^+) = 0$, $A = 0$.

Without formalism, for $t \geq 0$, the relaxation and creep function are, respectively

$$\begin{cases} \mathcal{R}(t) = Ee^{-\frac{t}{\tau}} \\ \mathcal{J}(t) = \dfrac{1}{E}\left[1 + \dfrac{t}{\tau}\right] \end{cases} \tag{2.31}$$

In Fig. (4.4) are shown the creep and relaxation function for the Maxwell model. Note that this model provides a vanishing residual stress for $t \to \infty$, so that all the imposed deformation is dissipated in the dashpot. For short time scale this model acts as an elastic solid. When subjected to a constant stress, Maxwell model behaves like a viscous fluid showing a continuous deformation with a constant rate equal to $1/\mu$.

2.3.3 Standard linear model

Since both Voigt and Maxwell model have limits in properly represent the viscoleastic behavior at short or long time scale, respectively, combinations of both models have been proposed to better represent the viscoelastic response. The standard linear solid (SLS) model shown in Fig. (2.7) is based on an elastic element in parallel with a Maxwell element.

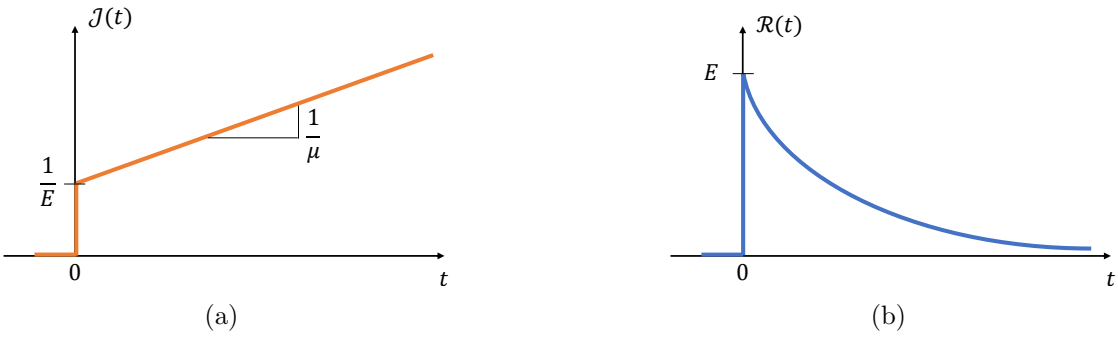

Figure 2.6: Creep function $\mathcal{J}(t)$ (a) and stress relaxation function $\mathcal{R}(t)$ (b) for the Maxwell model.

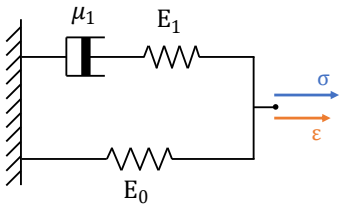

Figure 2.7: Scheme of standard linear solid model (SLS), Maxwell representation.

Relaxation function

We consider firstly the relaxation function of the system $\mathbf{R}(t)$. For this model, each element is subjected to the same strain $\varepsilon(t) = \mathcal{H}(t)$, so that the total stress is the sum of the stress in each branch. Recalling the relaxation function for the Maxwell model (Eq. (2.34)), we have

$$\begin{aligned} \mathcal{R}(t) &= \mathcal{R}_0(t) + \mathcal{R}_1(t) = \\ &= E_0 + E_1 e^{-\frac{t}{\tau}} \end{aligned} \tag{2.32}$$

Often, it is useful referring to the material stiffness exhibited at short time scale $t \to 0$ (fast excitation) E_∞ and long time scale $t \to \infty$ (slow excitation) E_0. Note that subscript refers to the excitation frequency. For very fast excitation it results $E_\infty = E_0 + E_1$, so that

$$\mathcal{R}(t) = E_0 + (E_\infty - E_0) e^{-\frac{t}{\tau_r}} \tag{2.33}$$

Observe that the relaxation time is $\tau_r = \mu / E_1 = \mu / (E_\infty - E_0)$.

Creep function

The creep function of the system will be given by a step function as stress input. By considering the components in each branch of the system, it is possible to write

$$\begin{cases} \sigma_0(t) = E_0\varepsilon_0 \\ \sigma_1(t) = E_1\varepsilon_{1,el} \\ \sigma_1(t) = \mu\dot{\varepsilon}_{1,vis} \\ \sigma(t) = \sigma_0(t) + \sigma_1(t) \end{cases} \tag{2.34}$$

with $\sigma(t) = \mathcal{H}(t)$ and $\varepsilon(t) = \mathcal{J}(t)$. After some algebraic calculations involving transformations already seen previously (see Section 2.3.2), we get the following differential equation

$$E_\infty \frac{\mu_1}{E_1}\dot{\mathcal{J}}(t) + E_0\mathcal{J}(t) = \frac{\mu_1}{E_1}\dot{\mathcal{H}}(t) + \mathcal{H}(t) \tag{2.35}$$

By substituting $\tau = \mu_1/E_1$, and defining the viscoelastic factor κ as

$$\kappa = \frac{E_\infty}{E_0} \tag{2.36}$$

we obtain

$$\dot{\mathcal{J}}(t) + \frac{1}{\kappa\tau}\mathcal{J}(t) = \frac{1}{E_\infty}\left[\delta(t) + \frac{1}{\tau}\mathcal{H}(t)\right] \tag{2.37}$$

Also in this case we can obtain the solution as the sum of the homogeneous and particular solutions; we have

$$\mathcal{J}_o(t) = Ae^{-\frac{t}{\kappa\tau}} \tag{2.38}$$

As after sufficiently time the dashpot is completely relaxed, all the deformation is sustained from the elastic element, thus the particular solution can be given as

$$\mathcal{J}_p(t) = \frac{1}{E_0} \tag{2.39}$$

The constant A is obtained imposing the initial condition. For $t \to 0^+$ the system reacts to the step strain as the parallel of the springs E_0 and E_1 so that

$$\mathcal{J}(0^+) = \frac{1}{E_0 + E_1} = \frac{1}{E_\infty} \tag{2.40}$$

We finally get the relaxation function

$$\mathcal{J}(t) = \frac{1}{E_0} + \left(\frac{1}{E_\infty} - \frac{1}{E_0}\right)e^{-\frac{t}{\tau_c}} \tag{2.41}$$

with $\tau_c = \kappa\tau$ being the creep (or retardation) time.

Observe that the creep time is not equal to the relaxation time but it is larger. The ratio of creep to relaxation times depends on the relaxation strength Δ, which, in terms of creep compliance, is given by the general form [112]

$$\Delta = \frac{\mathcal{J}(\infty) - \mathcal{J}(0)}{\mathcal{J}(0)} \tag{2.42}$$

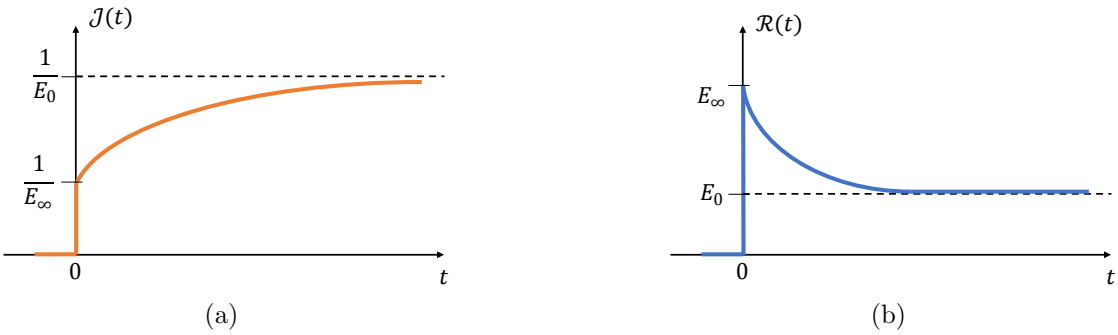

Figure 2.8: Creep function $\mathcal{J}(t)$ (a) and stress relaxation function $\mathcal{R}(t)$ (b) for the Standard solid model in Maxwell representation.

so,

$$\tau_c = \tau_r(1 + \Delta) = \kappa\tau_r \tag{2.43}$$

In Fig. 4.6 are shown trend of $\mathcal{J}(t)$ and $\mathcal{R}(t)$ for a SLM. This model is able to capture the typical viscoelastic behavior at both small and long time scales. Indeed, the creep function exhibit a step change for $t = 0$ as soon the stress is applied (pure elastic behavior), followed by a finite increase during the creep stage until the asymptotic limit is achieved $1/E_0$ where the system behaves as a solid but with lower stiffness. For the relaxation we observe the highest value E_∞ for $t = 0$, when all the elastic component of the system is stressed. For increasing time, a stress relaxation toward the asymptotic value E_0 occurs, so that the system maintains an elastic response.

Generalized SLS model

This model based on the simple combination of one Maxwell and one elastic element shows a single characteristic time so that undergoes creep and relaxation over about one decade in time scale. In fact, real viscoelastic materials relax and creep over many decades. In order to account for this behavior, starting from the SLS model a more general model can be considered where several Maxwell element are combined in parallel with a pure elastic element (see Fig. 2.9). In particular, when the input force or displacement occurs, only a few Maxwell branches are involved in the system response: only those having a characteristic time of the same order of magnitude of the frequency of the input; not all the time scales are then considered. The relaxation and creep function for these general models can be expressed with the following series as a combination of the response of each element

$$\begin{cases} \mathcal{R}(t) = E_0 + \sum_k E_k e^{-\frac{t}{\tau_k}} \\ \mathcal{J}(t) = \frac{1}{E_0} + \sum_k \frac{1}{E_k}\left(1 - e^{-\frac{t}{\tau_k}}\right) \end{cases} \tag{2.44}$$

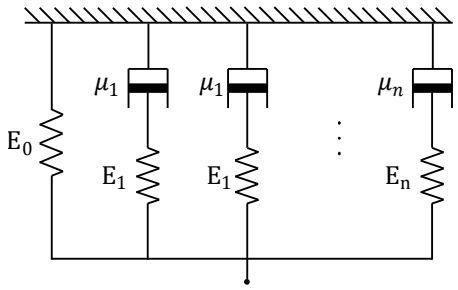

Figure 2.9: Scheme of generalized SLS model in Maxwell representation.

Chapter 3

Peeling of viscoelastic tapes: the role of frictional sliding

Following evidences of sliding between tape and substrate near the crack front during peeling propagation [32,34,80,82], many studies have tried to consider this behavior relying on mode-mixity approaches or energy based formulation which extends Kendall's original model by accounting for frictional dissipation energy contribution (refer to Section 1.2.4 for a more comprehensive discussion,). In the latter scenario, this problem has been addressed within the context of linear elasticity considering both small and large deformations, as well as single and V-peeling configurations [34,81,85,91]. Theoretical and experimental investigations have consistently concluded that, as expected, the presence of frictional sliding at the interface enhances the peeling resistance of the system, resulting in higher peeling forces, which may theoretically diverge at vanishing peeling angles. Nevertheless, while this dissipation mechanism appears to be pivotal for gaining a deeper understanding of peeling phenomena, it is often ignored and it has not been comprehensively explored, particularly when combined with the viscoelastic material response commonly exhibited by polymer tapes frequently employed in peeling processes.

In this chapter, we present a theoretical model of the behavior of a thin viscoelastic tape peeled away from a rigid substrate. Specifically, we aim at investigating the combined effect of frictional interfacial sliding occurring during the detachment process and the energy dissipation associated with the viscoelastic behavior of the tape. In order to better outline the interplay between these mechanisms of energy dissipation, two models will be discussed: (i) stuck model, where a rigid constraint avoids any possible interfacial displacement between the tape and the substrate, so that no additional energy contribution is present at interface beside the change in the energy of adhesion; then (ii) we consider the sliding case, where energy dissipation occurs due to frictional relative sliding in the tape elongated region.

3.1 Stuck model

We consider a viscoelastic tape of thickness d and transverse width w (cross-section $At = wd$), baked onto a rigid substrate with no relative sliding at the interface. As shown in Fig. 4.1, the tape is peeled away at an angle θ under a constant force P. We assume a stationary peeling process, with the propagation front moving on the left at a constant velocity v_c relative to the substrate. Conveniently, the process is observed in the peeling front, so that the substrate moves on the right at speed v_c as shown in Fig. 4.1.

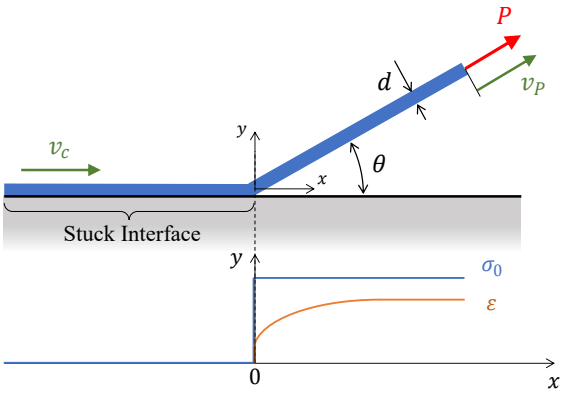

Figure 3.1: The scheme of the peeling process of a thin viscoelastic layer from a rigid substrate in the presence of stuck adhesion at the interface, so that no relative sliding occurs. In the lower part, qualitative diagrams of the tape stress σ (red) and deformation ε (blue) are shown.

Under steady state conditions, the Griffith criterion for the peeling condition can be referred to an energy balance per unit time in the form

$$W_E + W_I + W_S = 0 \tag{3.1}$$

where W_E is the work per unit time of the external forces acting on the tape, W_I is work per unit time done by tape internal stresses, which takes into account for both the change in the stored elastic and viscous energy dissipation in the tape, and W_S is the work per unit time done by interfacial forces. Notably, in this formulation we neglect any other source of energy dissipation, such as acoustic or thermal emissions.

The term W_E in Eq. (3.1) can be calculated considering the external forces acting on the system, which are the remote load P acting on the detached tape tip, and the corresponding opposite substrate reaction force $-P\cos\theta$ acting on the peeling front. We have

$$W_E = Pv_P - Pv_c\cos\theta = \sigma_0 v_c A_t \left(1 + \frac{\sigma_0}{E_0} - \cos\theta\right) \tag{3.2}$$

where we defined $\sigma_0 = P/A_t$, and E_0 is the low frequency viscoelastic modulus. Moreover, the mass balance of the tape gives $v_P = v_c(1 + \sigma_0/E_0)$. Notably, in

Eq. (3.2) we assumed that the tape tip (where the force P is applied) is located sufficiently far from the peeling front, so that complete viscoelastic relaxation occurs in the detached tape.

The surface term W_S in Eq. (3.1) represents the energy per unit time associated with the rupture of interfacial adhesive bond. Although the work of adhesion may also depend on the peeling rate as effect of dissipative surface phenomena (see Chapter 1), in this model we neglect such effects, thus assuming a constant work of adhesion independent on v_c coinciding with the Duprè adhesion energy γ. Therefore, we can write

$$W_S = -w\gamma v_c \tag{3.3}$$

As mentioned above, the term W_I in Eq. (3.1) takes into account for both the elastic energy stored in the tape, and the bulk energy dissipation occurring due to viscoelastic creep in the detached strip. Moreover, observing that the bending stiffness of the tape depends on the third power of thickness d, and considering that we focus on very thin tapes, the bending contribution to W_I can be neglected (see also Refs. [25, 113]). Hence we write

$$W_I = -v_c A_t \int_{-\infty}^{+\infty} \sigma(x)\varepsilon'(x)\, dx \tag{3.4}$$

where $\varepsilon'(x)$ is the spatial derivative of the strain $\varepsilon(x)$. Note that, in Eq. (3.4), we used $\dot{\varepsilon}(x) = v_c\varepsilon'(x)$, with $\dot{\varepsilon}(x)$ being the time derivative of $\varepsilon(x)$.

Since in this section we assume no interfacial sliding between the adhering tape and the rigid substrate, the stress distribution in the viscoelastic tape can be given by $\sigma(x) = \sigma_0\mathcal{H}(x)$, with $\mathcal{H}(x)$ being the Heaviside step function (see the diagram in Fig. 4.1). In the framework of linear viscoelasticity and steady state conditions, the deformation field can be calculated as (see Chapter 2)

$$\varepsilon(x) = \int_{-\infty}^{x} \mathcal{J}(x-s)\sigma'(s)\, ds \tag{3.5}$$

where $\mathcal{J}(x)$ is the spatial transformation of the viscoelastic creep function, that for a single creep time τ, is given by

$$\mathcal{J}(x) = \frac{1}{E_0} - \frac{e^{-x/\lambda}}{E_1} \tag{3.6}$$

where $\lambda = v_c\tau$ is the creep length, and $E_1^{-1} = E_0^{-1} - E_\infty^{-1}$ with E_0 and E_∞ being the low and very high frequency viscoelastic moduli, respectively. For the case at hand, Eq. (3.5) gives $\varepsilon(x) = \sigma_0\mathcal{J}(x)$, which substituting into Eq. (3.4), after some algebra, gives

$$W_I = -v_c A_t\sigma_0^2\left(\frac{1}{E_0} - \frac{1}{2E_\infty}\right) = -\frac{v_c A_t\sigma_0^2}{2}\left(\frac{1}{E_0} + \frac{1}{E_1}\right) \tag{3.7}$$

where the strain value in the crack section ($x = 0$) is made well-designed through $\varepsilon(0) = \frac{1}{2}\left[\varepsilon\left(0^-\right) + \varepsilon\left(0^+\right)\right] = \frac{1}{2}\varepsilon\left(0^+\right)$ [114,115]. Note that the two terms in Eq. (3.7)

represent the elastic energy per unit time stored in the system and the viscoelastic dissipated energy per unit time, respectively

$$U_{el} = \frac{v_c A_t \sigma_0^2}{2E_0} \qquad D_s = \frac{v_c A_t \sigma_0^2}{2E_1} \tag{3.8}$$

Finally, substituting Eqs. (3.2,3.3 ,3.7) into Eq. (3.1) we have

$$\frac{\sigma_0^2}{2E_\infty} + \sigma_0(1 - \cos\theta) = \frac{\gamma}{d} \tag{3.9}$$

which represents the peeling equilibrium condition. Interestingly regardless of the peeling velocity v_c, Eq. (3.9) is identical to the Kendall equation (1.9) with the elastic modulus given by the high frequency viscoelastic modulus E_∞. Notice that Eq. (3.9) can be rephrased as

$$\frac{1}{2}\left(\frac{\sigma_0}{E_0}\right)^2 + \kappa\frac{\sigma_0}{E_0}(1 - cos\theta) = \kappa\frac{\gamma}{E_0 d} \tag{3.10}$$

where we have defined the viscoelastic factor as $\kappa = E_\infty/E_0$. For $\theta = 0$, we get

$$\sigma_K = \sqrt{\frac{2\kappa E_0 \gamma}{d}} = \sqrt{\frac{2E_\infty \gamma}{d}} \tag{3.11}$$

so that, in this case, the peeling is much more tough than in the (low frequency) elastic case as the effective work of adhesion is κ-times larger than γ.

In order to explain the appearance of the high-frequency viscoelastic modulus E_∞ in Eq. (3.9) we note that, because of the stuck condition assumption (no relative sliding at the tape-substrate interface), the tape is subjected to an abrupt stretching in the peeling section (see Fig. 4.1). For this reason, regardless of the peeling velocity v_c, the material response close to the peeling front is governed by the high-frequency viscoelastic response, which makes the tape locally behave as a perfectly elastic material with elastic modulus E_∞.

Notably, in real conditions, the abrupt change of the tape stress during peeling would be smoothed, as it must occur on a finite length scale across the peeling section. Since the size of this transition zone can be estimated of order unity of the tape thickness d (see also Refs [23, 34]), the tape excitation frequency during peeling is $\omega \approx v_c/d$, so that at very low peeling velocities, i.e. when $v_c \ll d/\tau$, the tape response would be governed by the low-frequency viscoelastic modulus E_0. However, since we usually expect that $v_c \gg d/\tau$, this would not qualitatively affect the physical picture of the peeling behavior provided so far.

3.2 Frictional sliding interface

The discussion provided in the previous section is based on the assumption that the tape firmly sticks to the rigid substrate, and the tangential component of the peeling force P, remotely acting on the tape tip, is locally balanced by a

point reaction force acting in the peeling section. However, as discussed before, it has been shown that a certain amount of relative sliding occurs in real interfaces [32,34,79,80], so that the tangential component of the peeling force P is balanced by the frictional shear stresses arising at the interface between the tape and the rigid substrate. In this case, we consider an interfacial model where slip occurs if the interfacial shear stress is higher than a critical value f, which maintains uniform within the whole sliding length a, [91]. The force equilibrium of a plate element inside tape strip requires

$$\frac{d\sigma}{dx} = -\frac{f}{d} \tag{3.12}$$

which, integrated according with the force at the edge of the sliding region $\sigma(-a) = 0$ and $\sigma(0) = \sigma_0 cos\theta$, gives the extension of the sliding length. Thus, during the peeling process, a portion of the adhering tape of length

$$a = \frac{\sigma_0 cos\theta}{f} d = \frac{P cos\theta}{wf} \tag{3.13}$$

is gradually stretched and slides against the substrate. Such a physical scenario is shown in Fig. 4.2.

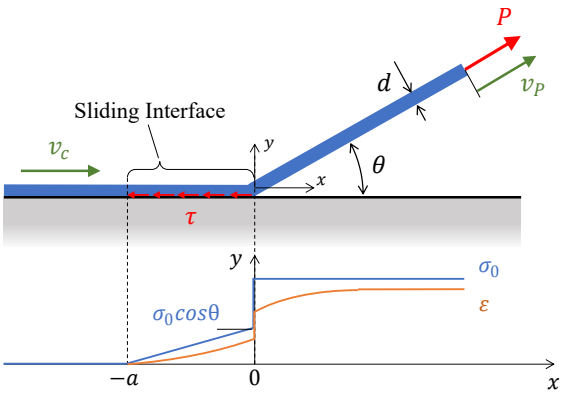

Figure 3.2: The scheme of the peeling process of a thin viscoelastic layer from a rigid substrate in the presence of relative sliding at the interface. Notably, f is the frictional shear stress. In the lower part, qualitative diagrams of the tape stress σ (red) and deformation ε (blue) are shown.

Being $v_s(x) = v_c \varepsilon(x)$ the sliding velocity distribution at the interface, derived from the tape mass conservation, the work per unit time done by interfacial frictional stresses is calculated as

$$W_T = -\int_{-a}^{0} v_s(x) f w dx = -f w v_c \int_{-a}^{0} \varepsilon(x) dx \tag{3.14}$$

Of course, both the stress and deformation distributions along the tape are modified due to the presence of the tangential tractions f. Indeed, from Eq.

(3.12), we have

$$\begin{aligned} \sigma(x) &= \frac{f}{d}(x+a); \qquad -a \le x < 0 \\ \sigma(x) &= \sigma_0; \qquad x > 0 \end{aligned} \tag{3.15}$$

where $\sigma_0 cos\theta = fa/d$. Similarly, from Eq. (4.4), recalling, Eq. (3.5), one obtains

$$\begin{aligned} \varepsilon(x) &= \frac{f}{E_0 d}(a+x) - \frac{f\lambda}{E_1 d}\left[1 - \exp\left(-\frac{x+a}{\lambda}\right)\right]; \qquad -a \le x < 0 \\ \varepsilon(x) &= \frac{\sigma_0}{E_0} - \frac{\sigma_0}{E_1}\left\{1 - \frac{fa}{\sigma_0 d} + \frac{f\lambda}{\sigma_0 d}\left[1 - \exp\left(-\frac{a}{\lambda}\right)\right]\right\}\exp(-x/\lambda); \qquad x > 0 \end{aligned} \tag{3.16}$$

Recalling Eq. (3.14) and using Eqs. (4.4, 3.16) we have

$$W_T = -A_t v_c \frac{\sigma_0^2}{2E_0}\cos^2\theta\left\{1 - 2\frac{\kappa-1}{\kappa}\frac{\lambda}{a}\left[1 - \frac{\lambda}{a} + \frac{\lambda}{a}\exp\left(-\frac{a}{\lambda}\right)\right]\right\} \tag{3.17}$$

where $a/\lambda =$ In Eq. (3.17), we note that for $a/\lambda \to \infty$ we get $W_T \to -\frac{1}{2}A_t v_c(\sigma_0^2/E_0)\cos^2\theta$, which involves the low frequency modulus E_0; whereas, for $a/\lambda \to 0$ we get $W_T \to -\frac{1}{2}A_t v_c(\sigma_0^2/E_\infty)\cos^2\theta$, which involves the high frequency modulus E_∞. Moreover, $W_T(a/\lambda \to \infty) = \kappa\, W_T(a/\lambda \to 0)$. It is worth to note that, just for $\theta \to \pi/2$, W_T vanishes. In particular, even in the limit of $f \to 0$ a non-negligible dissipative contribution associated with interfacial shear stresses lasts. This can be explained considering that, in such case, the force equilibrium Eq.(3.13) requires $a \to \infty$, so that, even if infinitesimal, frictional losses occur over an infinite area, resulting in a finite value of W_T. Of course, for real system where tapes have a finite length, the maximum a value is limited by the adhering tape portion length a_c. It results that, as long as $a \le a_c$ the system is in equilibrium as the tangential component of the external force ($Pcos\theta$) is entirely balanced by frictional stresses; as soon as $a > a_c$, $Pcos\theta$ is no longer balanced and the tape entirely slides in the pulling direction. On the other side, in the limit of $f \to \infty$ the sliding region is reduced to an infinitesimal length where all the frictional losses are concentrated, and $W_T \neq 0$. In light of this, the stuck case can not be recovered as a limit case of the sliding model.

This time, the work per unit time done by tape internal stresses is

$$W_I = -wdv_c\int_{-\infty}^{+\infty}\sigma(x)\,\varepsilon'(x)\,dx = \tag{3.18}$$

$$-wdv_c\frac{\sigma_0^2}{2E_0}\cos^2\theta\left\{\frac{2}{\kappa} - 1 - 2\frac{\kappa-1}{\kappa}\frac{\lambda}{a}\left[\frac{\lambda}{a} - \left(1 + \frac{\lambda}{a}\right)e^{-\frac{a}{\lambda}}\right]\right\} \tag{3.19}$$

$$+wdv_c\frac{\sigma_0^2}{2E_0}\left\{2\frac{\kappa-1}{\kappa}\left[\frac{3}{2} - cos\theta\left(1 - \frac{\lambda}{a}\left(1 - e^{-\frac{a}{\lambda}}\right)\right)\right]\right\} \tag{3.20}$$

Finally, recalling that, in this case, Eq. (3.1) modifies in

$$W_E + W_I + W_S + W_T = 0 \tag{3.21}$$

and using Eqs. (3.2,3.3,3.17 ,3.18) into Eq. (3.21), the final peeling equilibrium equation for a viscoelastic tape in the presence of frictional sliding at the interface is given by

$$\frac{\sigma_0^2}{2E_0}\left\{\left(1-\cos^2\theta\right)-\frac{\kappa-1}{\kappa}\left(1-\cos\theta\right)\left(1+2\cos\theta\left[\frac{\lambda}{a}\left(1-\exp\left(-\frac{a}{\lambda}\right)\right)-\frac{1}{2}\right]\right)\right\} \tag{3.22}$$
$$+\sigma_0(1-\cos\theta)-\frac{\gamma}{d}=0$$

3.3 Models comparison

3.3.1 Dimensionless analysis and limit solutions

In this section will be discussed the main outcomes of the peeling models proposed above. In order to simplify the interpretation of the results, we introduce the following dimensionless parameters: $\tilde{P} = P/(A_t E_0) = \sigma_0/E_0$, $\tilde{f} = f/E_0$, $\tilde{\gamma} = \gamma/(E_0 d)$ and $\tilde{v}_c = v_c\tau/d$. In our calculation, reasonable value of dimensionless parameters are assumed accordingly with experimental value taken from the literature [17, 79–81]. Note that $a/\lambda = \tilde{P}\cos\theta/\left(\tilde{v}_c\tilde{f}\right)$. Therefore, Eq. (3.22) becomes

$$\frac{\tilde{P}^2}{2}\left\{\left(1-\cos^2\theta\right)-\frac{\kappa-1}{\kappa}\left(1-\cos\theta\right)\left(1+2\cos\theta\left[\frac{\tilde{v}_c\tilde{f}}{\tilde{P}\cos\theta}\left(1-\exp\left(-\frac{\tilde{P}\cos\theta}{\tilde{v}_c\tilde{f}}\right)\right)-\frac{1}{2}\right]\right)\right\} \tag{3.23}$$
$$+\tilde{P}(1-\cos\theta)=\tilde{\gamma}$$

In the limiting cases of $\tilde{v}_c \gg 1$ and $\tilde{f} \gg 1$, Eq. (3.22) gives

$$\frac{1}{2}\frac{\sigma_0^2}{E_\infty}\left(1-\cos^2\theta\right)+\sigma_0(1-\cos\theta)=\frac{\gamma}{d} \tag{3.24}$$

which clearly differs from Eq. (3.9), showing that the energy dissipation due to frictional sliding at the interface is proportional to $\frac{1}{2}\left(\sigma_0^2/E_\infty\right)\cos^2\theta$, which leads to much tougher peeling behavior at small peeling angle, as the peeling stress σ_0 diverges as σ_K/θ. This result has been already observed in Refs. [85, 91] for purely elastic tapes (E is replaced by E_∞), and it can be interpreted as the emergence of an infinitely tough peeling behavior. Incidentally, it is worth noticing that ultratough peeling has been also predicted to occur when the tape is elastic and the substrate viscoelastic [23, 67].

Similarly, in the limiting case of $\tilde{v}_c\tilde{f} \ll 1$ with $\tilde{v}_c \gg 1$ (i.e. $v_c \gg d/\tau$), Eq. (3.22) becomes

$$\frac{1}{2}\frac{\sigma_0^2}{E_0}\left(1-\cos^2\theta\right) - \frac{\left[\sigma_0\left(1-\cos\theta\right)\right]^2}{2E_1} + \sigma_0(1-\cos\theta) = \frac{\gamma}{d}, \tag{3.25}$$

where the tape response in the adhered portion subjected to frictional shear stresses is governed by the low frequency viscoelastic modulus E_0. However, in Eq. (3.25), the additional term

$$D_{\mathrm{f}} = \frac{\sigma_0^2\left(1-\cos\theta\right)^2}{2E_1} = \left(1-\cos\theta\right)^2 D_{\mathrm{s}} \tag{3.26}$$

represents the viscoelastic energy dissipation per unit time, triggered by the stress step change $\sigma = \sigma_0 - \sigma_0\cos\theta$, which still occurs at the peeling front. Indeed, this time Eq. (3.8) is still valid provided that σ_0 is replaced by σ. Notice that, as already discussed before, for $\tilde{v}_c \ll 1$ (i.e. $v_c \ll d/\tau$) the term D_{f} must also vanish, as even in the peeling section the tape behaves elastically with modulus E_0. Therefore, for $\tilde{f} \ll 1$ and $\tilde{v}_c \ll 1$ (i.e. $v_c \ll d/\tau$), Eq. (3.22) becomes

$$\frac{1}{2}\frac{\sigma_0^2}{E_0}\left(1-\cos^2\theta\right) + \sigma_0(1-\cos\theta) = \frac{\gamma}{d} \tag{3.27}$$

which holds true for purely elastic tapes (with elastic modulus $E = E_0$) in the presence of interfacial frictional sliding (see Refs [81, 85, 91]).

3.3.2 Effect of viscoelastic parameter and adhesion energy

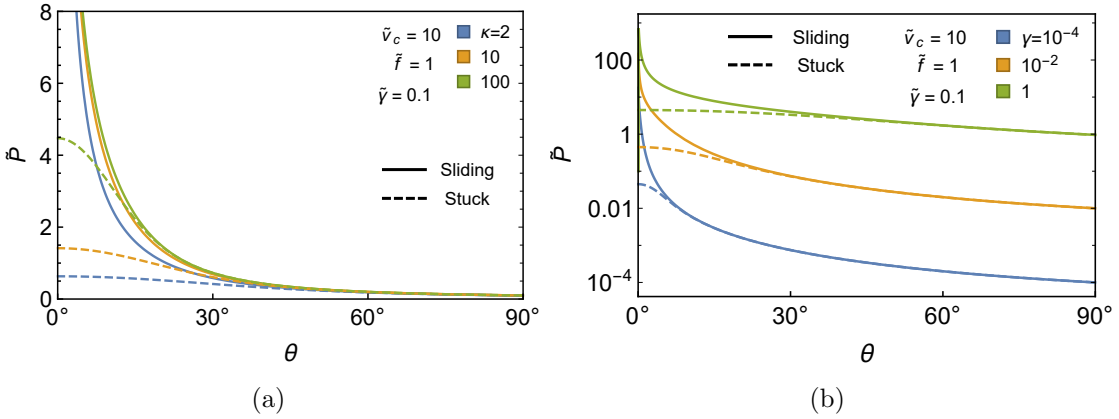

Figure 3.3: The dimensionless peeling force $\tilde{P}$ as a function of the peeling angle θ, for different values of (a) the viscoelasticity parameter $\kappa = E_\infty/E_0$; and (b) the dimensionless energy of adhesion $\tilde{\gamma}$. The dashed curves refer to the case of stuck interface between the tape and the rigid substrate, whereas continuum curves refer to frictionally sliding interfaces.

Figure 3.6 shows the dimensionless peeling force $\tilde{P}$ as a function of the peeling angle θ, for both stuck and sliding interfaces and different values of the parameter $\kappa = E_\infty/E_0$ (Fig. 3.3a), and of the energy of adhesion γ (Fig. 3.3b).

As already discussed, in the stuck case (dashed lines in Figure 3.6) we recover the well-known elastic Kendall's solution, where the elastic modulus is replaced by the high-frequency viscoelastic modulus E_∞ [see Eq. (3.9)]. Given the values of the low-frequency viscoelastic modulus E_0, the peeling angle θ and work of adhesion γ, the peeling force increases with the parameter $\kappa = E_\infty/E_0$.

On the other hand, in case of frictional sliding at the interface a very different scenario emerges. This time, the peeling process is governed by Eq. (3.22), which, regardless of the κ value, leads to unbounded peeling forces for vanishing peeling angle θ (see continuous lines in Figure 3.6). In this case, the dimensionless peeling force obeys the equation $\tilde{P} = \sqrt{2\tilde{\gamma}}/\theta$ for $\theta \to 0$. Interestingly, such a result is in agreement with several experimental observations on the peeling behavior of insects pads in the presence of relative frictional sliding between the fibrils and the substrate [34, 36, 116]. Figure 3.6 presents the effect of the dimensionless energy of adhesion $\tilde{\gamma}$ on the peeling behavior. As expected, regardless of the specific interface behavior, increasing $\tilde{\gamma}$ leads to an overall tougher peeling behavior, as the necessary stress $\tilde{P}$ to sustain the peeling process increases [54]. Moreover, for relatively high peeling angles, the peeling force predicted by stuck and sliding models is comparable; conversely, as θ decreases, difference in $\tilde{P}$ increases due to the energy dissipation within the sliding region. Interestingly, higher the value of $\tilde{\gamma}$, a more pronunced disparity between the two models becomes evident for higher angles. This is a consequence of the fact that high adhesion energies require greater forces to trigger the detachment, which in turn will increase the length of the shear sliding zone and thus increase the amount of frictional work that must be overcome to peel the tape.

3.3.3 Effect of velocity parameter

Figure 3.4a shows the dimensionless peeling force $\tilde{P}$ as a function of the peeling angle θ. This time, different values of the dimensionless velocity parameter $\tilde{v}_c\tilde{f}$ are considered. In the same figure, we also report purely elastic (with elastic modulus $E = E_0$) solution in presence of frictional sliding Eq. (3.27). We observe that, for relatively small values of the parameter $\tilde{v}_c\tilde{f}$ and moderately large peeling angles θ, the value of $\tilde{P}$, observed in presence of frictional sliding, is lower than the value predicted in the case of stuck interface (see $\tilde{v}_c\tilde{f} = 0.1$ curve in Fig. 3.4a). This is related to the different mechanisms of energy dissipation occurring in each case. In order to clarify this point, we refer also to Fig. 3.4b where are shown the dimensionless dissipative energy terms as a function of the dimensionless velocity parameter for the stuck and sliding case.

For a stuck interface, the only source of energy dissipation arises from the viscoelastic creep occurring in the detached branch of tape (i.e. for $x > 0$), which is independent on θ and $\tilde{v}_c\tilde{f}$ (see $\tilde{D}_S$ curve in Fig. 3.4b). On the contrary, when dealing with interfaces where frictional relative motion occurs between the tape and

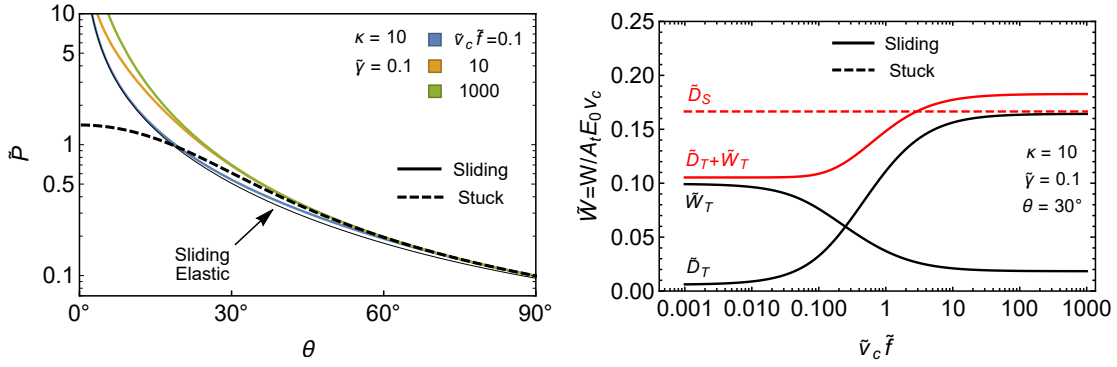

(a) (b)

Figure 3.4: (a) The dimensionless peeling force $\tilde{P}$ as a function of the peeling angle θ, for different values of the dimensionless parameter $\tilde{v}_c\tilde{f}$. The dashed curve refers to the case of stuck interface between the tape and the rigid substrate, whereas continoum curves refer to frictionally sliding interfaces. In the same figure, we also plot for comparison the behavior of an elastic tape in frictional sliding. Results refer to $\tilde{v}_c >> 1$. (b) Dimensionless dissipative terms for the stuck and sliding model as a function of $\tilde{v}_c\tilde{f}$

the substrate, two additional sources of energy dissipation can be identified: (i) the work done by the frictional shear stress at the interface; and (ii) the viscoelastic creep occurring in the portion of the tape stretched by the interfacial frictional shear stresses (i.e. for $-a \leq x < 0$). However, for $\tilde{v}_c\tilde{f} \ll 1$ and for $0 \ll \theta \lesssim \pi/2$, no viscoelastic creep occurs in the adhered sliding portion of the tape (i.e. the tape response is governed by E_0, see Eq. (3.22)) and the term $cos^2\theta \to 0$ has a low influence on the overall energy balance. Therefore, under these conditions, even in the case of frictionally sliding interfaces, the only sources of the energy dissipation is the viscoelastic creep occurring in the detached tape, which can be quantified as D_f through Eq. 3.26) (see $\tilde{D}_f$ and $\tilde{W}_T$ curves in Fig. 3.4b). Since $D_\mathrm{f} = (1-\cos\theta)^2 D_\mathrm{s} < D_\mathrm{s}$ for $\theta < \pi/2$, a lower peeling force is predicted in the frictional sliding case compared to stuck interfaces. Notably, the effect of the energy dissipation term D_f on the overall peeling behavior can be appreciated by comparing the low speed viscoelastic case (blue curve) against the elastic limit (black continuous curve) in Fig. 3.4b. As already discussed in commenting Eq. (3.22)), a physical explanation of this phenomenon can be found by observing that, in the case if frictional sliding interfaces, the step change occurring in the tape stress at the peeling front is lower than in the case of stuck interfaces, as in the former case the in the adhered portion close to the peeling front is pre-stressed by frictional shear stress by a quantity $\sigma_0 cos\theta$. Thus, since for $\tilde{v}_c\tilde{f} < 1$ the tape pre-stress occurs at a very low excitation frequency (i.e. the tape response does not present any creep), the resulting energy dissipation due to the viscoelastic creep (only occurring in the detached strip) is smaller for frictional sliding interfaces compared to the stuck case, in turn leading to smaller peeling forces.

Figure 4.3 shows the dimensionless peeling force $\tilde{P}$ as a function of the dimensionless parameter $\tilde{v}_c\tilde{f}$ for a given value of θ. All the cases refer to $\tilde{v}_c > 1$. As

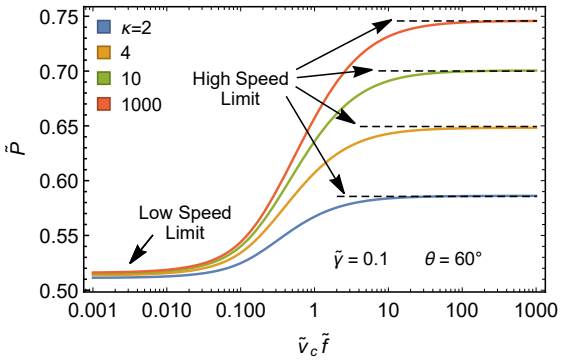

Figure 3.5: The dimensionless peeling force $\tilde{P}$ as a function of the dimensionless parameter $\tilde{v}_c\tilde{f}$, for different values of the parameter $\kappa = E_\infty/E_0$. In the figure, both the high and low speed plateau are highlighted. Results refer to $\tilde{v}_c >> 1$.

expected three different regimes can be observed depending on the value of $\tilde{v}_c\tilde{f}$. For $\tilde{v}_c\tilde{f} \ll 1$ an asymptotic plateau for $\tilde{P}$ is observed as predicted by Eq. (3.25), which depends on the value of κ (the tape response in the peeling section is still governed by E_∞). For $\tilde{v}_c\tilde{f} \gg 1$, the peeling behavior is governed by Eq. (3.24) and depends on the high frequency viscoelastic modulus E_∞. Again, a plateau is observed for $\tilde{P}$, whose value saturates as for $\kappa \to \infty$ as the Rivlin's solution is approached in the case of infinitely stiff tapes. At intermediate values of $\tilde{v}_c\tilde{f}$ the hysteretic viscoelastic behavior of the tape plays a key role so that, in this transition region, the peeling force increases with the peeling rate by following a power law $\tilde{P} \approx \left(\tilde{v}_c\tilde{f}\right)^n$ where the exponent n depends on the parameter κ.

This result is in agreement with experimental evidences where a velocity-dependent peeling force in the form predicted by our model is recovered. See, for instance, Fig. 3.6a where the three regions are well identified from peel-test results of a cellulose nitrate tape debonded from a glass substrate [117]. In particular, the power law as been largely employed for fitting measures of peeling force (e.g. see fig. 3.6b [64]) and it is also extensively recovered by means of empirical formulations where the contribution of energy dissipation is modeled following the Gent and Shultz power law formalism for the energy release rate or the adhesion energy [27, 28, 44, 53, 63, 118]. However, as far as we know, this is the first time that a velocity-dependency of this kind has been obtained as just a result of an analytical model where no *a priori* assumptions have been made on the dissipative contributions and their form.

3.4 Conclusions

In this study, we investigate the peeling behavior of a thin viscoelastic tape peeled away from a rigid substrate. Specifically, we consider two alternative scenarios: one, with the interface between the tape and the rigid substrate under stuck adhesion (i.e. no sliding occurs); the other, assuming relative sliding on a portion of

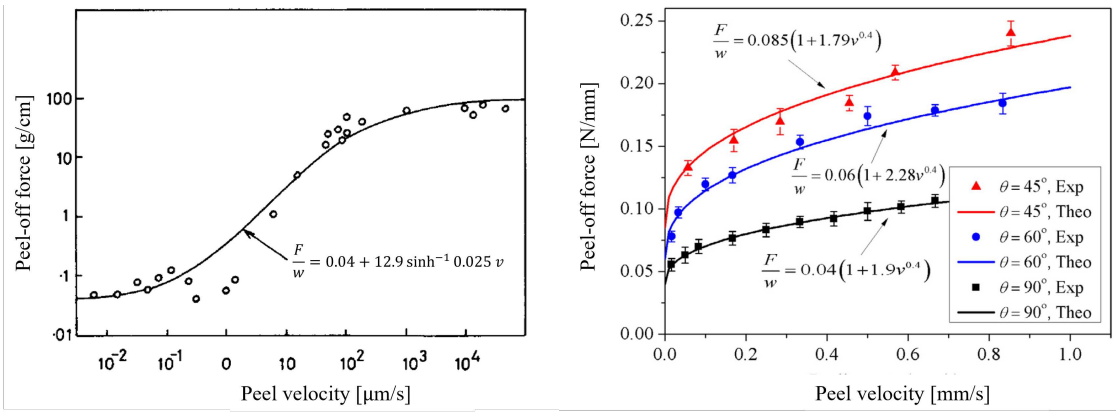

(a) (b)

Figure 3.6: Measures of the peeling force as a function of the peel velocity. (a) Results for the peeling of cellulose nitrate from glass where the two asymptotic limit are well identified. Adapted from [117]. (b) Experiments of a PVC film peeling from a glass substrate. Theoretical predictions are shown for comparison. Adapted from [64].

the interface in the presence of frictional shear stresses.

We found that, in stuck interfaces, the overall viscoelastic peeling behavior is independent of the peeling velocity, provided that the peeling velocity $v_C \gg d/\tau$ (where d is the thickness of the tape and τ is the creep characteristic time of the viscoelastic material), and the peeling force takes the value predicted by Kendall's peeling model with the elastic modulus given by the high-frequency viscoelastic modulus E_∞ of the tape material. Under these conditions, the energy dissipation associated with the viscoelastic creep of the tape is entirely localized in the detached portion of the tape.

In the presence of frictional sliding at the interface additional sources of energy dissipation come into play, which are associated with both the work done by frictional shear stress and the viscoelastic hysteresis occurring in the portion of the adhering tape subjected to frictional shear stresses. In such conditions, the peeling force is predicted to continuously increase as the peeling angle is decreased, leading to unbounded value for a vanishing peeling angle. Also, the viscoelastic hysteretic behavior of the tape strongly affects the dependence of the peeling force on the peeling velocity. Indeed, for any given value of the peeling angle, three regions can be identified: (i) the low velocity region, where a low plateau is reported for the peeling force; (ii) the transition region, where the peeling force increases as a power law of the peeling velocity, and (iii) the high velocity region, where a high plateau of the peeling force occurs.

Our analysis can enhance our comprehension of the role played by specific dissipative phenomena in governing the peeling behavior. It can also help us understand how these phenomena are interrelated and how they affect the overall debonding resistance of the system.

Chapter 4

Nonsteady peeling of viscoleastic tapes

Most of the existing peel tests and theories usually refer to a single peeling configuration, where the pulling force acting on the free edge of the tape and the tape are oriented in the same prescribed direction (i.e. the peeling angle equals the force angle). Moreover, they mostly focus on steady-state propagation condition where the values of peeling quantities remain constant throughout the delamination process. While valuable insights on peeling systems could be inferred from this analysis, there are many practical applications where the delamination process is intrinsically non-stationary and characterized by continuous variation of geometry, load condition and propagation velocity. In order to assess these scenarios, so called shallow-angle configurations are employed. Among others, V-peeling configuration is particularly studied as it allows for a simplified testing condition [16] and as it is widely encountered in natural bonding/debonding processes (see Section 1.2.3). Moreover, although time-dependent viscoelastic behavior intrinsic to biological tissues as well as engineering material used for adhesive tapes and membranes could introduce additional nonsteady contribution to global peeling behavior, the V-peeling of viscoelastic tape is still an unexplored problem.

In this chapter, we present a model for the V-peeling process of viscoelastic tapes backed onto rigid substrates. Since the process under investigation is non-steady, we first set the theoretical energy-based framework and derive the governing equations, then we outline a numerical procedure to predict the process evolution over time in terms of the peeling load, the peeling angle, and the detached tape length. In presenting our model results, we consider three possible test procedures: (i) constant peeling-front velocity, (ii) constant peeling load, (iii) constant pulling velocity), each of which leads to different time-histories allowing to highlight the interplay between complex peeling geometry and tape viscoelasticity.

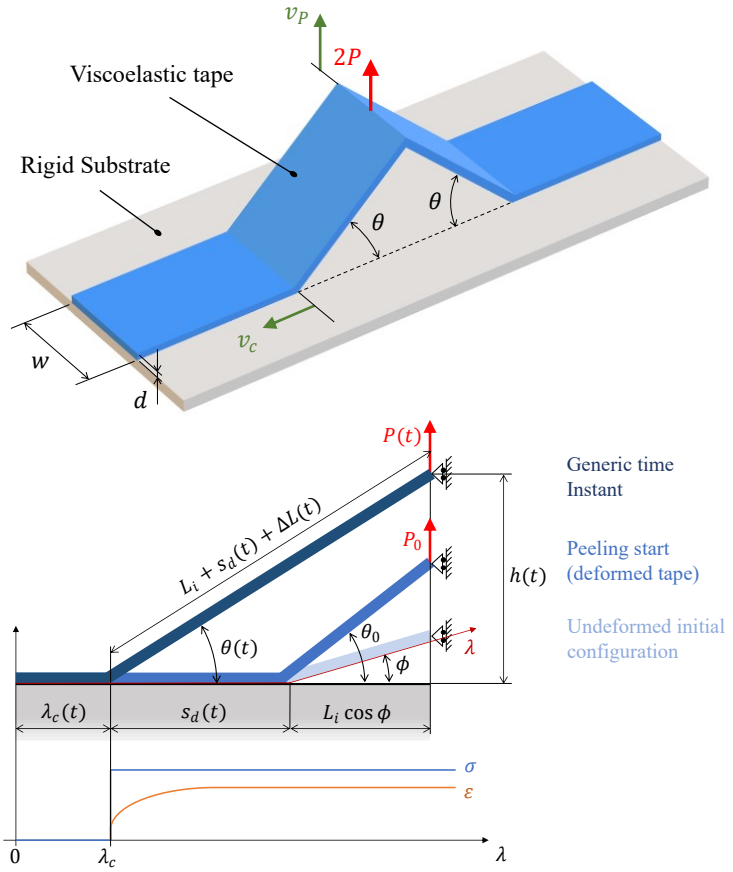

Figure 4.1: Double (V-shaped) peeling scheme of a viscoelastic tape adhering to a rigid substrate, where v_c is the peeling front propagation velocity and v_P is the pulling velocity (i.e., the velocity of the tape tip). The lower part shows the undeformed initial configuration, as well as those associated with the propagation start, and with a generic time instant during the peeling process evolution. Qualitative diagrams of the stress σ (blue) and deformation ε (orange) are also shown for the latter case.

4.1 Analytical formulation

We consider the peeling configuration shown in Fig. 4.1, where a thin viscoelastic tape of thickness d and width w (cross-section $A_t = wd$) adhering to a rigid substrate is pulled away by a vertical force $2P$. As illustrated in the figure, film detachment occurs via propagation of two opposite peeling fronts, resulting in an overall V-shaped peeling geometry. However, the particular symmetry of such configuration allows limiting the study to half of the system. Moreover, since θ depends on the tape deformation and instantaneous system configuration, V-peeling propagation is, in general, a transient process.

Referring to Fig. 4.1, we define a fixed reference frame λ along the undeformed tape (at rest), so that $\lambda_c(t)$ and $v_c(t) = -d\lambda_c/dt$ are the peeling front coordinate and velocity, respectively, at a generic time t. As the peeling front moves to the left, a tape portion of length $s_d(t) = \int_0^t v_c(t)\,dt$ is debonded, so that the instantaneous

peeling angle $\theta(t)$ is given by

$$\cos\theta = \frac{s_d + L_i \cos\phi}{L_i + s_d + \Delta L} \tag{4.1}$$

where L_i is the undeformed length of the initially non-adhering tape, and $\Delta L(t) = \int_{\lambda_c}^{\lambda_c+s_d+L_i} \varepsilon(\lambda,t)d\lambda$ is the elongation of the overall detached tape, with $\varepsilon(\lambda,t)$ being the extensional deformation field in the tape. Notably, as shown in Fig. 4.1, $\theta = \phi$ at rest (i.e., for $P = 0$).

The instantaneous energy balance governing the peeling evolution is

$$W_E + W_I + W_S = 0 \tag{4.2}$$

where $W_E(t)$ is the work per unit time done by the peeling force $P(t)$, $W_I(t)$ is the work per unite time done by the internal stress field, and $W_S(t)$ is the rate of the surface adhesion energy. In Eq. (4.2), minor energy contributions ascribable to acoustic emissions and heat transfer are neglected, as well as dynamic and inertial effects which might lead to stick-slip unstable delamination [29,31,80,119,120]. Moreover, we assume a fully stuck adhesion between the tape and the rigid substrate in the adhering region, thus no friction energy dissipation occurs due to relative sliding, as instead considered in Ch. 3.

The term $W_I(t)$ is associated with both the rate of elastic energy stored in the detached tape and the viscoelastic energy loss occurring during the tape relaxation. Large deformations can be reasonably expected for soft polymeric tapes; however, both numerical [121] and experimental [34] studies have clearly shown that real systems exhibiting strains as large as beyond 60% can still be both qualitatively and quantitatively described in linear theory approximation, especially at relatively large peeling angles [24]. Moreover, we assume purely extensional stress $\sigma(\lambda,t)$ and deformation $\varepsilon(\lambda,t)$ fields, as experiments have shown that bending effects vanish for very thin tapes [122] (i.e., the tape bending stiffness depends on d^3). Therefore, we have

$$W_I = -A_t \int_{\lambda_c}^{\lambda_c+L_i+s_d} \sigma(\lambda,t)\frac{\partial\varepsilon}{\partial t}(\lambda,t)d\lambda \tag{4.3}$$

with $\varepsilon(\lambda,t) = \sigma(\lambda,t) = 0$ for $\lambda < \lambda_c$ (adhering tape) and $\sigma(\lambda,t) = \sigma(t) = P/(A_t \sin\theta)$ for $\lambda > \lambda_c$ (detached tape). In the peeling section (i.e., for $\lambda = \lambda_c$), a step change of the stress occurs (see Chapter 3), so that

$$\sigma(\lambda,t) = \sigma(t)H[\lambda - \lambda_c(t)] \tag{4.4}$$

where $\mathcal{H}$ is the Heaviside step function. In the framework of linear viscoelasticity, the deformation field within the tape is given by

$$\varepsilon(\lambda,t) = \int_{-\infty}^{t} \mathcal{J}(t-t')\frac{\partial\sigma}{\partial t'}(\lambda,t')dt' \tag{4.5}$$

where $\mathcal{J}$ is the viscoelastic creep function. For a single characteristic creep time τ, is given by (see Chapter 2)

$$\mathcal{J}(t) = \frac{1}{E_0} - \frac{e^{-t/\tau}}{E_1} \tag{4.6}$$

where $E_1^{-1} = E_0^{-1} - E_\infty^{-1}$, with E_0 and E_∞ being the low and high frequency viscoelastic moduli, respectively.

The term $W_E(t)$ in Eq. (4.2) is given by

$$W_E = P\, v_P = \sigma A_t v_P \sin\theta \tag{4.7}$$

where

$$v_P = \frac{dh}{dt} = v_c \tan\theta + \frac{s_d + L_i \cos\phi}{\cos^2\theta}\dot{\theta} \tag{4.8}$$

is the pulling velocity (see Fig. 4.1).

Finally, in Eq. (4.2), $W_S(t)$ represents the energy per unit time associated with the rupture of interfacial bonds between the tape and the rigid substrate; being γ the work of adhesion[1], we have

$$W_S = -v_c w \gamma \tag{4.9}$$

As mentioned so far, the the work of adhesion γ might, in general, depend on the peeling velocity, as the results of non-conservative interfacial or bulk-processes ascribable to viscous/viscoelastic mechanisms (see Chapter 1). Here, we precisely model the tape viscoelastic creep, thus the latter effect is intrinsically accounted for. However, as pointed out by Marin & Derail [28] with ad hoc tests on inextensible tapes, velocity-dependent power loss is also localized in the thin adhesive layer between the tape and the substrate. Thus, in order to account for the pure interfacial loss contribution, we model a velocity-dependent work of adhesion as

$$\gamma = \gamma_0 \left[1 + \left(\frac{v_c}{v_\gamma}\right)^n\right] \tag{4.10}$$

where γ_0 is the adhesion energy for $v_c \ll v_\gamma$, with v_γ being a reference peeling velocity, and n being a constant which depends on the properties of the adhesive (typically in a range of $0.3 \div 0.7$) [28, 44, 64].

At any given time t, Eqs. (4.1,4.2) allow to calculate the critical condition for peeling propagation.

We remark that, in the present formulation, we assumed that the stress and deformation fields present a step-change in the peeling section (i.e., for $\lambda = \lambda_c$). However, the real deformation process of the initially undeformed adhering tape is continuous and occurs in a small adhering region very close to the peeling front, with the stress gradually increasing from 0 to σ value. Physical arguments suggest that the size of such a region is of the same order of magnitude as the tape thickness d [23, 66]. The excitation frequency in this portion of material as $\omega \approx v_c/d$; therefore, depending on the value of v_c, three viscoelastic regimes can be identified. At extremely low peel-rate (i.e., for $v_c \ll d/\tau$ and $\omega \ll 1/\tau$), the response of the tape very close to the peeling section is elastic and governed by the low-frequency modulus E_0. In this case, no relaxation (i.e., no viscoelastic dissipation) occurs

[1] Unlike as Chapeter 1, here we use γ symbol to indicate the work of adhesion instead of Γ.

in the tape and the peeling behavior is governed by the well-known Kendall's theory [17], so that

$$\frac{\sigma^2}{2E_0} + \sigma\,(1 - \cos\theta) - \frac{\gamma}{d} = 0 \tag{4.11}$$

For $v_c \approx d/\tau$ (i.e., $\omega \approx 1/\tau$), the tape response close to the peeling section is governed by viscoelasticity. In this case, energy dissipation occurs even at the small-scale, which strictly depends on the specific trend of stress increase from 0 to σ value; therefore, *ad Hoc* solid mechanics formulations are required to properly account for this effect.

The formulation and the results presented in this study focus on the third case, i.e. for $v_c \gg d/\tau$ and $\omega \gg 1/\tau$. Under this condition, the tape close to the peeling front behaves elastically, with high frequency elastic modulus E_∞. The whole viscoelastic loss occurs in the detached tape relatively far from the peeling front. We observe that, since in common practice adhesive tapes can be as thin as $10 \div 100$ μm with principal viscoelastic relaxation times ranging in the order of seconds, the threshold velocity is in the range of $d/\tau \approx 10^{-5} \div 10^{-4}$ m/s, thus being significantly lower than the usual peeling front velocity in real-life applications.

4.2 Numerical implementation

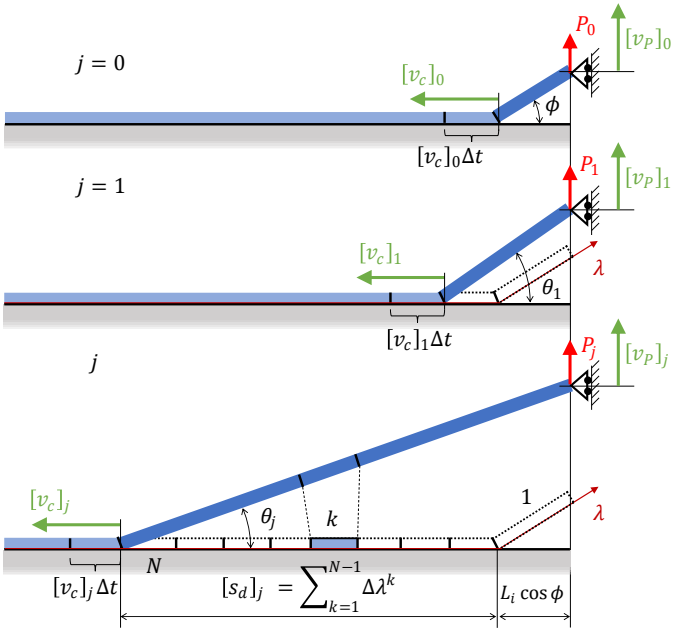

Figure 4.2: A schematic of the tape mesh: at the generic j-th time instant, the tape mesh is updated by including a freshly detached element of undeformed length $\Delta\lambda = [v_c]_j\,\Delta t$.

The process evolution can be calculated by numerical integration of Eqs. (4.2, 4.1). However, dealing with a viscoelastic tape, the governing equations depend on the entire time-history of the process and the solution of Eqs. (4.2, 4.1) must

be iteratively sought by successively updating the system configurations as the propagation advances.

The numerical method is based on uniform time discretization, with time step $\Delta t \ll \tau$, and non-uniform tape mesh. In the following discussion, the notation η_j^k represents the discrete value of the generic quantity η at the j-th time instant in the k-th tape element. Only the non-adhering tape is discretized and the mesh is updated at each time step so that, at the generic time $t_j = j\Delta t$, an element of (undeformed) length $\Delta\lambda = [v_c]_j \, \Delta t$ is added to take into account for the additional detached tape resulting from the peeling front advancement. The resulting non-uniform "incremental" mesh has two primary advantages: (i) the total number of elements does not need to be fixed a priori; (ii) only the non-adhering tape is discretized and the computational cost is reduced. More in details, referring to Fig. (4.2), $N_j = j+1$ is the total number of tape elements at the j-th time instant, with the first element $\Delta\lambda^1$ being the initial non-adhering tape (i.e., $\Delta\lambda^1 = L_i$) and the N-th element $\Delta\lambda^{N_j}$ being last detached element ($\Delta\lambda^{N_j} = \Delta t \, [v_c]_{j-1}$). Therefore, the detached tape projection s_j is given by

$$s_j = L_i \cos\phi + [s_d]_j = L_i \cos\phi + \sum_{k=2}^{N_j} \Delta\lambda^k \tag{4.12}$$

The discrete form of Eqs. (4.9,4.7) is

$$[W_S]_j = -\,[v_c\gamma]_j \, w \tag{4.13}$$

$$[W_E]_j = A_t \;\; [v_P\sigma]_j \sin\theta_j \tag{4.14}$$

where, from Eq. (4.8),

$$[v_P]_j = [v_c]_j \, \tan\theta_j + \frac{s_j}{\cos^2\theta_j} \frac{\theta_j - \theta_{j-1}}{\Delta t} \tag{4.15}$$

Integrating by parts, Eq. (4.5) is rewritten as

$$\varepsilon(\lambda, t) = \frac{\sigma(\lambda, t)}{E_\infty} + \int_{-\infty}^{t} \dot{\mathcal{J}}(t - t')\sigma(\lambda, t')dt' \tag{4.16}$$

where we used $\mathcal{J}(0) = E_\infty^{-1}$, and $\sigma(\lambda, -\infty) = 0$; the discrete form of Eq. (4.16) gives the elongation of the generic k-th element of the non-adhering tape at the j-th time instant as

$$\varepsilon_j^k = \frac{\sigma_j^k}{E_\infty} + \Delta t \sum_{h=0}^{j} \dot{\mathcal{J}}_{j-h}\sigma_h \tag{4.17}$$

with $\sigma_j^k = \sigma_j = P_j / \left(A_t \sin\theta_j\right)$ for all the tape elements.

To calculate W_I, we observe that the term $\partial\varepsilon/\partial t(\lambda, t)$ diverges at the peeling front (i.e., for $\lambda \to \lambda_c(t)$), as we assume a step-change in the tape stress σ. In this case, the discretized form of Eq. (4.3) can be conveniently rewritten as

$$\frac{[W_I]_j}{A_t} = -\sigma_j \dot{\varepsilon}_j^N \Delta\lambda^N - \sigma_j \sum_{k=1}^{N-1} \dot{\varepsilon}_j^k \Delta\lambda^k \tag{4.18}$$

where, as already done in Ch. 3, according to [114, 115], since $v_c \gg d/\tau$, the first right-hand side term can be calculated as

$$\sigma_j \dot{\varepsilon}_j^N \Delta\lambda^N = \frac{[\sigma^2 v_c]_j}{2E_\infty} \tag{4.19}$$

Combining Eqs. (4.18, 4.19), the discretized form of Eq. (4.3) is

$$\frac{[W_I]_j}{A_t} = -\frac{[v_c \sigma^2]_j}{2E_\infty} - \sigma_j \sum_{k=1}^{N-1} \left[\frac{\varepsilon_j - \varepsilon_{j-1}}{\Delta t} \Delta\lambda \right]^k \tag{4.20}$$

Finally, using Eqs. (4.13,4.14,4.20) in Eq. (4.2) gives the discrete form for the instantaneous energy balance equation

$$[W_E]_j + [W_I]_j + [W_S]_j = 0 \tag{4.21}$$

and, from Eq. (4.1) we have

$$\frac{s_j}{\cos\theta_j} = \sum_{k=1}^{N} \left(1 + \varepsilon_j^k\right) \Delta\lambda^k \tag{4.22}$$

where $\left(1 + \varepsilon_j^k\right) \Delta\lambda^k$ is the deformed length of the generic k-th element at the j-th time instant.

In what follows, we consider three different scenarios, each associated to a specific controlled parameter: (i) constant peeling front velocity v_c; (ii) constant peeling force P; and (iii) constant pulling speed v_P. An iterative algorithm, based on the Newton-Rapshon method, is employed at each time instant to solve Eqs. (4.21,4.22) for the unknown peeling quantities.

4.2.1 Steady-state long-term propagation limit

Although the V-peeling process is non-stationary, a steady-state regime is asymptotically approached in the long term limit [19], when the non-adhering tape is sufficiently long to ensure complete viscoelastic relaxation. In this case, the peeling angle θ_S is constant, and the energy balance equation recovers the viscoelastic single peeling form Eq. (3.9) as

$$\frac{\sigma_S^2}{2E_\infty} + \sigma_S \left(1 - \cos\theta_S\right) - \frac{\gamma}{d} = 0 \tag{4.23}$$

where $\sigma_S = P_S / \left(A_t \sin\theta_S\right)$ and θ_S are the long-term steady-state asymptotic limits, and γ depends on the peeling front velocity v_c through Eq. (4.10). Moreover, since $s_d \gg L_i$ and $\varepsilon(\lambda, t) \approx \varepsilon_S = \sigma_S / E_0$, Eq. (4.1) can be rewritten as

$$\frac{1 - \cos\theta_S}{\cos\theta_S} = \frac{\sigma_S}{E_0} \tag{4.24}$$

Furthermore, since $\dot{\theta}_S \approx 0$, Eq. (4.8) modifies as

$$v_P = v_c \tan\theta_S \tag{4.25}$$

Notably, under force-controlled conditions (i.e., given $P = P_S$), Eqs. (4.23,4.24,4.10) allow to calculate the peeling front velocity v_c and, through Eq. (4.25), the pulling velocity v_P. On the contrary, under velocity controlled conditions (i.e., given v_c or v_P), the value of P_S can be calculated by Eqs. (4.23,4.24,4.10).

4.3 Simulation results and discussion

In this section, we discuss the peeling behavior of a viscoelastic tape arranged in double (V-)peeling configuration. To simplify the interpretation of the results, we refer to the following dimensionless quantities $\tilde{t} = t/\tau$, $\tilde{\gamma} = \gamma/E_0 d$, $\tilde{v}_c = v_c\tau/d$, $\tilde{v}_P = v_P\tau/d$, $\tilde{P} = P/dwE_0 = \sigma \sin\theta/E_0$. In our calculations, we assume a tape thickness $d \approx 100$ μm, $E_0 = 10$ MPa and a relaxation time $\tau = 1$ s. The adhesion of real tapes has been measured by specific peeling tests in Ref. [28]: referring to Eq. (4.10), they found $v_\gamma \approx 0.1$ mm/s, $\gamma_0 \approx 20$ J/m^2 and $n = 0.5$. Therefore, in our calculations, set $\tilde{\gamma}_0 = \gamma_0/E_0 d = 0.02$ and $\tilde{v}_\gamma = v_\gamma\tau/d = 10$. It is worth to note that experimental tests reported in Ref. [28] are based on tapes with aluminum backing, so that the effect of tape viscoelasticity can be neglected, and the dependence of γ on the peeling front velocity v_c must be only ascribed to local non-conservative phenomena.

4.3.1 Constant peeling front velocity

We firstly consider the peeling process occurring at constant peeling front velocity v_c. Although this case may result far from usual test conditions and practical application (as both the corresponding peeling force P and pulling velocity v_P are time-varying), important insights on the overall system behavior can be inferred from this analysis. Moreover, in long-term steady-state limit, from Eq. (4.25) we have that constant v_c entails constant v_P.

In order to initialize the iterative calculation scheme described in Sec. 4.2, we need to calculate the peeling force $P_0 = A_t\ \sigma_0\ \sin\theta_0$ able to trigger the peeling propagation at constant peeling front velocity v_c. Specifically, with reference to Fig. 4.1, we assume that P_0 is instantaneously applied at time $t = 0$ to the tape, thus leading to a step change of the non-adhering tape deformation from $\varepsilon = 0$ (i.e., undeformed) and tape angle ϕ at time $t \to 0^-$ to $\varepsilon = \sigma_0/E_\infty$ and tape angle θ_0 at time $t \to 0^+$ (i.e., when the peeling front propagation starts). Moreover, since the viscoelastic threshold velocity $d/\tau \approx 10^{-4}$ m/s is of poor interested for practical applications, we consider $v_c \gg d/\tau$. Under these conditions, since at $t = 0$ no viscoelastic loss occurs, the critical values of σ_0 and θ_0 for peeling initiation are given by the Kendall's equation for a tape with elastic modulus $E = E_\infty$

$$\frac{\sigma_0^2}{2E_\infty} + \sigma_0\,(1 - \cos\theta_0) - \frac{\gamma}{d} = 0 \tag{4.26}$$

and, from Eq. (4.1) with $s_d = 0$

$$\frac{\cos\phi - \cos\theta_0}{\cos\theta_0} = \frac{\sigma_0}{E_\infty} \tag{4.27}$$

Once the viscoelastic relaxation starts (i.e., for $t > 0$), the peeling process evolution can be calculated by means of the procedure outlined in Sec. 4.2.

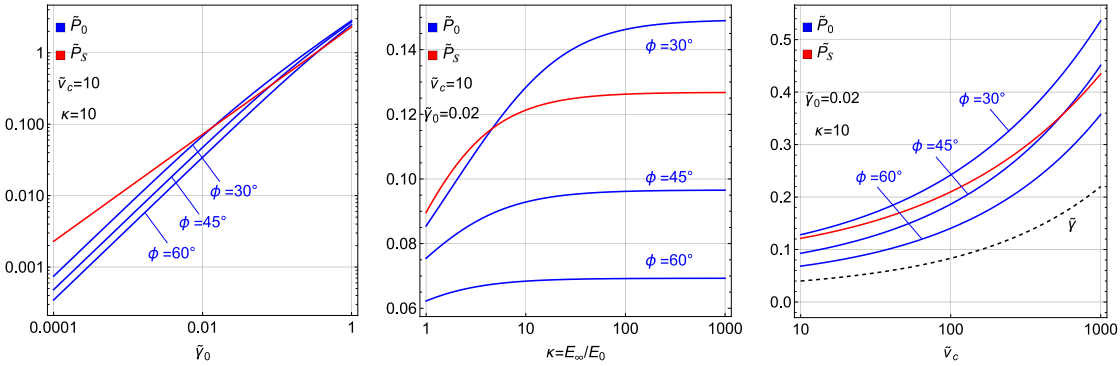

Figure 4.3: The initial $\tilde{P}_0$ and long-term $\tilde{P}_S$ dimensionless peeling force as functions of the dimensionless adhesion energy $\tilde{\gamma}_0$ (a), the viscoelastic parameter $\kappa = E_\infty/E_0$ (b) and the dimensionless peeling front velocity $\tilde{v}_c$ (c). In figure (c), the rate-dependent dimensionless adhesion energy $\tilde{\gamma}$ is also shown for comparison (dashed line). Notably, $\kappa = 1$ corresponds to the elastic tape limit.

Comparing the initial and long-term limiting behavior allows to highlight some peculiar features of viscoelastic V-peeling. This is done in Figures 4.3, showing the dimensionless values of the peeling force in the initial $\tilde{P}_0$ and long-term $\tilde{P}_S$ limits as functions of (a) the dimensionless adhesion energy $\tilde{\gamma}_0$, (b) the viscoelastic parameter $\kappa = E_\infty/E_0$, and (c) the dimensionless peeling front velocity $\tilde{v}_c$. First, we observe that $\tilde{P}_0$ can be either larger or smaller than $\tilde{P}_S$, depending on the specific combination of the peeling parameters $\tilde{\gamma}_0$, κ, and $\tilde{v}_c$. This is strictly related to tape viscoelasticity and relaxation, as in the case of elastic V-peeling we always have the toughest peeling condition associated with the long-term limit and the smallest peeling angle (see also $\kappa = 1$ in Fig. 4.3b). As expected, Figs. 4.3 also show that reducing ϕ tougher peeling initiation is achieved, regardless of the other parameters. Similarly, from Figs. 4.3a,4.3c it follows that peeling toughness increases with $\tilde{\gamma}_0$ and $\tilde{v}_c$, as in both cases the adhesion energy γ in Eqs. (4.9,4.23,4.26) increases. In Fig. 4.3b, we observe that the stiffer the tape, the larger the peeling force is, in agreement with theoretical predictions [17] and experimental results [123]; however, at very large values of κ, the tape response asymptotically approach the rigid limit, and the peeling behavior resembles the Rivlin prediction [15].

Figures 4.4 show the time-history of peeling process evolution in terms of (a) the normalized peeling force $\tilde{P}/\tilde{P}_0$ and (b) the peeling angle θ, for different dimensionless peeling front velocity $\tilde{v}_c$ (notably, $\tilde{P}_0$ also depends on $\tilde{v}_c$, as shown in

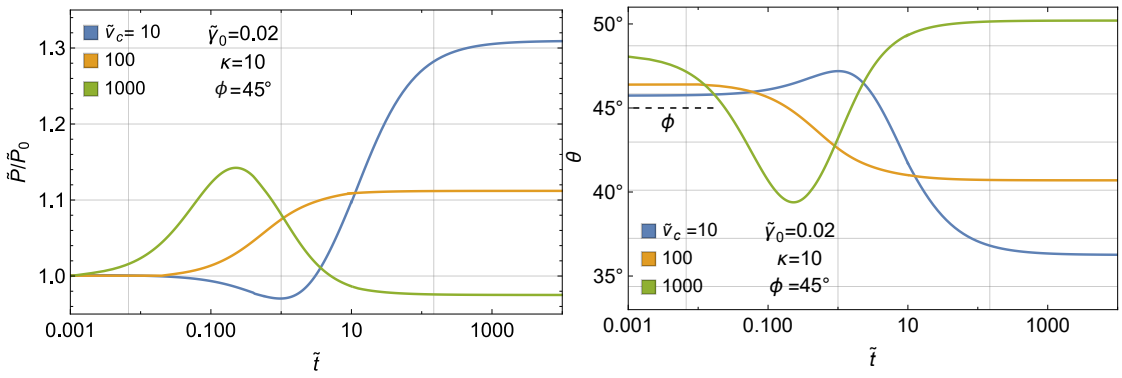

(a) (b)

Figure 4.4: The time-history of the normalized dimensionless peeling force $\tilde{P}/\tilde{P}_0$ (a) and the peeling angle θ (b) for different values of the peeling front velocity $\tilde{v}_c$.

Fig. 4.3c). First, in Fig. 4.4b, we observe that the peeling angle θ_0 associated with peeling initiation increases with $\tilde{v}_c$. This can be easily explained by observing that, from Eq. (4.27), θ_0 increases with $\tilde{P}_0$ and, from Fig. 4.3c, $\tilde{P}_0$ increases with $\tilde{v}_c$. Surprisingly, the main qualitative feature shown in Figures 4.4 is that in viscoelastic V-peeling both θ and $\tilde{P}/\tilde{P}_0$ may present non-monotonic trends, in contrast with the elastic case. Focusing first on the θ time-history, this is mostly ascribable to the interplay of two phenomena (see also Eq. (4.1)): first, the peeling front advancement, causing a linear increase of s_d; second, the tape relaxation, affecting the term ΔL. For $\tilde{t} \ll 1$ (i.e., $t \ll \tau$), a rough estimation of $\dot{\theta}$ can be derived from Eq. (4.1) as $\dot{\theta} \propto d\left(\Delta L\right)/dt - \beta v_c$, with $\beta = \beta\left(\theta_i\right) \approx 1$ for $\theta_i \gg 0$; therefore, depending on the value of v_c, the peeling angle θ at $\tilde{t} \ll 1$ can either show a decreasing (at high velocity, i.e. $\tilde{v}_c \approx 1000$) or increasing (at low velocity, i.e. $\tilde{v}_c \approx 10$) trend, as indeed shown in Fig. 4.4b. However, the long-term limit θ_S is approached for $\tilde{t} \gg 1$, thus $\theta\left(t\right)$ may experience a non-monotonic trend, depending on the specific value of θ_S. As expected [17,19], the values of $\tilde{P}/\tilde{P}_0$ and θ are correlated, as high values of θ lead to low values of $\tilde{P}/\tilde{P}_0$ and vice-versa; therefore, non-monotonic trends of θ also entail non-monotonic trends of $\tilde{P}/\tilde{P}_0$.

4.3.2 Constant peeling force

In this section, we investigate the viscoelastic peeling V-peeling behavior under a constant peeling force P, which means that the peeling front can either start and indefinitely propagate, start and stop at some point, or not start at all, depending on the value of P, given a generic initial undeformed configuration (i.e., the value of ϕ). However, since in this case the peeling front velocity $v_c\left(t\right)$ is not know a priori and depends on the process evolution through Eqs. (4.1,4.2), we need to outline three qualitative physical scenarios. First, for $v_c \gg v_\gamma \gg d/\tau$, the limiting force for peeling initiations and long-term steady-state propagation are P_0 and P_S, respectively, as predicted by Eqs. (4.26,4.27) and Eqs. (4.23,4.24).

Second, for $d/\tau \ll v_c \ll v_\gamma$, the peeling behavior is still governed by the tape high-frequency elastic modulus E_∞, but the critical values P_1 of the peeling force for peeling initiations and P_2 for long-term steady-state propagation are given by Eqs. (4.26,4.27) and Eqs. (4.23,4.24), respectively, with $\gamma \approx \gamma_0$. Finally, for $v_c \ll d/\tau \ll v_\gamma$, the tape deformation once moving across the peeling section is a slow continuous process rather then a step-change, and the tape response is governed by the low-frequency elastic modulus E_0. In this latter case, we the limiting values P_3 and P_4 for peeling initiation and long-term steady-state propagation are given, respectively, by Eqs. (4.26,4.27) and Eqs. (4.23,4.24), with $\gamma \approx \gamma_0$ and E_∞ replaced by E_0.

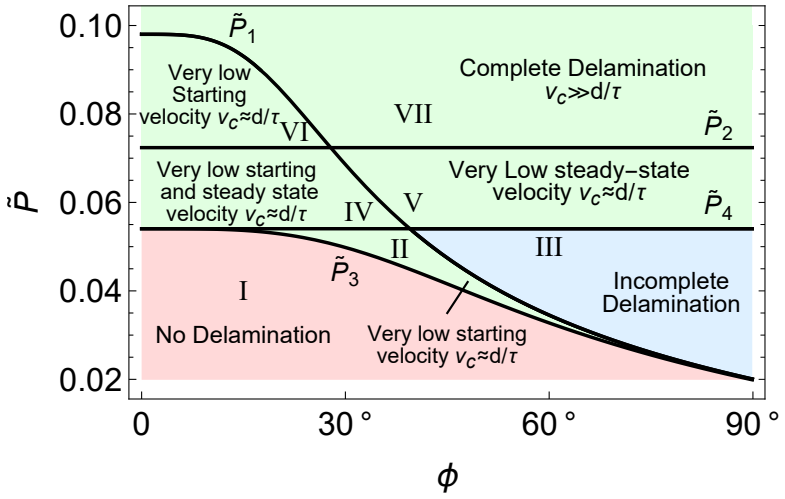

Figure 4.5: The state map of the possible peeling behavior as a function of the dimensionless applied peeling force $\tilde{P}$ and undeformed tape angle ϕ. The definitions of the dimensionless limiting loads $\tilde{P}_1$, $\tilde{P}_2$, $\tilde{P}_3$, $\tilde{P}_4$ are given in the body text.

The map in Fig. 4.5 shows the possible qualitative peeling behaviors, depending of the dimensionless applied peeling force $\tilde{P}$ and undeformed tape angle ϕ. Notably, the dimensionless critical loads for peeling initiation $\tilde{P}_1$ and $\tilde{P}_3$ depend on the undeformed tape angle ϕ; whereas, the long-term steady-state dimensionless limits $\tilde{P}_2$ and $\tilde{P}_4$ do not. Three main regions can be identified: the peeling does not propagate (region I); the peeling propagation starts and then stops after some time (II-III); the peeling propagates indefinitely (VI and VII, together with IV and V where the long-term velocity is very low though). The model presented in this study is able to rigorously predict the peeling behavior in regions I and VII; however, qualitative insight can also be inferred for regions III and V (as a velocity of about $d/\tau \approx 10^{-5}$ m/s in the long-term limits qualitatively correspond to the full stop case III), and region VI, as v_c quickly increases after the low velocity peeling initiation. Regions II and IV cannot be accounted for in the present framework as the specific viscoelastic behavior close to the peeling front does really matter throughout the whole process evolution; however, since $d/\tau \approx 10^{-4}$ m/s is a very low value, these are of little interest. In most cases, real systems belong to the

first scenario, with $v_c \gg v_\gamma \gg d/\tau$.

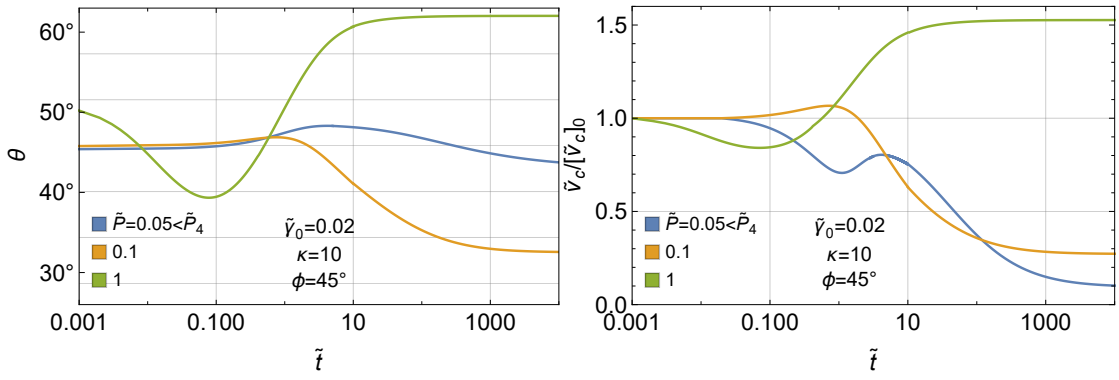

(a) (b)

Figure 4.6: The time-history of the peeling angle θ (a) and the normalized peeling front velocity $\tilde{v}_c/\left[\tilde{v}_c\right]_0$ (b), for different values of the dimensionless peeling force $\tilde{P}$.

Fig. 4.6 shows the time-history of the peeling angle θ and normalized peeling front velocity $\tilde{v}_c/\left[\tilde{v}_c\right]_0$ for different values of $\tilde{P}$ (in regions V and VII), where $\left[\tilde{v}_c\right]_0$ is the peeling front velocity when propagation initiates. Firstly, in Fig. 4.6a we note that increasing $\tilde{P}$ leads to increasing values of θ_0, as the detached tape experiences higher elongation when the process initiates. As discussed so far, non-monotonic trends occur due to interplay between tape relaxation and peeling front advancement, with key features localized at $\tilde{t} \approx 1$. Specifically, in Fig. 4.6b, we observe that complete delamination up to the long-term steady-state condition occurs when load conditions fall in region VII (i.e., $\tilde{P} > \tilde{P}_1$ as for orange and green curves), whereas v_c reduces to very low values eventually for conditions corresponding to region V (i.e., blue curve). Interestingly, both the magnification of peel strength in steady peeling over a certain range of velocity and the slowing or stopping of the debonding process have been already experimentally observed by Kendall [35] and have been interpreted as the effect of viscoelastic energy loss in the bulk of the peeling film.

The energy loss in the bulk of the peeling film introduces two additional effects: a magnification of the peel strength in steady peeling over a certain velocity range, and a slowing down or stopping of peeling as transient relaxation occurs shortly after the application of the peel force.

4.3.3 Constant pulling velocity

Lastly, we consider the case of a tape pulled at a constant velocity v_P (see Fig. 4.1), so that the deformation $\varepsilon(t)$ and stress $\sigma(t)$ in the non-adhering tape monotonically increase before peeling front propagation initiates. In this case, rather than at $t = 0$, peeling front propagation occurs at a certain time t^* when $\sigma\left(t^*\right) = \sigma_{cr}\left(t^*\right)$,

with σ_{cr} depending on the energy balance

$$\frac{\sigma_{cr}^2}{2E_\infty} + \sigma_{cr}[1 - \cos\theta] = \frac{\gamma_0}{d} \tag{4.28}$$

Until peeling front propagation occurs, the peeling angle can be calculated as

$$\tan\theta = \frac{L_i \sin\phi + v_P t}{L_i \cos\phi} \tag{4.29}$$

where $v_P t$ is the tape edge displacement at a generic time t (see also Fig. 4.7a). Since $L_i + \Delta L = L_i \cos\phi / \cos\theta$ is the deformed tape length, the tape uniform deformation before peeling propagation is

$$\varepsilon(t) = \frac{L_i + \Delta L}{L_i} - 1 = \frac{\cos\phi}{\cos\theta} - 1 \tag{4.30}$$

Finally we can calculate the stress in the detached tape as (see Chapter 2),

$$\sigma(t) = \int_{-\infty}^{t} \mathcal{R}(t - t')\dot{\varepsilon}(t')dt' \tag{4.31}$$

where $\mathcal{R}$ is the stress-relaxation function given by (see Chapter 2)

$$\mathcal{R}(t) = E_0 + (E_\infty - E_0)e^{-t/\tau_r} \tag{4.32}$$

with $\tau_r = \tau/(1 + \Delta) = \tau/\kappa$ being the relaxation time, where $\Delta = E_\infty/E_0 - 1$ is the relaxation strength.

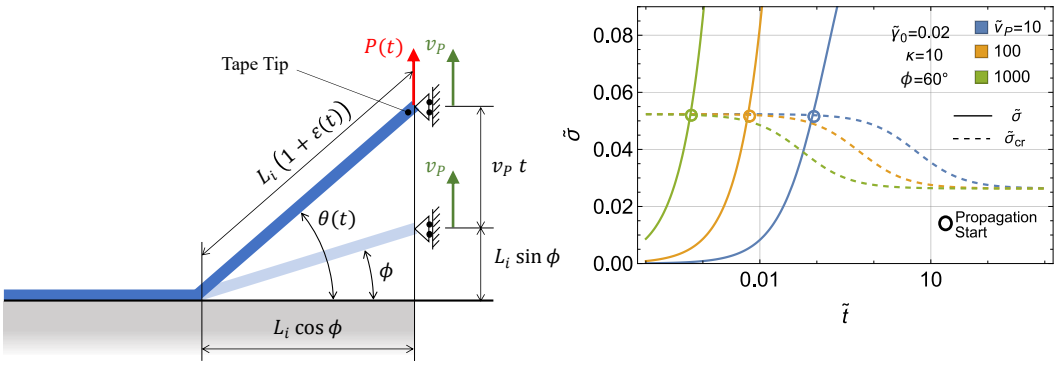

(a) (b)

Figure 4.7: (a) A schematic of the system in the initial undeformed condition, and at a generic time $t < t^*$ before the peeling propagation starts. (b) The dimensionless tensile stress $\tilde{\sigma}$ in the tape and the critical tensile stress $\tilde{\sigma}_{cr}$ to start the peeling propagation (dashed curves) as functions of the dimensionless time $\tilde{t}$ for different dimensionless tape tip velocity $\tilde{v}_P$. The circles indicate the instant of propagation start.

The peeling propagation start is then obtained by simultaneously solving Eqs. (4.28-4.31). Once the peeling front propagation starts, the numerical algorithm

described in Section 4.2 can be used to calculate time evolution of the peeling process with t^* corresponding to $j = 0$. Regarding the value of the peeling front velocity $v_c(t^*)$ associated with the start of the peeling propagation, it cannot be exactly determined in the framework of the present model. However, after the very early stages of peeling, we rapidly have $v_c > d/\tau$, as we assumed $v_P/\tan\theta_S = [v_c]_S \gg d/\tau$. Therefore, we set $\tilde{v}_c(t^*) \approx 1$.

In Figure 4.7b we show the time-history of $\tilde{\sigma}(t)$ and $\tilde{\sigma}_{cr}(t)$, for different dimensionless pulling velocity $\tilde{v}_P$. Increasing $\tilde{v}_P$ leads to higher stress in the viscoelastic tape, thus peeling propagation starts sooner.

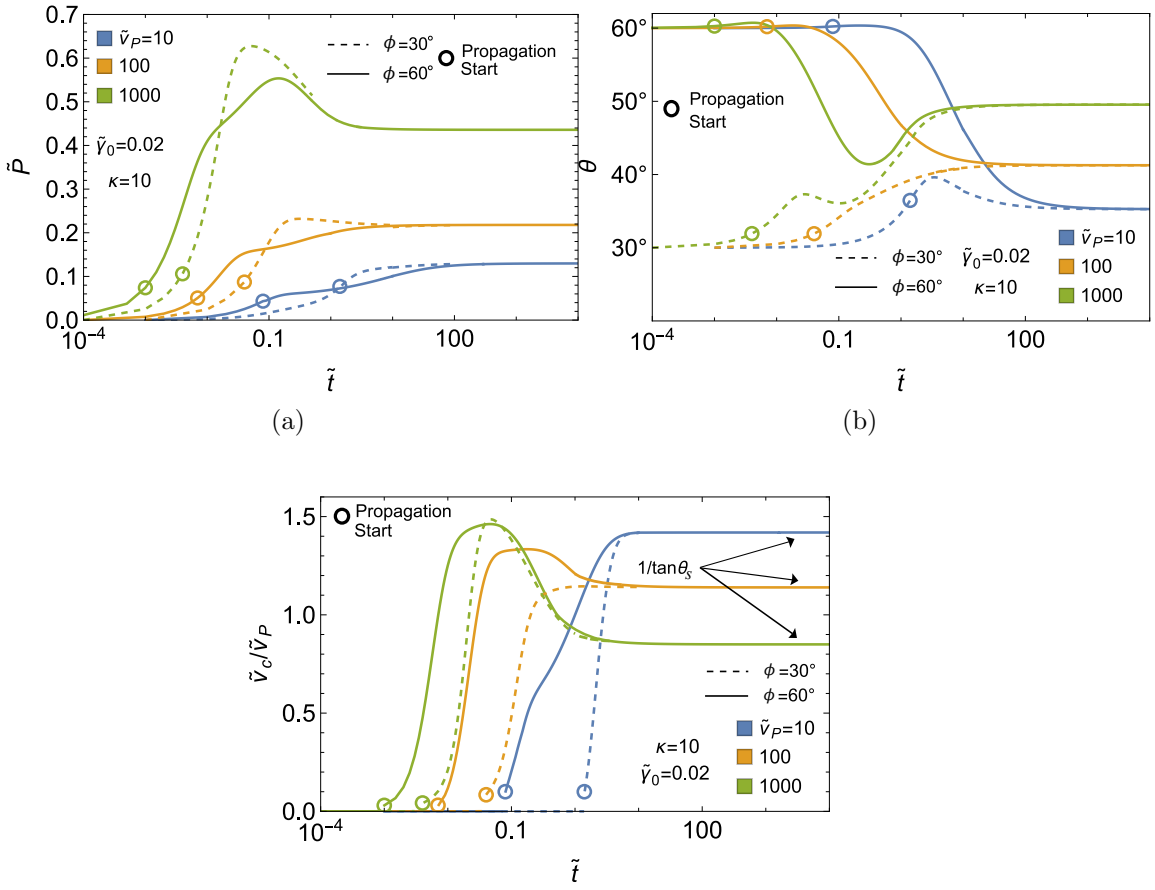

Figure 4.8: The time-history of the dimensionless peeling force $\tilde{P}$ (a), the peeling angle θ (b) and the dimensionless normalized peeling front velocity $\tilde{v}_c/\tilde{v}_P$ for different values of the dimensionless pulling velocity $\tilde{v}_p$. Two different initial configurations are considered: $\theta_i = 60$ (solid lines), and 30 (dashed lines). The circles indicate the instant of propagation start.

In Figs. 5.2, we show the time-history of $\tilde{P}$, θ and $\tilde{v}_c/\tilde{v}_P$, for different values of the dimensionless pulling velocity $\tilde{v}_P$ and initial angles θ_i. Of course, reducing θ_i leads to a longer time interval before propagation occurs, as Eq. (4.28) predicts

tougher peeling behavior. Steady-state propagation regime is always recovered in the long-term limit, with $[v_c]_S / \tilde{v}_P = 1/\tan\theta_S$ (see Eq. (4.25). However, depending on the pulling velocity $\tilde{v}_P$, the peeling force $\tilde{P}$ may present a maximum just after the peeling propagation start (see Fig. 4.8a). Such a peculiar feature may relate to the superior adhesive performance of natural systems, such as spider webs [76] and mussels byssus [77], under the action of high-speed (impact) loading conditions. In the latter case, for instance, Cohen at Al. [124] have shown that the single byssus highly stretchable response can be ascribed to the heterogeneity of the filament structure (a system of nonlinear swollen springs); here, we suggest that the interplay between byssus rheology and the multiple V-shaped threads geometry may also contribute to the observed tougher adhesive response under dynamic loads [77].

4.4 Conclusions

In this study, we investigate the peeling behavior of a viscoelastic thin tape arranged in double V-shaped peeling configuration. Specifically, the velocity-dependent condition for peeling front propagation is found in terms of energy balance between the work per unit time done by the internal stress in the tape, the external forces acting on the system, and the surface adhesion forces. An *ad hoc* numerical procedure is derived to model the time-evolution of the peeling process, taking into account for the time-varying viscoelastic relaxation of the detached tape. We consider three possible scenarios, associated with different controlled parameters: the peeling front velocity, the peeling force, and the pulling velocity at the tape tip.

In the long-term limit, the peeling propagation asymptotically approaches a steady-state elastic-like behavior, regardless of the specific controlled parameter. However, the initial transient peeling behavior is strongly affected by the tape viscoelasticity and undeformed geometry, and presents non-monotonic time evolution of the peeling toughness (and angle). Under given peeling force conditions, the peeling propagation can either start and indefinitely continue, start and successively stop, or even not start at all, depending on the peeling force and undeformed geometry. More surprisingly, when the pulling velocity at the tape tip is assigned, as in the case of impact loads, the time required to trigger the peeling propagation may significantly vary due to viscoelastic relaxation, and the time evolution of the resulting peeling force may present a maximum. This mechanism might be qualitatively related to the high-speed superior adhesive performance observed in several natural systems.

Chapter 5

Frictional contact on rubber: an experimental study

Ever since, friction is one of the most addressed fundamental problems in the field of tribology. It is an ubiquitous phenomenon in every contact pair, influenced by the mechanical properties of materials, the geometrical characteristics of surfaces (e.g. roughness) and the physico-chemical behavior of interfaces (e.g. adhesive/repulsive interactions). Because of the complex interconnection between these factors, despite the long-stand effort, friction is still a partially unresolved problem. In particular, due to its significance in various engineering applications, such as sealing [125], wear resistance [126], lubrication [127], and electrical/thermal insulation [128], the relationship between adhesion, friction and contact area in soft contact context stands as a primary focus of research.

Starting from common observations of changing in the contact shape in frictional contact problems, different mechanisms have been proposed to unravel the origin of this evidence. Theoretical and experimental investigations on elastomeric sphere/plane contacts have indicated that the presence of tangential displacement at the interface leads to a reduction of the contact area, which may also lose its circular symmetry (see Fig. 5.1a). This phenomenon, known as friction-induced adhesion weakening, has been interpreted using fracture mechanics adhesion models [129–133] for full stick conditions (i.e. in the presence of uniform tangential displacement at the contact interface). However, conflicting evidences could arise when considering the gross slip contact regime, where the contact area is observed to remain unchanged, or even to increase at moderate slip velocities [134, 135].

Although soft materials can easily achieve high levels of strain outside linear elastic range during frictional contact conditions [136], most of the theoretical models are grounded in linear elastic frameworks. In this case, for perfect incompressible material (Poisson modulus $\nu = 0.5$), a fully uncoupling between normal and in-plane response is expected [137]. However, when dealing with nearly-incompressible materials ($\nu \lesssim 0.5$), a certain degree of coupling emerges even within the linear elastic range. This coupling becomes increasingly pronounced and anisotropic at higher deformations when the nonlinear material response is triggered [138]. In this context, contact area reduction and shape asymmetry re-

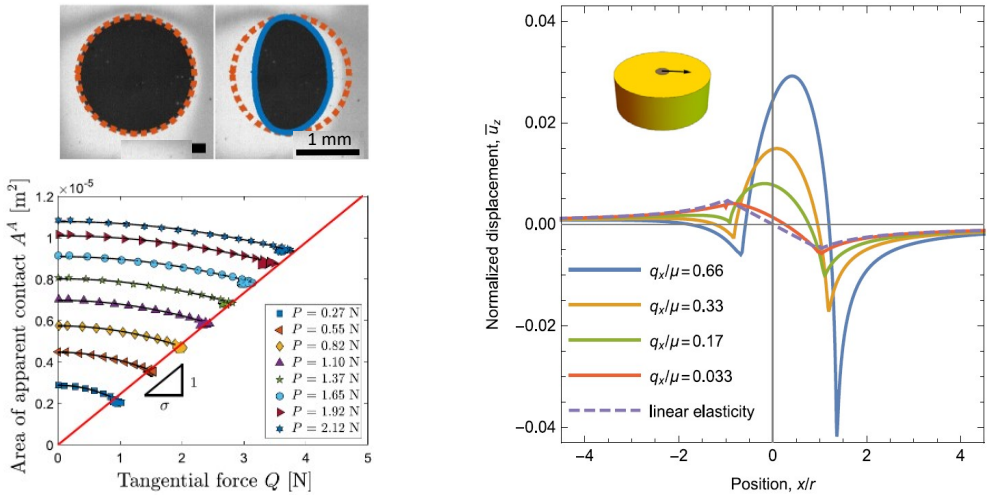

(a) (b)

Figure 5.1: (a) Effect of interfacial tangential force on the contact area for a smooth PDMS/glass sphere/plane contact in full stick condition. Adapted from [132]. (b) Normalized vertical surface displacement for a nearly incompressible ($\nu = 0.49$) half-space loaded by a homogeneous tangential traction over a circular area for neo-Hookean model (solid lines) and linear elastic case (dashed line). Adapted from [138].

sult from a sinking and a lifting of the soft material's surface at the trailing and leading edges of contact, respectively (see Fig. 5.1b).

In this regard, recent investigations have shown that coupling could affect significantly gap topography and sliding behavior of rough contact pairs resulting in a friction reduction [125]. Moreover, confinement could induce a coupling effect which, on contrary lead to friction to increase [125, 139].

In the following, we present an experimental study aimed at investigating the contribution of material non linearities and the mechanical confinement on the size and shape of the contact area under steady-state sliding. Friction experiments within smooth contact interfaces between silicon substrates and glass spheres have been carried out on an homemade set-up which allows for the measure of in-plane displacements and tangential force.

5.1 Experimental details

5.1.1 The substrate

Material

The experiments were carried out using two different formulations of Polydimethylsiloxane (PDMS) rubber to vary the extent of material non-linearities effect:

- Sylgard 184 mixed in a 10:1 ratio with its hardener; this system will be denoted as S184.

- A mixture of Sylgard 184 and Sylgard 527 in a 1:1 ratio; this system will be denoted as S184:S527.

These rubbers were characterized in the range of linear elastic behavior in term of the elastic modulus E and the adhesion energy γ through static indentation test carried on bulk specimens with a glass lens of radius $R = 9.33$ mm. The applied normal load F_N is increased step by step from 50 N to 1.5 N. At each load step, the contact radius is measured after an equilibrium time. Data are analysed using the following linearized form of the JKR theory [140]:

$$\frac{a^{3/2}}{R} = \frac{1}{K}\frac{F_N}{a^{3/2}} + \sqrt{\frac{6\pi w}{K}} \tag{5.1}$$

with $K = 16/9E$. In fig. 5.2a, $a^{3/2}/R$ is plotted as a function of $F_N/a^{3/2}$. A linear fit to Eqn 5.1 provides E =1.93 MPa and w =33 mJ m^{-2} for S184 and E =0.94 MPa and w =26 mJ m^{-2} for S184:S527, in agreement with measures present in literature [141]
Additionally, the deviation from linear elastic behavior for higher deformations is shown in Fig. 5.2b for S187 rubber specifically . Experimental strain-stress curve (red line) under uniaxial tension is fitted with two different hyperelastic models: neo-hookean (blue line Eq. 5.2) and Yeoh (blue line Eq. 5.3) laws, respectively

$$\sigma = 2C_{10}\left(\lambda - \frac{1}{\lambda^2}\right) \tag{5.2}$$

$$\sigma = 2\left(\lambda - \frac{1}{\lambda^2}\right)\left[C_{10} + 2C_{20}(I_1 - 3) + 3C_{30}(I_1 - 3)^2\right] \tag{5.3}$$

where $I_1 = \lambda^2 + \frac{2}{\lambda}$ is the first invariant and C_{10}, C_{20} and C_{30} are material constants.

Specimen preparation

Bulk specimens are prepared with S187 and S184:S527 with dimensions 6-3,5-1,5 cm, approximately, to ensures that semi infinite contact conditions are achieved during sliding experiments (i.e. the ratio of the substrate thickness to the contact radius is greater than ten [15]). In addition, a S184 PDMS layer 2 mm in thickness was also manufactured to investigate the effects of mechanical confinement. This layer was glued on a glass substrate to prevent any interface slippage at the interface with during sliding experiments.

In order to monitor contact induced surface displacements, a square network of small cylindrical holes (20 µm in diameter and a mesh size of 400 µm) is produced on the PDMS. Under transmitted light observation conditions, such holes act as markers which are easily detectable using image processing. In order to elaborate these marked PDMS surfaces, a resin template with a network of cylindrical pillars is firstly realized on a silicon wafer by means of soft microlithography. The PDMS mixture is then directly molded in resin template and cured in an oven for 48 hours at 70 °C (see. Fig. 5.3).

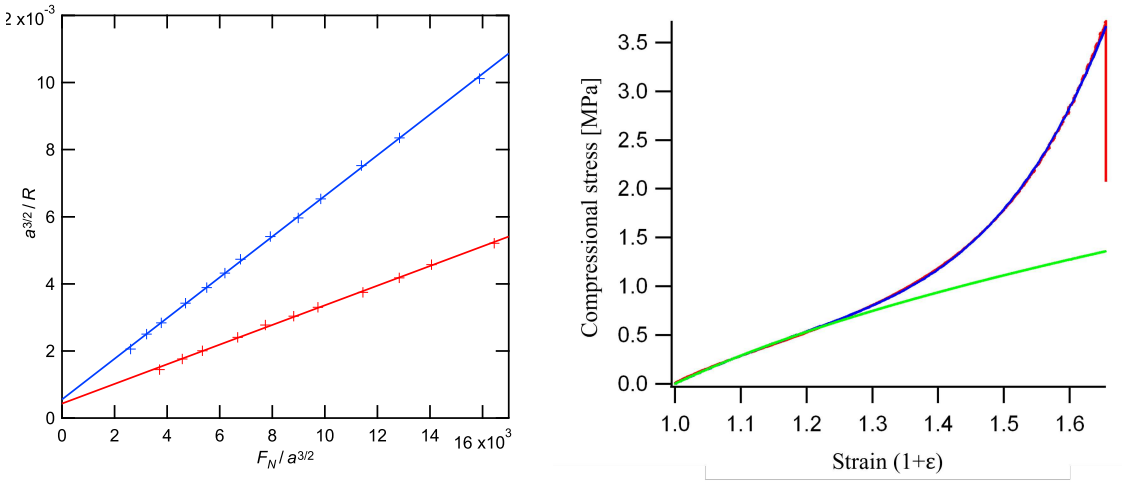

(a) (b)

Figure 5.2: (a)Static indentation response in linear elastic range of S184 (red) and S184:S527 (blue). Solid line: linear fit to Eq (5.1) with E =1.93 MPa and w =33 mJ m^{-2} for S184 and E =0.94 MPa and w =26 mJ m^{-2} for S184:S527. (b) Nominal stress as a function of stretch ratio for S184 (red line) under uniaxial tension. The green line corresponds to a fit to neo-hokean model with C_{10} = 0.526 MPa. The blue line is a fit to Yeoh model with C_{10} = 0.526 MPa, C_{20} = -0.036 MPa, C_{30} = 0.357 MPa.

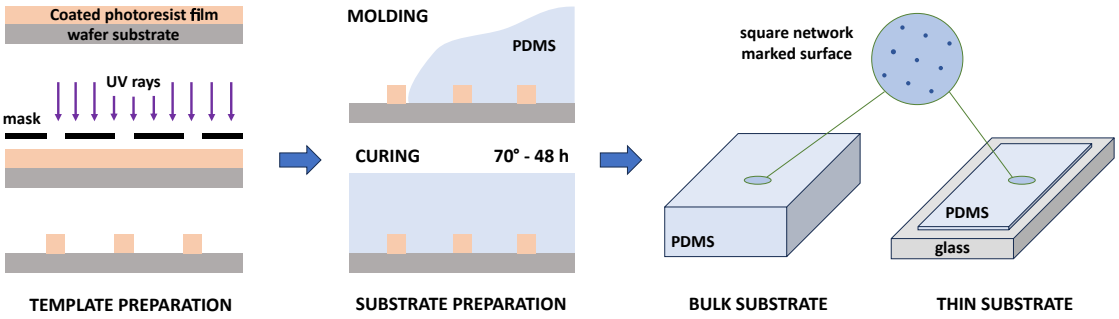

Figure 5.3: Preparation of bulk and thin PDMS specimens. Liquid PDMS is molded on a resin template obtained by microlithography technique. This process produces a square network of small cylindrical holes.

5.1.2 The set-up

The sliding experiments have been conducted between a spherical glass lens (static element) and the PDMS substrate (sliding element) displaced by means of a linear translation stage. Two different home-made set-up have been used differing in how the normal load is applied

- a device where the normal load (between 0.8 and 2.1 N) is applied by means of a dead weight arrangement
- a device where a constant normal load (between 0.1 and 10 N) is achieved

by means of an actuator which continuously adjust the vertical position of the probe during the experiments.

In both cases, contact visualization is performed through the transparent PDMS substrate by means of a zoom lens and a CMOS camera (2048x2048 pixels, 8 bit resolution) operated in a light transmission mode. The selected radii of the glass spherical lenses were $R = 5.2$, 9.33 and 20.75 mm. The tangential force F_t generated during the sliding contact is measured with a load cell and a lateral displacement is monitored using a non contact laser transducer. Simplified scheme of the two device in Fig. 5.4.

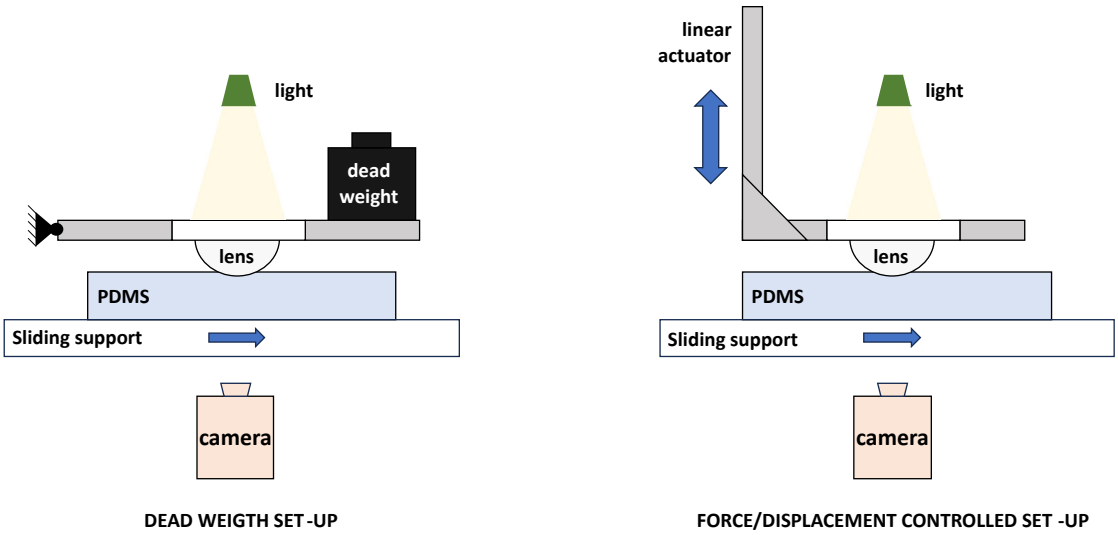

Figure 5.4: Simplified scheme of the home made set-up used for the experiments.

5.1.3 Friction experiments

After achieving contact between the glass lens and the PDMS substrate under the applied normal load, the substrate is then moved at a predetermined velocity v. Throughout the entire experiment, both the tangential force and contact images are recorded. Since the friction is weakly (logarithmically) increasing with velocity [88, 89], it was decided to ignore the effect of this parameter and to carry out experiments at a single imposed velocity, $v = 0.1$ mm s^{-1}.
The surface displacement fields are measured from the continuous monitoring of the position of the dot markers in the contact zone with respect to their position in the undeformed grid. To ensure a proper tracking of the markers all the images are treated from static to full sliding condition. The accumulation of about 400-600 images taken under steady-state sliding conditions allows to generate displacement fields with more than 200,000 data points which are interpolated to provide images of the displacements components u and v along and perpendicular to the sliding direction, respectively.

5.2 Results

In Fig. 5.5, the typical change in tangential force F_t as a function of the imposed displacement is showed. Stiction represents the transition from static contact to full sliding condition. The load peak is associated with the onset of the full sliding at the contact interface. The following results will mostly refer to steady-state sliding where stationary values of the tangential force is achieved. In a latter part, in commenting the effect of the mechanical confinement, some insights will be inferred from a stiction analysis.

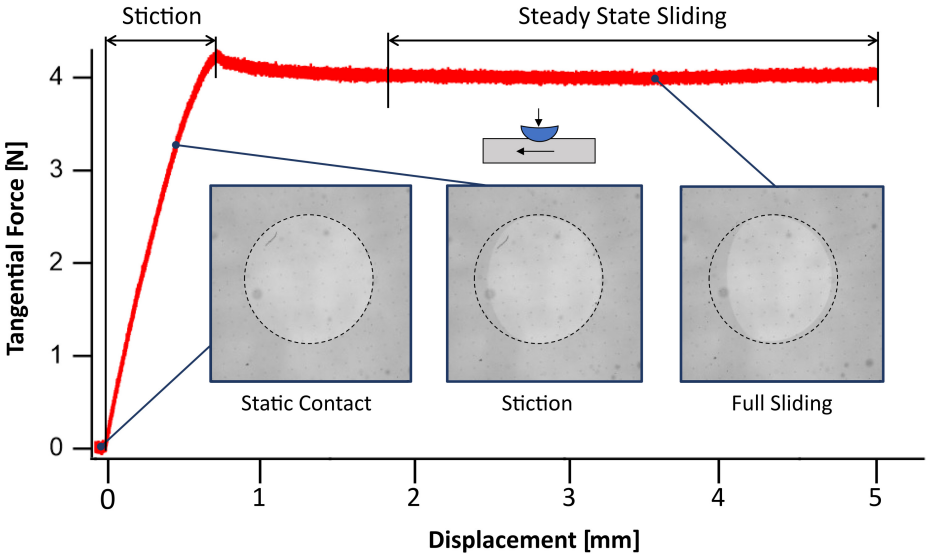

Figure 5.5: Typical tangential force F_t as a function of the imposed displacement during a sliding experiment. Even in the early stages of the experiment, the asymmetry in the contact shape can be observed.

5.2.1 Unconfined contacts

Frictional stress and contact shape

Figure 5.6 shows the average frictional shear stress $\tau = F_t/A$, where F_t and A are the steady-state tangential force and contact area, respectively, as a function of the nominal contact pressure $p_m = F_n/\pi a_0^2$ (F_n and a_0 are the normal load and the static contact radius, respectively). In these experiments, the contact pressure was varied by changing both the normal load and the radius of the spherical glass probe. A weak dependence of the average frictional stress on the contact pressure is observed for S184 with no measurable effects of the radius of the lens, consistently with the adhesion model of friction for polymers proposed by Bowden and Tabor [87]and previous literature evidences [88, 89].
For S184:S527 substrate, a significantly lower frictional stress is measured which cannot be accounted for by a change in the adhesion energy γ which remains unchanged with respect to S184. Instead, it may be due to the change in mechanical

properties or in the interfacial properties (increased concentration of free surface chains at the surface of the S184:S527 substrate). In addition, a slight increase in the measured average shear stress τ is observed when the contact pressure is increased. This could be tentatively attributed to the higher penetration depths achieved for lower radii of curvature at given normal force, which increases the 'ploughing' contribution to friction [142–144].

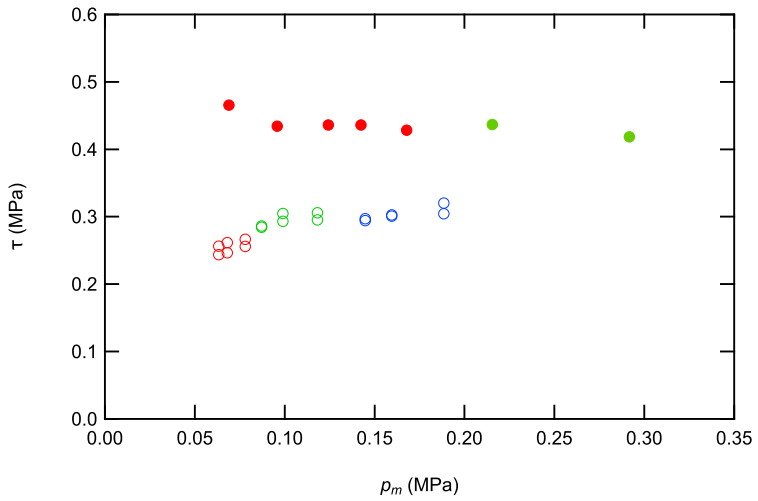

Figure 5.6: Average shear stress τ as a function of the nominal contact pressure p_m for S184 (closed symbols) and S184:S527 (open symbols). Blue: $R = 5.2$ mm; green: $R = 9.33$ mm, red: $R = 20.75$ mm.

Figure 5.7 shows typical examples of images of the contact area under steady-state sliding for S184 and S184:S527 substrates. Images of the static contact area (delimited by dashed lines) have also been superimposed to these pictures. The main effect of sliding is to induce a contact area reduction as a result of a receding of the contact edge at both rear/trailing and front/leading edges. This behavior could in part be explained by assuming a normal-tangential coupling resulting from the nearly-incompressible material response (Poisson modulus $\nu \lesssim 0.5$) [138]. At the trailing edge, the in-plane tensile stretching of the substrate leads to a contraction along the vertical direction which results in a peeling from the sphere. However, the same Poisson effect should imply an extension of the contact at the leading edge where the in-plane compression of the PDMS should induce a surface lifting. In fact, the opposite occurs. Although for incipient sliding conditions experimental and theoretical studies all conclude that the presence of friction at the interface always leads to a reduction of the contact area, conflicting results emerge for full sliding condition where also an increasing of contact area has been reported at moderate velocities (refer to the introduction of this chapter for additional info). However, our evidences seem to suggest a potential effect of friction in weakening adhesion strength, even for gross slip contact, which overshadows a normal-tangential coupling contribution at the leading edge. While this hypothesis has not been validated yet, it could offer a potential solution to the observed counterintuitive behavior.

The contact asymmetry is quantified here from a measurement of the contact radii a and b along and perpendicular to the sliding direction, respectively. Fig. 5.8 shows the change in the ratio b/a as a function of the contact pressure p_m for both the S184 and S527:S184 substrates. Within experimental accuracy, an unique relationship is observed whatever the lens radius or the mechanical properties of the substrate. The contact is becoming more and more symmetrical as the contact pressure is increased.

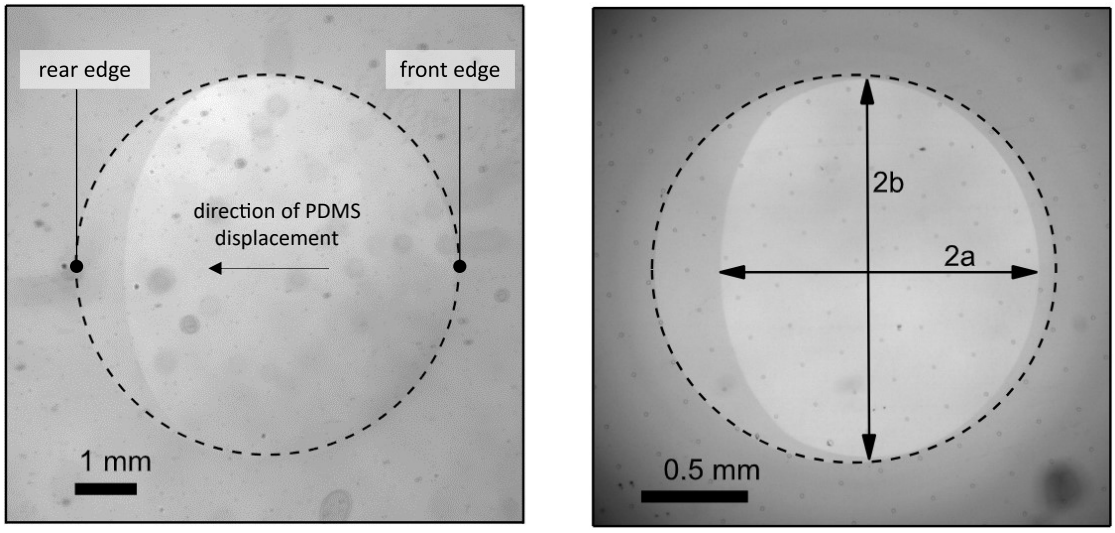

Figure 5.7: Superimposition of contact pictures corresponding to static indentation (delimited by the dotted lines) and steady-state sliding (averaged contact images). (a) S184, $R = 20.7$ mm, $F_N = 5$ N; (b) S527:S184, $R = 5.2$ mm, $F_N = 1.9$ N. The silicons substrate is moved from right to left with respect to the fixed glass lens.

Displacement and strain fields.

As a reference, we first focus on the steady state frictional response of the bulk S184 substrate under increasing applied normal load (between 0.5 and 5 N) and for a lens radius $R = 20.7$ mm. A typical example of the measured displacement fields is shown in Fig. 5.9 for $F_n = 1$ N, where all the space coordinates are taken in the reference, *i.e.* undeformed, space. The main displacement component is occurring along the sliding direction (x axis) while the transverse displacement displays a quadripolar symmetry as a result of Poisson's effects. Profiles of the longitudinal displacement field u and the corresponding logarithmic strain $\ln(1 + \partial u/\partial x)$ across the contact and along the sliding direction x are shown in Fig. 5.10, where both the displacements and the space coordinates have been normalized with respect to the to the static contact radius a_0. As expected, compressive and tensile strains are achieved at the front edge and the leading edge of the contact, respectively. For the considered substrate modulus (E =1.93 MPa) and lens radius ($R = 20.7$ mm), it can be seen that the displacement scales roughly to a_0. Consequently, the magnitude of the applied in plane surface strain is only weakly dependent on the

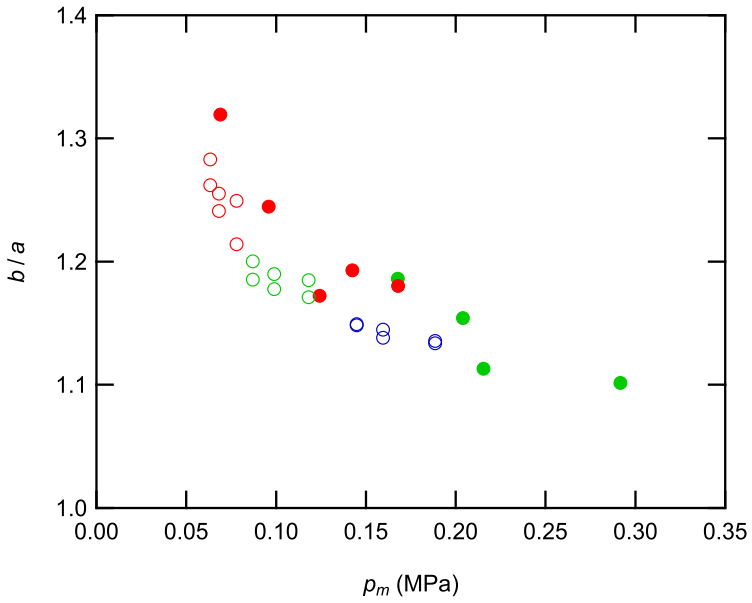

Figure 5.8: Contact aspect ratio b/a as a function of the nominal contact pressure p_m for S184 (closed symbols) and S184:S527 (open symbols). Blue: $R = 5.2$ mm; green: $R = 9.33$ mm, red: $R = 20.75$ mm.

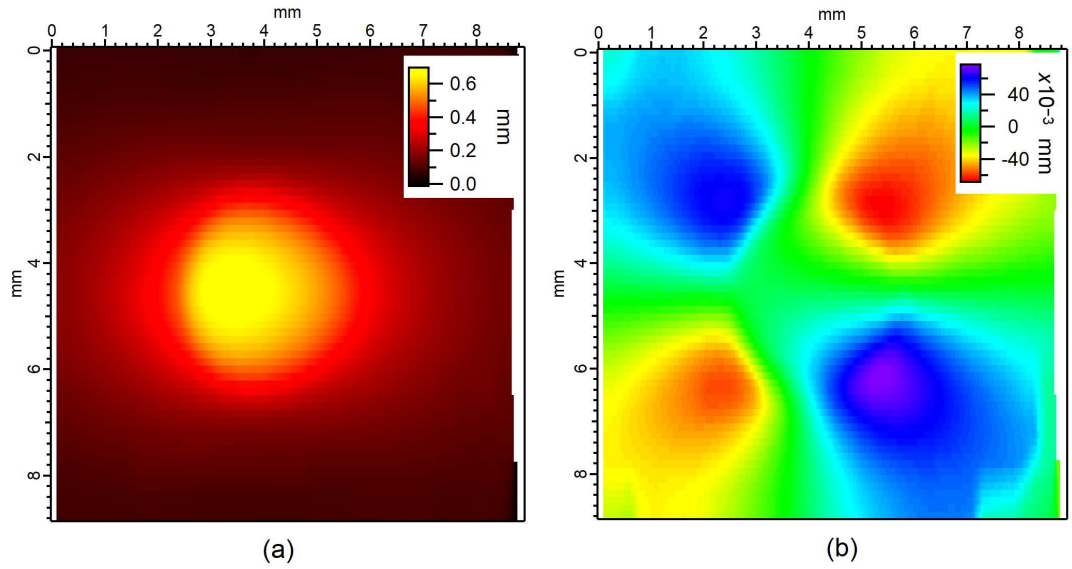

Figure 5.9: Displacement field of S184 during steady-state sliding ($P = 1$ N, $R = 20.7$ mm. (a) displacement component along the sliding direction, (b) displacement component perpendicular to the sliding direction. The rubber substrate is moved from right to left with respect to the fixed spherical probe.

nominal applied normal stress p_m which is ranging from 0.07 to 0.17 MPa when the normal load is increased from 0.5 to 5 N. This is consistent with the finding that a constant, pressure independent shear stress, is achieved within smooth glass/PDMS contacts. It can also be noted the maximum tensile strain level at

the trailing edge of the contact (between 0.35 and 0.4) is slightly outside the neo-Hookean range.

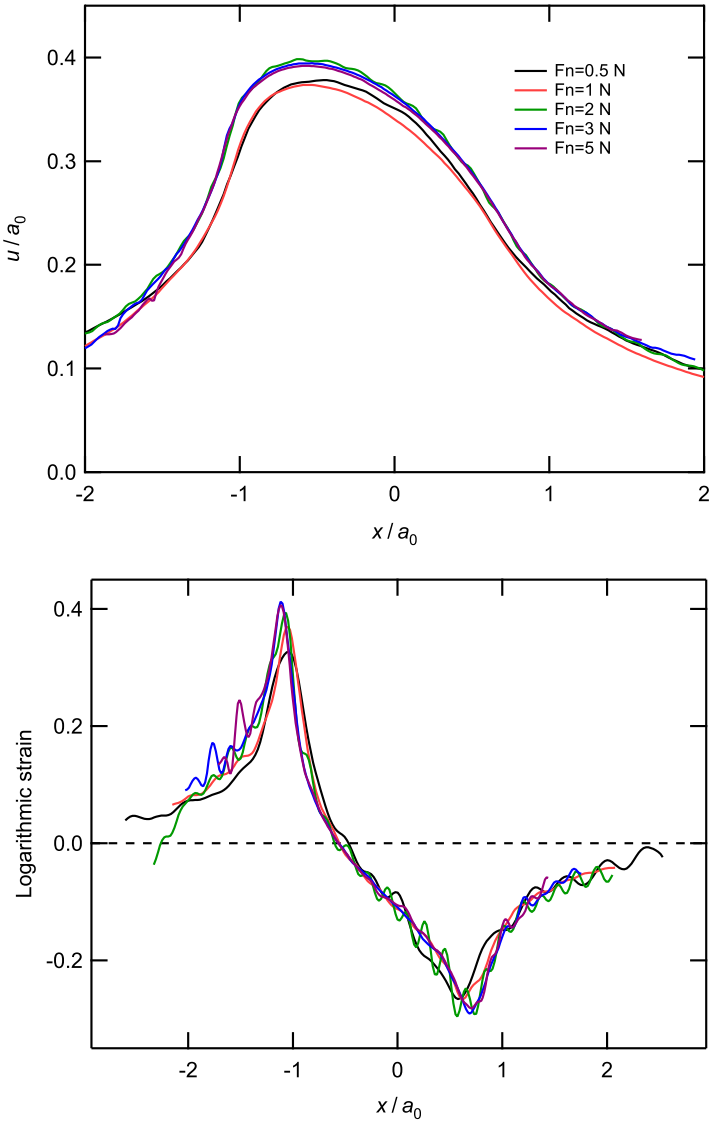

Figure 5.10: Non-dimensional longitudinal displacement (top) and logarithmic strain (bottom) profiles taken across the contact for increasing normal load F_N for the bulk S184 substrate (R = 20.7 mm) . Both the space coordinate x and the displacement component u are normalized with respect to the static contact radius a_0.

Displacement and strain profiles for the softer S184:S527 substrate are shown in Fig. 5.11 for increasing normal loads and a radius of the lens R = 9.33 mm. As for S184, the strain amplitude is roughly independent on the nominal applied contact pressure p_m which is ranging from 0.8 to 0.12 MPa in these experiments. The main difference with the stiffer substrate is the increased strain magnitude, especially at the trailing contact edge where the maximum in-plane tensile strain

is increased by a factor of 1.5 while the elastic modulus is decreased by a factor 2. Noticeably, this increase is achieved for a decreased frictional shear stress τ as compared to the bulk S184 substrate (see Fig. 5.6). The shape of the strain profiles is also altered: the main enhancement in the strain level is occurring in tension at the contact trailing edge which is results in more asymmetric profiles.

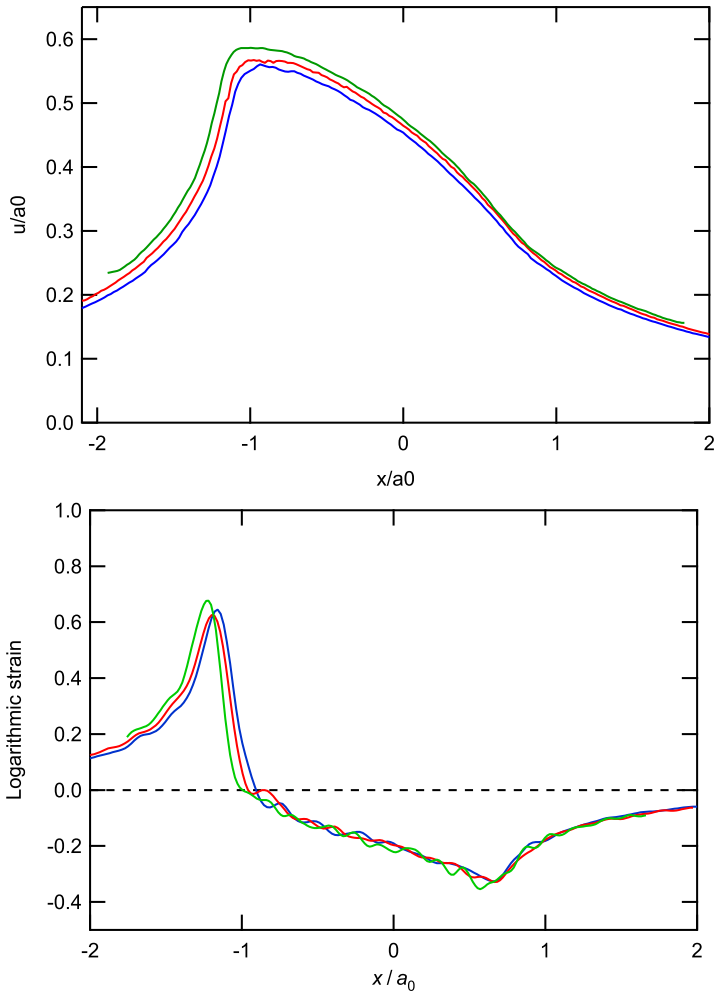

Figure 5.11: Non-dimensional longitudinal displacement (top) and logarithmic strain (bottom) profiles taken across the contact for increasing normal load F_N for the bulk S184:S527 substrate ($R = 9.3$ mm). $F_N = 0.8$ N (blue), 1.1 N (red) and 2.2 N (green). Both the space coordinate x and the displacement component u are normalized with respect to the static contact radius a_0.

5.2.2 Finite size contacts

Frictional stress and contact shape

The average frictional shear stress for confined contacts with the S184 layer 2 mm in thickness is shown in Fig. 5.12 as a function of contact pressure and lens radius. The gray symbols correspond to measurements with a bulk S184 substrate. As opposed to semi-infinite contacts, the frictional shear stress is observed to decrease with increased contact pressure (the difference between the lenses with $R = 9.3$ and $R = 20.7$ mm is not significant). In addition, the confinement seems to result in an increase of the average shear stress at low contact pressures.
Regarding contact asymmetry, a significant effect of the lens radius is now observed: the b/a ratio for the lens $R = 9.3$ mm is roughly independent on contact pressure in the range 0.1-0.3 MPa. It is also lower than for the lens $R = 20.7$ mm.

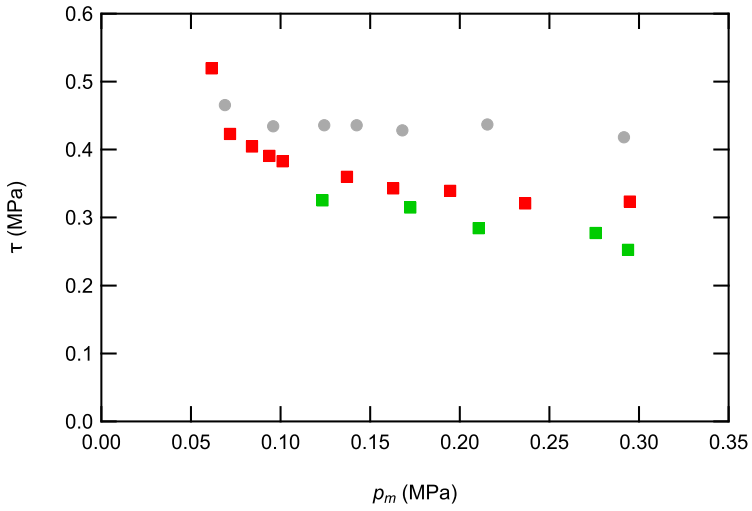

Figure 5.12: Average frictional stress as a function of the nominal contact pressure for a confined S184 layer ($h = 2$ mm). Red: $R = 20.7$ mm; Green: $R = 9.3$ mm; Gray: data for bulk S184 ($R = 20.7$ mm and $R = 9.3$ mm).

Changes in indentation depth during stiction

Evidences of a coupling between normal and lateral direction could be inferred by a change in the indentation depth of the lens with respect to the static indentation equilibrium. As detailed below, this coupling is occurring with both bulk PDMS substrate and confined silicone layers but with opposite trends.

Fig. 5.14 shows the changes in the vertical position of the glass lens as a function of time when a lateral motion is initiated from the static indentation equilibrium in the case of a contact between a S184 layer and a lens ($R = 20.7$ mm) under increasing applied normal loads. In this figure, the filled symbols correspond to the onset of full sliding at the contact interface, assimilated to the time at which a stiction peak force is observed A negative value of Δ_z is indicative of a decrease in

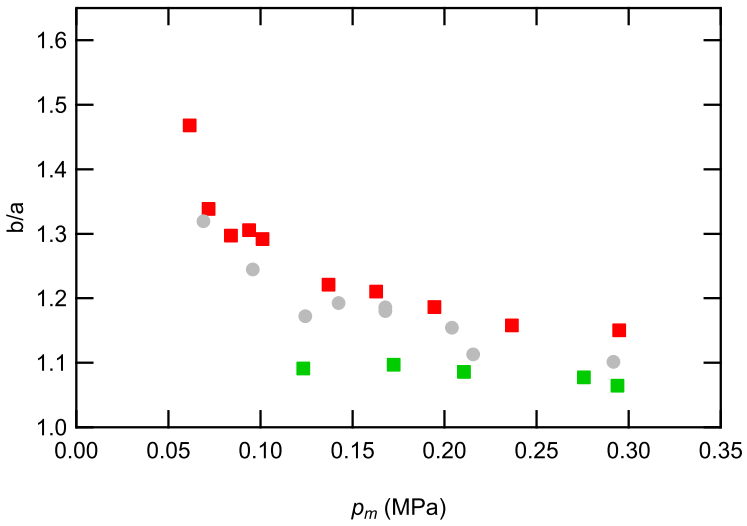

Figure 5.13: Contact aspect ratio as a function of the nominal pressure for a confined S184 layer ($h = 2$ mm). Red: $R = 20.7$ mm; Green: $R = 9.3$ mm; Gray: data for bulk S184 substrates ($R = 20.7$ mm and $R = 9.3$ mm).

the indentation depth. At low applied normal forces F_n, it turns out that the glass lens is slightly *lifted-up* during stiction while at larger F_n it is deeply *sinking-in* in the silicone substrate [1].

In Fig. 5.15 the magnitude Δz^* of the vertical displacement at the onset of full sliding is reported as a function of nominal contact pressure p_m for both the bulk S184 substrate (circles) and the confined S184 layer (square). Two opposite trends are clearly evidenced: while the glass lens tends to be lifted-up during stiction of bulk substrates under a constant applied normal force, the reverse effect is observed for confined contacts with silicone layers lying on a glass flat. In the latter case, a transition from negative to positive Δz^* for increasing p_m also reflects the effect of the confinement, negligible at low normal load and becoming more and more prominent for higher loads. Such a change in the indentation depth can be arguably be attributed to coupling between the vertical and lateral direction which are responsible for an overall lifting or sinking of the substrate surface for bulk and thin specimen, respectively.

Displacement and strain fields

Figure 5.16 shows profiles of the non-dimensional longitudinal displacement and strain across the confined contacts for increased applied normal forces. As com-

[1] After stiction, the observed drift of the vertical position of the lens is simply due to the fact that the surface of the silicone specimen is not perfectly aligned with respect to the axis of translation of the linear translation stage. As a result, the normal load actuator is continuously adjusting the vertical position of the lens to maintain the constant prescribed normal load

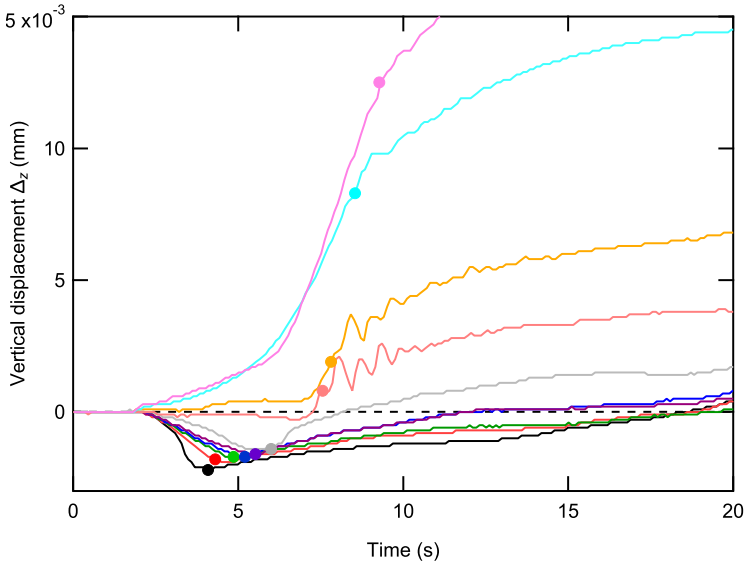

Figure 5.14: Time-change in the indentation depth Δz of a glass lens in a S184 layer during stiction at increasing applied normal forces F_N from 0.1 to 8 N ($R = 20.7$ mm). Filled symbols correspond to the achievement of a full sliding condition at the glass/PDMS interface.

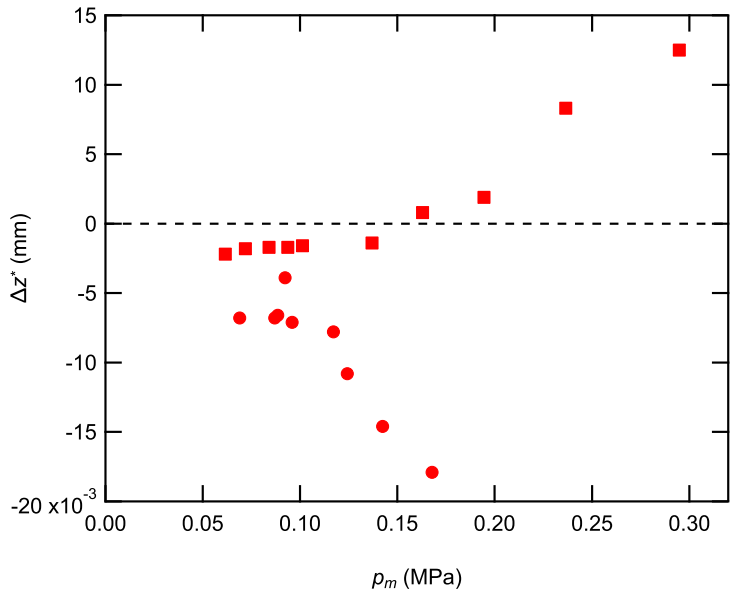

Figure 5.15: Magnitude Δz^* of the change in the indentation depth during stiction for bulk (circle) and film (square) S184 specimens as a function of the nominal contact pressure p_m ($R = 20.7$ mm).

pared to bulk substrates, the maximum strain achieved at the edges of the contact is reduced by a factor of roughly two. This reduction can partially be attributed to the measured decrease in the frictional shear stress by a factor of about 1.5 (see fig. 5.12), and in part it is associated with the mechanical confinement which in-

hibits displacements as effect of stiffening. Moreover, as compared to semi-infinite contacts, we observed an enhanced dependence of the maximum strain achieved at the contact edge on the normal load. The maximum strain saturates at high normal load, and the strain shape evolves from asymmetric to symmetric for increasing contact pressure. This observation aligns with the trend observed in the bulk case, where a stiffer substrate tends to exhibit a more symmetric shape.

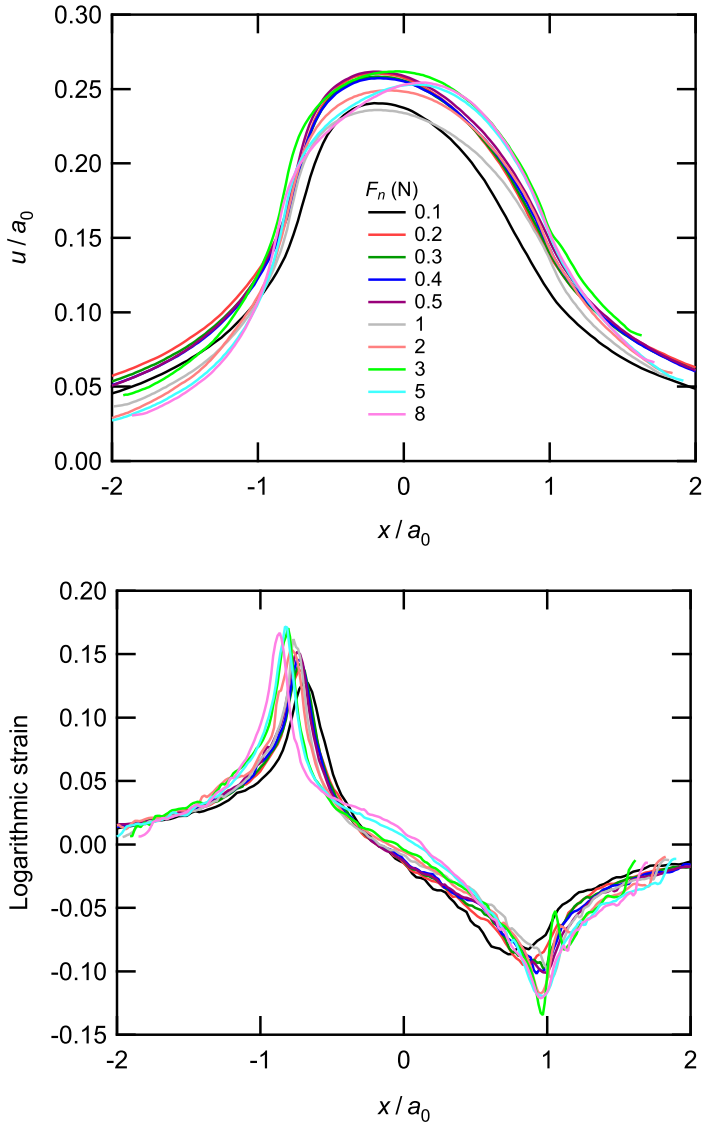

Figure 5.16: non-dimensional longitudinal displacement (top) and logarithmic strain (bottom) profiles taken across the contact for increasing normal load F_N from 0.1 to 8 N for a confined contact with a S184 layer 2 mm in thickness ($R = 20.7$ mm). Both the space coordinate x and the displacement u are normalized with respect to the static contact radius a_0.

5.3 Conclusions

We conducted an experimental study on the frictional sliding contact between a spherical glass probe and a smooth PDMS substrate. Both semi-infinite and confined contact conditions have been investigated using a custom-made setup that enables the measurement of substrate surface displacement. An asymmetry is systematically observed in the contact shape which is associated with a receding of both trailing and leading edge. Large deformations, normal-tangential coupling, and adhesion reduction have been proposed as responsible mechanisms. Indeed tensile and compressive strains achieved at the trailing and leading contact edges, respectively, are systematically lying outside the linear range and sometimes outside the neo-Hookean range. Moreover, changes in the indentation depth during the onset of sliding evidenced a normal-tangential coupling which manifests oppositely with respect to contact confinement: for unconfined contact conditions, the lens is lifted-up during stiction while it is sinking-in for confined contacts. This study could provide new valuable evidence to better understand the mechanisms behind the observed area reduction in frictional sliding contact. Additionally, examining the effects of confinement may help explain how material and geometrical non-linearities can impact this phenomenon.

Conclusions

This thesis has addressed some opened problems in contact mechanics field in order to foster the understanding on dissipative phenomena and geometrical aspects in governing the behavior of adhesive and debonding systems.

As main focus of our study, a rounded overview on peeling mechanism has been presented (Chapter 1). From the first approaches to current researches, we have discussed theoretical and experimental frameworks for its analysis underlining the importance of including viscoelasticity in peeling models as pivotal aspect of real-life processes. To address this problem, basic notions linear viscoelasticity have been introduced (Chapter 2) and creep and relaxation functions as well as constitutive equations for viscoleastic models have been derived.

In Chapter 3 we have investigated the single peeling behavior of a thin viscoelastic tape peeled away from a rigid substrate. In a first scenario, stuck contact condition have been assumed at the interface between tape and substrate. The overall viscoelastic peeling behavior has resulted independent of the peeling velocity, with the peeling force resembling the Kendall's prediction for elastic tape, with the elastic modulus given by the high-frequency viscoelastic modulus of the tape material. Under these conditions, the energy dissipation associated with the viscoelastic creep of the tape is entirely localized in the detached portion of the tape. In a second scenario the presence of frictional sliding at the interface close to the peeling front have been considered. Additional energy dissipation occurs, associated with the work done by frictional shear stress and viscoelastic hysteresis in the adhering tape section. The system's delamination resistance appears enhanced for low peeling angle, with the peeling force diverging at vanishing peeling angle. The interplay between these dissipative contributions results in a velocity dependent peeling behavior, in agreement with phenomenological models and experimental observations.

Chapter 4 have investigated the V-peeling of a thin viscoelastic tape. Governing equations have been derived from energy balance and geometrical arguments and a numerical procedure has been deployed to model the nonsteady peeling propagation taking into account for the viscoleastic tape relaxation and the changing in system's arrangement. We have considered three possible scenarios, associated with different controlled parameters: the peeling front velocity, the peeling force, and the pulling velocity at the tape tip. Regardless of the specific controlled parameter, peeling propagation asymptotically approaches a steady-state elastic-like behavior, while the initial transient peeling behavior is strongly affected by the tape viscoelasticity and undeformed geometry, and could present non-monotonic

time evolution of the peeling toughness (and angle). Under given peeling force conditions, depending on the peeling force and undeformed geometry, the peeling propagation can either start and indefinitely continue, start and successively stop, or even not start at all. For imposed pulling velocity condition, the system can exhibits peaks of peeling resistance especially for fast loading, as in the case of impact loads.

Lastly, in Chapter 5 we have reported the main evidences of sliding contact experiments between a PDMS rubber and a glass spherical probe aimed at investigating the effect of material/geometric non-linearities and mechanical confinement on the frictional contact behavior. A particular device has been employed for the continuous recording of contact images which have been treated in order to obtain a measure of surface displacements. Contact area reduction and asymmetry is always encountered in frictional sliding condition as result of edge receding at leading and trailing edge. This evidence, widely discussed for full-stick contact condition, results not completely understood for gross slip situations. As large deformations outside the material linear elastic range are observed at contact edges, non-linearities have been invoked for explaining this behavior. Moreover, semi-infinite and confined contact condition resulted in opposite behavior with respect of indentation depth during the stiction regime: for unconfined contact conditions, the lens is lifted-up during stiction while it is sinking-in for confined contacts.

We hope that these findings could advance our understanding on the role of particular aspects of contact systems in governing their overall behavior and could help to unravel still unclear evidences observed in the natural world, in various engineering applications, and everyday life experiences.

References

[1] N. Bandara, H. Zeng, J. Wu, Marine mussel adhesion: biochemistry, mechanisms, and biomimetics, Journal of adhesion science and technology 27 (18-19) (2013) 2139–2162.

[2] M. Varenberg, N. M. Pugno, S. N. Gorb, Spatulate structures in biological fibrillar adhesion, Soft Matter 6 (14) (2010) 3269–3272.

[3] W. Barthlott, C. Neinhuis, Purity of the sacred lotus, or escape from contamination in biological surfaces, Planta 202 (1997) 1–8.

[4] M. D. Hager, P. Greil, C. Leyens, S. van der Zwaag, U. S. Schubert, Self-healing materials, Advanced Materials 22 (47) (2010) 5424–5430.

[5] D. Bechert, W. Reif, On the drag reduction of the shark skin, in: 23rd Aerospace sciences meeting, 1985, p. 546.

[6] Y.-T. Cheng, D. E. Rodak, Is the lotus leaf superhydrophobic?, Applied physics letters 86 (14) (2005).

[7] B. Bhushan, Y. C. Jung, Micro-and nanoscale characterization of hydrophobic and hydrophilic leaf surfaces, Nanotechnology 17 (11) (2006) 2758.

[8] C. Creton, S. Gorb, Sticky feet: from animals to materials, Mrs Bulletin 32 (6) (2007) 466–472.

[9] K.-J. Cho, J.-S. Koh, S. Kim, W.-S. Chu, Y. Hong, S.-H. Ahn, Review of manufacturing processes for soft biomimetic robots, International Journal of Precision Engineering and Manufacturing 10 (2009) 171–181.

[10] W.-L. Min, B. Jiang, P. Jiang, Bioinspired self-cleaning antireflection coatings, Advanced Materials 20 (20) (2008) 3914–3918.

[11] M. A. Meitl, Z.-T. Zhu, V. Kumar, K. J. Lee, X. Feng, Y. Y. Huang, I. Adesida, R. G. Nuzzo, J. A. Rogers, Transfer printing by kinetic control of adhesion to an elastomeric stamp, Nature materials 5 (1) (2006) 33–38.

[12] J. Hwang, Y. Jeong, J. M. Park, K. H. Lee, J. W. Hong, J. Choi, Biomimetics: forecasting the future of science, engineering, and medicine, International journal of nanomedicine (2015) 5701–5713.

[13] A. Shafiee, A. S. Cavalcanti, N. T. Saidy, D. Schneidereit, O. Friedrich, A. Ravichandran, E. M. De-Juan-Pardo, D. W. Hutmacher, Convergence of 3d printed biomimetic wound dressings and adult stem cell therapy, Biomaterials 268 (2021) 120558.

[14] A. Kinloch, Adhesives in engineering, Proceedings of the Institution of Mechanical Engineers, Part G: Journal of Aerospace Engineering 211 (5) (1997) 307–335.

[15] R. S. Rivlin, The effective work of adhesion, in: Collected Papers of RS Rivlin: Volume I and II, Springer, 1997, pp. 2611–2614.

[16] M. D. Bartlett, S. W. Case, A. J. Kinloch, D. A. Dillard, Peel tests for quantifying adhesion and toughness: A review, Progress in Materials Science (2023) 101086.

[17] K. Kendall, The adhesion and surface energy of elastic solids, Journal of Physics D: Applied Physics 4 (8) (1971) 1186.

[18] N. M. Pugno, The theory of multiple peeling, International journal of fracture 171 (2011) 185–193.

[19] L. Afferrante, G. Carbone, G. Demelio, N. Pugno, Adhesion of elastic thin films: double peeling of tapes versus axisymmetric peeling of membranes, Tribology Letters 52 (2013) 439–447.

[20] F. Bosia, S. Colella, V. Mattoli, B. Mazzolai, N. M. Pugno, Hierarchical multiple peeling simulations, Rsc Advances 4 (48) (2014) 25447–25452.

[21] D. Nicholson, Peel mechanics with large bending, International Journal of Fracture 13 (1977) 279–287.

[22] N. Menga, L. Afferrante, N. Pugno, G. Carbone, The multiple v-shaped double peeling of elastic thin films from elastic soft substrates, Journal of the Mechanics and Physics of Solids 113 (2018) 56–64.

[23] L. Afferrante, G. Carbone, The ultratough peeling of elastic tapes from viscoelastic substrates, Journal of the Mechanics and Physics of Solids 96 (2016) 223–234.

[24] L. He, J. Lou, S. Kitipornchai, J. Yang, J. Du, Peeling mechanics of hyperelastic beams: Bending effect, International Journal of Solids and Structures 167 (2019) 184–191.

[25] H. Chen, X. Feng, Y. Huang, Y. Huang, J. A. Rogers, Experiments and viscoelastic analysis of peel test with patterned strips for applications to transfer printing, Journal of the Mechanics and Physics of Solids 61 (8) (2013) 1737–1752.

[26] L. Benyahia, C. Verdier, J.-M. Piau, The mechanisms of peeling of uncross-linked pressure sensitive adhesives, The Journal of Adhesion 62 (1-4) (1997) 45–73.

[27] M. Barquins, M. Ciccotti, On the kinetics of peeling of an adhesive tape under a constant imposed load, International journal of adhesion and adhesives 17 (1) (1997) 65–68.

[28] G. Marin, C. Derail, Rheology and adherence of pressure-sensitive adhesives, The Journal of Adhesion 82 (5) (2006) 469–485.

[29] D. Maugis, M. Barquins, Stick-slip and peeling of adhesive tapes, Adhesion 12 (1988) 205–222.

[30] M.-J. Dalbe, P.-P. Cortet, M. Ciccotti, L. Vanel, S. Santucci, Multiscale stick-slip dynamics of adhesive tape peeling, Physical review letters 115 (12) (2015) 128301.

[31] P.-P. Cortet, M. Ciccotti, L. Vanel, Imaging the stick–slip peeling of an adhesive tape under a constant load, Journal of Statistical Mechanics: Theory and Experiment 2007 (03) (2007) P03005.

[32] B.-m. Z. Newby, M. K. Chaudhury, H. R. Brown, Macroscopic evidence of the effect of interfacial slippage on adhesion, Science 269 (5229) (1995) 1407–1409.

[33] S. Wang, X. Li, The effects of tensile residual stress and sliding boundary on measuring the adhesion work of membrane by pull-off test, Thin solid films 515 (18) (2007) 7227–7231.

[34] R. R. Collino, N. R. Philips, M. N. Rossol, R. M. McMeeking, M. R. Begley, Detachment of compliant films adhered to stiff substrates via van der waals interactions: role of frictional sliding during peeling, Journal of The Royal Society Interface 11 (97) (2014) 20140453.

[35] K. Kendall, Peel adhesion of solid films-the surface and bulk effects, The Journal of Adhesion 5 (3) (1973) 179–202.

[36] K. Autumn, A. Dittmore, D. Santos, M. Spenko, M. Cutkosky, Frictional adhesion: a new angle on gecko attachment, Journal of Experimental Biology 209 (18) (2006) 3569–3579.

[37] I. Badge, A. Y. Stark, E. L. Paoloni, P. H. Niewiarowski, A. Dhinojwala, The role of surface chemistry in adhesion and wetting of gecko toe pads, Scientific Reports 4 (1) (2014) 6643.

[38] M. Kang, K. Sun, M. Seong, I. Hwang, H. Jang, S. Park, G. Choi, S.-H. Lee, J. Kim, H. E. Jeong, Applications of bioinspired reversible dry and wet adhesives: A review, Frontiers in Mechanical Engineering 7 (2021) 668262.

[39] S. Kim, M. Spenko, S. Trujillo, B. Heyneman, D. Santos, M. R. Cutkosky, Smooth vertical surface climbing with directional adhesion, IEEE Transactions on robotics 24 (1) (2008) 65–74.

[40] S. Hu, S. Lopez, P. H. Niewiarowski, Z. Xia, Dynamic self-cleaning in gecko setae via digital hyperextension, Journal of the Royal Society Interface 9 (76) (2012) 2781–2790.

[41] M. R. Cutkosky, Climbing with adhesion: from bioinspiration to biounderstanding, Interface Focus 5 (4) (2015) 20150015.

[42] W. G. Bae, D. Kim, M. K. Kwak, L. Ha, S. M. Kang, K. Y. Suh, Enhanced skin adhesive patch with modulus-tunable composite micropillars, Advanced healthcare materials 2 (1) (2013) 109–113.

[43] M. Sexsmith, T. Troczynski, Peel adhesion test for thermal spray coatings, Journal of Thermal Spray Technology 3 (1994) 404–411.

[44] X. Feng, M. A. Meitl, A. M. Bowen, Y. Huang, R. G. Nuzzo, J. A. Rogers, Competing fracture in kinetically controlled transfer printing, Langmuir 23 (25) (2007) 12555–12560.

[45] V. Cacucciolo, H. Shea, G. Carbone, Peeling in electroadhesion soft grippers, Extreme Mechanics Letters 50 (2022) 101529.

[46] I. 8510-1, Adhesives—peel test for a flexible-bonded-to-rigid test specimen assembly—part 1: 90 degree peel (1990).

[47] I. 8510-2, Adhesives—peel test for a flexible-bonded-to-rigid test specimen assembly—part 2: 180 degree peel (2006).

[48] A. A. Griffith, Vi. the phenomena of rupture and flow in solids, Philosophical transactions of the royal society of london. Series A, containing papers of a mathematical or physical character 221 (582-593) (1921) 163–198.

[49] E. Erdogan, Fracture mechanics, International Journal of Solids and Structures 37 (2) (2000) 171–183.

[50] G. R. Irwin, Analysis of stresses and strains near the end of a crack traversing a plate (1957).

[51] Z. Gu, S. Li, F. Zhang, S. Wang, Understanding surface adhesion in nature: a peeling model, Advanced Science 3 (7) (2016) 1500327.

[52] Z. Lu, S. Yu, X. Wang, X. Feng, Effect of interfacial slippage in peel test: theoretical model, The European Physical Journal E 23 (2007) 67–76.

[53] A. Gent, J. Schultz, Effect of wetting liquids on the strength of adhesion of viscoelastic material, The Journal of Adhesion 3 (4) (1972) 281–294.

[54] K. Kendall, Thin-film peeling-the elastic term, Journal of Physics D: Applied Physics 8 (13) (1975) 1449.

[55] G. Spies, The peeling test on redux-bonded joints: A theoretical analysis of the test devised by aero research limited, Aircraft Engineering and Aerospace Technology 25 (3) (1953) 64–70.

[56] D. H. Kaelble, Theory and analysis of peel adhesion: mechanisms and mechanics, Transactions of the Society of Rheology 3 (1) (1959) 161–180.

[57] D. H. Kaelble, Peel adhesion: micro-fracture mechanics of interfacial unbonding of polymers, Transactions of the Society of Rheology 9 (2) (1965) 135–163.

[58] J. Kim, K. Kim, Y. Kim, Mechanical effects in peel adhesion test, Journal of adhesion science and technology 3 (1) (1989) 175–187.

[59] Z. Peng, S. Chen, Effect of bending stiffness on the peeling behavior of an elastic thin film on a rigid substrate, Physical Review E 91 (4) (2015) 042401.

[60] X. Oyharcabal, T. Frisch, Peeling off an elastica from a smooth attractive substrate, Physical Review E 71 (3) (2005) 036611.

[61] R. A. Sauer, The peeling behavior of thin films with finite bending stiffness and the implications on gecko adhesion, The Journal of Adhesion 87 (7-8) (2011) 624–643.

[62] K.-S. Kim, J. Kim, Elasto-plastic analysis of the peel test for thin film adhesion (1988).

[63] M. Zhou, Y. Tian, N. Pesika, H. Zeng, J. Wan, Y. Meng, S. Wen, The extended peel zone model: Effect of peeling velocity, The Journal of Adhesion 87 (11) (2011) 1045–1058.

[64] Z. Peng, C. Wang, L. Chen, S. Chen, Peeling behavior of a viscoelastic thin-film on a rigid substrate, International Journal of Solids and Structures 51 (25-26) (2014) 4596–4603.

[65] M. Loukis, N. Aravas, The effects of viscoelasticity in the peeling of polymeric films, The Journal of Adhesion 35 (1) (1991) 7–22.

[66] N. Menga, D. Dini, G. Carbone, Tuning the periodic v-peeling behavior of elastic tapes applied to thin compliant substrates, International Journal of Mechanical Sciences 170 (2020) 105331.

[67] E. Pierro, L. Afferrante, G. Carbone, On the peeling of elastic tapes from viscoelastic substrates: designing materials for ultratough peeling, Tribology International 146 (2020) 106060.

[68] R. H. Plaut, Two-dimensional analysis of peeling adhesive tape from human skin, The Journal of Adhesion 86 (11) (2010) 1086–1110.

[69] J. Renvoise, D. Burlot, G. Marin, C. Derail, Adherence performances of pressure sensitive adhesives on a model viscoelastic synthetic film: a tool for the understanding of adhesion on the human skin, International journal of pharmaceutics 368 (1-2) (2009) 83–88.

[70] A. Karwoski, R. Plaut, Experiments on peeling adhesive tapes from human forearms, Skin Research and Technology 10 (4) (2004) 271–277.

[71] Z. Zhu, Z. Yang, Y. Xia, H. Jiang, Controllable peeling of an elastic strip on a viscoelastic substrate, Engineering Fracture Mechanics 256 (2021) 107990.

[72] G. Carbone, B. Persson, Hot cracks in rubber: origin of the giant toughness of rubberlike materials, Physical review letters 95 (11) (2005) 114301.

[73] G. Carbone, B. Persson, Crack motion in viscoelastic solids: the role of the flash temperature, The European Physical Journal E 17 (2005) 261–281.

[74] L. Heepe, S. Raguseo, S. N. Gorb, An experimental study of double-peeling mechanism inspired by biological adhesive systems, Applied Physics A 123 (2017) 1–8.

[75] E. Lepore, F. Pugno, N. M. Pugno, Optimal angles for maximal adhesion in living tokay geckos, The Journal of Adhesion 88 (10) (2012) 820–830.

[76] S. W. Cranford, A. Tarakanova, N. M. Pugno, M. J. Buehler, Nonlinear material behaviour of spider silk yields robust webs, Nature 482 (7383) (2012) 72–76.

[77] Z. Qin, M. J. Buehler, Impact tolerance in mussel thread networks by heterogeneous material distribution, Nature communications 4 (1) (2013) 2187.

[78] B.-m. Zhang Newby, M. K. Chaudhury, Effect of interfacial slippage on viscoelastic adhesion, Langmuir 13 (6) (1997) 1805–1809.

[79] B.-m. Zhang Newby, M. K. Chaudhury, Friction in adhesion, Langmuir 14 (17) (1998) 4865–4872.

[80] N. Amouroux, J. Petit, L. Léger, Role of interfacial resistance to shear stress on adhesive peel strength, Langmuir 17 (21) (2001) 6510–6517.

[81] S. Ponce Heredia, Adhesion of thin structures: frictional peeling and adhesive shells, Ph.D. thesis, Paris 6 (2015).

[82] F. D. Blum, B. C. Gandhi, D. Forciniti, L. R. Dharani, Effect of surface segmental mobility on adhesion of acrylic soft adhesives, Macromolecules 38 (2) (2005) 481–487.

[83] Z. Suo, J. W. Hutchinson, Interface crack between two elastic layers, international Journal of Fracture 43 (1990) 1–18.

[84] M. Thouless, H. Jensen, Elastic fracture mechanics of the peel-test geometry, The Journal of Adhesion 38 (3-4) (1992) 185–197.

[85] M. R. Begley, R. R. Collino, J. N. Israelachvili, R. M. McMeeking, Peeling of a tape with large deformations and frictional sliding, Journal of the Mechanics and Physics of Solids 61 (5) (2013) 1265–1279.

[86] S. P. Heredia, Adhesion of thin structures: frictional peeling and adhesive shells, Ph.D. thesis, Université Pierre et Marie Curie-Paris VI (2015).

[87] F. Bowden, D. Tabor, the friction and lubrication oil solids oxford university press (1950).

[88] A. Chateauminois, C. Fretigny, Local friction at a sliding interface between an elastomer and a rigid spherical probe, The European Physical Journal E 27 (2008) 221–227.

[89] A. Chateauminois, C. Fretigny, L. Olanier, Friction and shear fracture of an adhesive contact under torsion, Physical Review E 81 (2) (2010) 026106.

[90] F. P. Bowden, D. Tabor, The friction and lubrication of solids, Vol. 1, Oxford university press, 2001.

[91] A. Jagota, C.-Y. Hui, Adhesion, friction, and compliance of bio-mimetic and bio-inspired structured interfaces, Materials Science and Engineering: R: Reports 72 (12) (2011) 253–292.

[92] W. Chen, Z. Wang, S. Chen, J. Ma, Y. Liang, Frequency response analysis of concrete seawall including soil-structure-seawater interaction, Soil Dynamics and Earthquake Engineering 139 (2020) 106392.

[93] H.-J. Lee, Y. R. Kim, Viscoelastic constitutive model for asphalt concrete under cyclic loading, Journal of engineering mechanics 124 (1) (1998) 32–40.

[94] F. Nabarro, H. De Villiers, The physics of creep [m], London: Taylor and Francis 4 (1995) 4213–4222.

[95] D. G. Backman, J. C. Williams, Advanced materials for aircraft engine applications, Science 255 (5048) (1992) 1082–1087.

[96] Y. Aihara, K. Komatsu, H. Dairoku, O. Kubo, T. Hori, Y. Okada, Cranial molding helmet therapy and establishment of practical criteria for management in asian infant positional head deformity, Child's Nervous System 30 (2014) 1499–1509.

[97] S. Clarren, D. Smith, J. Hanson, Helmet treatment for plagiocephaly and congenital muscular torticollis, The Journal of Pediatrics 94 (1) (1979) 43–46.

[98] T. Royston, H. Mansy, R. Sandler, Excitation and propagation of surface waves on a viscoelastic half-space with application to medical diagnosis, The Journal of the Acoustical Society of America 106 (6) (1999) 3678–3686.

[99] M. Mridha, S. Ödman, Characterization of subcutaneous edema by mechanical impedance measurements, Journal of investigative dermatology 85 (6) (1985) 575–578.

[100] A. Sarvazyan, Shear acoustic properties of soft biological tissues in medical diagnostics, The Journal of the Acoustical Society of America 93 (4_Supplement) (1993) 2329–2330.

[101] L. Ambrosio, R. De Santis, S. Iannace, P. Netti, L. Nicolais, Viscoelastic behavior of composite ligament prostheses, Journal of Biomedical Materials Research: An Official Journal of The Society for Biomaterials, The Japanese Society for Biomaterials, and the Australian Society for Biomaterials 42 (1) (1998) 6–12.

[102] M. D. Geil, An iterative method for viscoelastic modeling of prosthetic feet, Journal of Biomechanics 35 (10) (2002) 1405–1410.

[103] J. Y. Lazennec, Lumbar and cervical viscoelastic disc replacement: Concepts and current experience, World Journal of Orthopedics 11 (8) (2020) 345.

[104] C. Zou, S. Dai, C. Chen, Ethylene polymerization and copolymerization using nickel 2-iminopyridine-n-oxide catalysts: Modulation of polymer molecular weights and molecular-weight distributions, Macromolecules 51 (2018) 49–56. doi:10.1021/ACS.MACROMOL.7B02156.

[105] L. Deng, G. Chen, Recent progress in tuning polymer oriented microstructures for enhanced thermoelectric performance, Nano Energy 80 (2021) 105448.

[106] X. Zhou, D. Yu, X. Shao, S. Zhang, S. Wang, Research and applications of viscoelastic vibration damping materials: A review, Composite Structures 136 (2016) 460–480.

[107] M. Rice, E. Arruda, M. Thouless, The use of visco-elastic materials for the design of helmets and packaging, Journal of the Mechanics and Physics of Solids 141 (2020) 103966.

[108] J. Holnicki-Szulc, P. Pawlowski, M. Wiklo, High-performance impact absorbing materials—the concept, design tools and applications, Smart Materials and Structures 12 (3) (2003) 461.

[109] A. Thatte, R. F. Salant, Effects of multi-scale viscoelasticity of polymers on high-pressure, high-frequency sealing dynamics, Tribology international 52 (2012) 75–86.

[110] M. Thomine, J.-M. Degrange, G. Vigier, L. Chazeau, J.-M. Pelletier, P. Kapsa, L. Guerbe, G. Dudragne, Study of relations between viscoelasticity and tribological behaviour of filled elastomer for lip seal application, Tribology international 40 (2) (2007) 405–411.

[111] A. Abboud, S. A. Nassar, Viscoelastic strain hardening model for gasket creep relaxation, Journal of Pressure Vessel Technology 135 (3) (2013) 031201.

[112] R. S. Lakes, Viscoelastic materials, Cambridge university press, 2009.

[113] R. Villey, P.-P. Cortet, C. Creton, M. Ciccotti, In-situ measurement of the large strain response of the fibrillar debonding region during the steady peeling of pressure sensitive adhesives, International Journal of Fracture 204 (2017) 175–190.

[114] B. Persson, E. Brener, Crack propagation in viscoelastic solids, Physical Review E 71 (3) (2005) 036123.

[115] B. Persson, A simple model for viscoelastic crack propagation, The European Physical Journal E 44 (2021) 1–10.

[116] D. Labonte, W. Federle, Biomechanics of shear-sensitive adhesion in climbing animals: peeling, pre-tension and sliding-induced changes in interface strength, Journal of The Royal Society Interface 13 (122) (2016) 20160373.

[117] N. Krotova, Y. M. Kirillova, B. Deryagin, Issledovanie vliyaniya khimicheskogo stroeniya na adgeziyu, ZHURNAL FIZICHESKOI KHIMII 30 (9) (1956) 1921–1931.

[118] D. Maugis, M. Barquins, Fracture mechanics and adherence of viscoelastic solids. adhesion and adsorption of polymers, Polymer Science and Technology 12 (1980) 203–277.

[119] G. Lake, A. Stevenson, Wave phenomena in low angle peeling, The Journal of Adhesion 12 (1) (1981) 13–22.

[120] M. Ciccotti, B. Giorgini, D. Vallet, M. Barquins, Complex dynamics in the peeling of an adhesive tape, International journal of adhesion and adhesives 24 (2) (2004) 143–151.

[121] A. Molinari, G. Ravichandran, Peeling of elastic tapes: effects of large deformations, pre-straining, and of a peel-zone model, The Journal of Adhesion 84 (12) (2008) 961–995.

[122] A. N. Gent, G. R. Hamed, Peel mechanics for an elastic-plastic adherend, Journal of Applied Polymer Science 21 (10) (1977) 2817–2831.

[123] S. Xia, L. Ponson, G. Ravichandran, K. Bhattacharya, Adhesion of heterogeneous thin films—i: elastic heterogeneity, Journal of the Mechanics and Physics of Solids 61 (3) (2013) 838–851.

[124] N. Cohen, J. H. Waite, R. M. McMeeking, M. T. Valentine, Force distribution and multiscale mechanics in the mussel byssus, Philosophical Transactions of the Royal Society B 374 (1784) (2019) 20190202.

[125] C. Müller, M. H. Müser, G. Carbone, N. Menga, Significance of elastic coupling for stresses and leakage in frictional contacts, Physical Review Letters 131 (15) (2023) 156201.

[126] A. Dimaki, A. I. Dmitriev, N. Menga, A. Papangelo, M. Ciavarella, V. L. Popov, Fast high-resolution simulation of the gross slip wear of axially symmetric contacts, Tribology Transactions 59 (1) (2016) 189–194.

[127] J. B. Adams, L. G. Hector Jr, D. J. Siegel, H. Yu, J. Zhong, Adhesion, lubrication and wear on the atomic scale, Surface and Interface Analysis: An International Journal devoted to the development and application of techniques for the analysis of surfaces, interfaces and thin films 31 (7) (2001) 619–626.

[128] J. Barber, Bounds on the electrical resistance between contacting elastic rough bodies, Proceedings of the royal society of London. Series A: mathematical, physical and engineering sciences 459 (2029) (2003) 53–66.

[129] A. Savkoor, G. Briggs, The effect of tangential force on the contact of elastic solids in adhesion, Proceedings of the Royal Society of London. A. Mathematical and Physical Sciences 356 (1684) (1977) 103–114.

[130] K. Johnson, Adhesion and friction between a smooth elastic spherical asperity and a plane surface, Proceedings of the Royal Society of London. Series A: Mathematical, Physical and Engineering Sciences 453 (1956) (1997) 163–179.

[131] J. F. Waters, P. R. Guduru, Mode-mixity-dependent adhesive contact of a sphere on a plane surface, Proceedings of the Royal Society A: Mathematical, Physical and Engineering Sciences 466 (2117) (2010) 1303–1325.

[132] R. Sahli, G. Pallares, C. Ducottet, I. Ben Ali, S. Al Akhrass, M. Guibert, J. Scheibert, Evolution of real contact area under shear and the value of static friction of soft materials, Proceedings of the National Academy of Sciences 115 (3) (2018) 471–476.

[133] A. Papangelo, M. Ciavarella, On mixed-mode fracture mechanics models for contact area reduction under shear load in soft materials, Journal of the Mechanics and Physics of Solids 124 (2019) 159–171.

[134] N. Menga, G. Carbone, D. Dini, Do uniform tangential interfacial stresses enhance adhesion?, Journal of the Mechanics and Physics of Solids 112 (2018) 145–156.

[135] B. A. Krick, J. R. Vail, B. N. Persson, W. G. Sawyer, Optical in situ micro tribometer for analysis of real contact area for contact mechanics, adhesion, and sliding experiments, Tribology letters 45 (2012) 185–194.

[136] D. T. Nguyen, P. Paolino, M. Audry, A. Chateauminois, C. Fretigny, Y. Le Chenadec, M. Portigliatti, E. Barthel, Surface pressure and shear stress fields within a frictional contact on rubber, The Journal of Adhesion 87 (3) (2011) 235–250.

[137] K. L. Johnson, K. L. Johnson, Contact mechanics, Cambridge university press, 1987.

[138] J. Lengiewicz, M. de Souza, M. A. Lahmar, C. Courbon, D. Dalmas, S. Stupkiewicz, J. Scheibert, Finite deformations govern the anisotropic shear-induced area reduction of soft elastic contacts, Journal of the Mechanics and Physics of Solids 143 (2020) 104056.

[139] N. Menga, G. Carbone, D. Dini, Exploring the effect of geometric coupling on friction and energy dissipation in rough contacts of elastic and viscoelastic coatings, Journal of the Mechanics and Physics of Solids 148 (2021) 104273.

[140] K. L. Johnson, K. Kendall, a. Roberts, Surface energy and the contact of elastic solids, Proceedings of the royal society of London. A. mathematical and physical sciences 324 (1558) (1971) 301–313.

[141] R. N. Palchesko, L. Zhang, Y. Sun, A. W. Feinberg, Development of polydimethylsiloxane substrates with tunable elastic modulus to study cell mechanobiology in muscle and nerve, PloS one 7 (12) (2012) e51499.

[142] F. Bowden, A. Moore, D. Tabor, The ploughing and adhesion of sliding metals, Journal of Applied Physics 14 (2) (1943) 80–91.

[143] R. Spurr, The" ploughing" contribution to friction, British Journal of Applied Physics 7 (7) (1956) 260.

[144] S. Lafaye, C. Gauthier, R. Schirrer, The ploughing friction: analytical model with elastic recovery for a conical tip with a blunted spherical extremity, Tribology Letters 21 (2006) 95–99.

Publications

Journal paper:

- Ceglie, Marco, Nicola Menga, and Giuseppe Carbone. The role of interfacial friction on the peeling of thin viscoelastic tapes. Journal of the Mechanics and Physics of Solids 159 (2022): 104706.
- Ceglie, Marco, Nicola Menga, and Giuseppe Carbone. Modelling the non-steady peeling of viscoelastic tapes. International Journal of Mechanical Sciences (Accepted).